An investigation into the role of fibre bridging as a toughening mechanism in engineered composite materials

Bobby Huxford B.E. (2015), M.E. (2016)

A thesis submitted to the National University of Ireland as fulfilment of the requirements for the Degree of Doctor of Philosophy.

January 2022

Discipline of Biomedical Engineering,

School of Engineering,

College of Science and Engineering,

National University of Ireland Galway.

Supervisor: Dr William Ronan

Table of Contents

Abstract

Fibre reinforced composites are becoming increasingly popular in engineering design due to their high strength to weight ratio. In one of the failure mechanisms, which can occur during impact, fibres can bridge between each of the newly created crack surfaces. This extrinsic toughening mechanism can significantly increase the material toughness. The objective of this thesis is to provide frameworks to characterise this behaviour and capture it correctly in computational models, i.e., using the finite element method.

While previous research has represented this behaviour in models, the procedures to identify the input cohesive properties can be subjective. Using the most commonly used representation of fibre bridging (tri-linear traction separation law), a thorough examination of the possible parameter space is performed. The effect of each parameter is described and a robust method to identify the properties is outlined. This work is performed by virtually mimicking the typical experimental characterisation techniques, i.e., a Double Cantilever Beam (DCB) test. This work is also packaged in a format that allows use by a non-expert user, e.g., in an industry setting. The outputs can be used to compare different material systems or as inputs in larger scale simulations of applications of composite laminates.

To further understand the mechanism of fibre bridging, it is necessary to consider the precise nature of the tractions exerted behind the crack tip. A recently developed experimental method seeks to do this by applying a fixed curvature to cantilever arms of a typical DCB specimen. A theoretical analysis is performed to show how the fracture energy can be related to the applied loads and how the crack length is directly controlled by the applied displacement. Further analysis establishes a method to calculate the tractions generated as a function of crack separation. Simulations using these findings show the conditions under which the approach can give accurate results. For both materials tested with this technique, the data

suggests a second local maximum in the traction separation response; this contrasts with the majority of the literature which considers only a single peak associated with intrinsic toughness.

To further explore the detailed relationship between traction and separation for fibre bridging, a simpler test method based on the standard DCB approach was developed. Using a series of captured images and rotation tracking features on the beams, the slope, curvature, and internal moments were determined along the beam and from this the tractions are derived. These analyses support the existence of the second peak in the bridging tractions. The proposed methods are easily incorporated into standard test methods and the data is directly comparable to standard test methods.

This thesis presents work which can improve the design of composite material systems by quickly assessing the changes in fracture behaviour with increased detail in the extrinsic toughening mechanisms. The research provides experimental and computational methods to accurately characterise the behaviour and facilitate inclusion in simulations of composite applications.

Acknowledgements

I kindly acknowledge funding from NUI Galway College of Engineering and Informatics (now part of the College of Science and Engineering), as well as from industry collaborators Hexcel Composites. Additional funding was also provided by NUI Galway and the Higher Education Authority related to COVID-19.

I would like to thank my supervisor Dr William Ronan for his hard work in providing technical support, guidance and mentoring throughout the duration of my studies.

I thank the technical staff at NUI Galway for assistance in designing and conducting experimental procedures. I also thank the academic staff present during my yearly review for their input to my research.

At Hexcel Composites, I thank Dr Benjamin Russell for technical input to my research and feedback of research conducted. I also thank him and his team at Hexcel Composites for allowing me to visit and complete experiments on site.

Computational resources provided by ICHEC have greatly reduced the time required to perform the large simulations present in this thesis.

Personally, I thank all the PhD students at NUI Galway for providing assistance and a welcome distraction where required. I thank my family for understanding and supporting my research. Finally, I thank my wife Lauren for the support she has provided me during my studies. Without her, I would not have been able to finish this thesis.

Commonly used abbreviations

CFRP	Carbon Fibre Reinforced Polymer(s)
CT	Compact Tension
CTOD	Crack Tip Opening Displacement
CZM	Cohesive Zone Model
DCB	Double Cantilever Beam
DRAFT	Double Rolling Arc Fracture Test
ENF	End notch Flexure
FE	Finite Element
FRP	Fibre Reinforced Polymer(s)
GFRP	Glass Fibre Reinforced Polymer(s)
GUI	Graphical User Interface
TSL	Traction Separation Law
VCCT	Virtual Crack Closure Technique

Chapter 1. Introduction

This thesis is focused on understanding an extrinsic toughening mechanism known as fibre bridging or crack bridging. This research is directed primarily towards composite structures and is conducted at a micro-scale. The research contains computational and experimental components.

1.1 Composite materials

A composite material is made up of two or more constituent materials, typically having different physical properties, which remain distinct in the finished material. Fibre reinforced polymers (FRP), such as glass fibre reinforced polymer (GFRP) or carbon fibre reinforced polymer (CFRP), are common examples of a composite material. The composite materials considered in this research are synthetic non-woven FRP; hence other composites such as foams, reinforced concrete and metallic composites will not be discussed in detail. Naturally occurring composite materials are also relevant to this research. Biological composites such as adipose tissue [1] and dentin [2] also contain a fibre and matrix structure; and experience toughening mechanisms similar to those found in synthetic composites. Both natural and synthetic composites are considered herein.

Carbon fibre, glass fibre and carbon-epoxy composites are among the materials with the highest specific strength [3] meaning they can provide lightweight solutions to engineering problems for which steels are not viable. Composites and FRP are commonly used in large structural applications such as wind turbine blades and aircraft fuselage or wing surfaces, due to their high strength to weight ratio.

Due to the unidirectional nature of the fibre properties. Composite materials typically consist of numerous plies in different orientations to provide tensile strength along several principal directions. Loading environment dictates the orientation of plies used in composite layups; popular combinations include [0°/90°] and [0°/$\pm$45°/90°].

1.2 Fibre bridging and delamination

Following matrix failure, the fibres in the composite matrix can bridge the crack interface providing a traction between the previously bonded matrix surfaces in a process known as fibre bridging. Fibre bridging is an extrinsic toughening mechanism acting behind the crack tip to significantly increase the material toughness in the wake of crack propagation. As the crack propagates, the density of fibres bridging the interface increases, raising the energy requirement for crack propagation, until a steady state distribution of fibres is reached. A steady state distribution is achieved when new fibres bridging the interface no longer increase the fracture toughness as they are counteracted by fibre breakage or pull-out in the interface.

Fibre rich composite materials therefore do not have a single fracture toughness value, the fracture toughness increases as the crack propagates. The material's fracture toughness reaches a plateau when a steady state distribution of fibres has been reached. This attribute can be found in a range of material types such as CFRP [4], GFRP [5], biological tissues [1,6], and timbers [7,8]. Figure 1-1B shows fibre bridging in a DCB specimen [5]. The length scales over which fibre bridging acts is from the order of micrometres to millimetres (Figure 1-1C).

Fibre bridging is relevant on a structural level, not just at a micro scale. Figure 1-1D shows the effect of a bird strike on an aircraft, an impact event, with fibre bridging present at the perimeter of the damaged area. Fibre bridging is often observed after an impact event or excessive tension causing delamination. The damage experienced can prove difficult to identify, as it is often internal. Figure 1-1A shows a possible mechanism by which fibre bridging occurs after impact loading, this mechanism applies to both internal (in the centre of a laminate for example) and external (at the laminate peripheries) delamination.

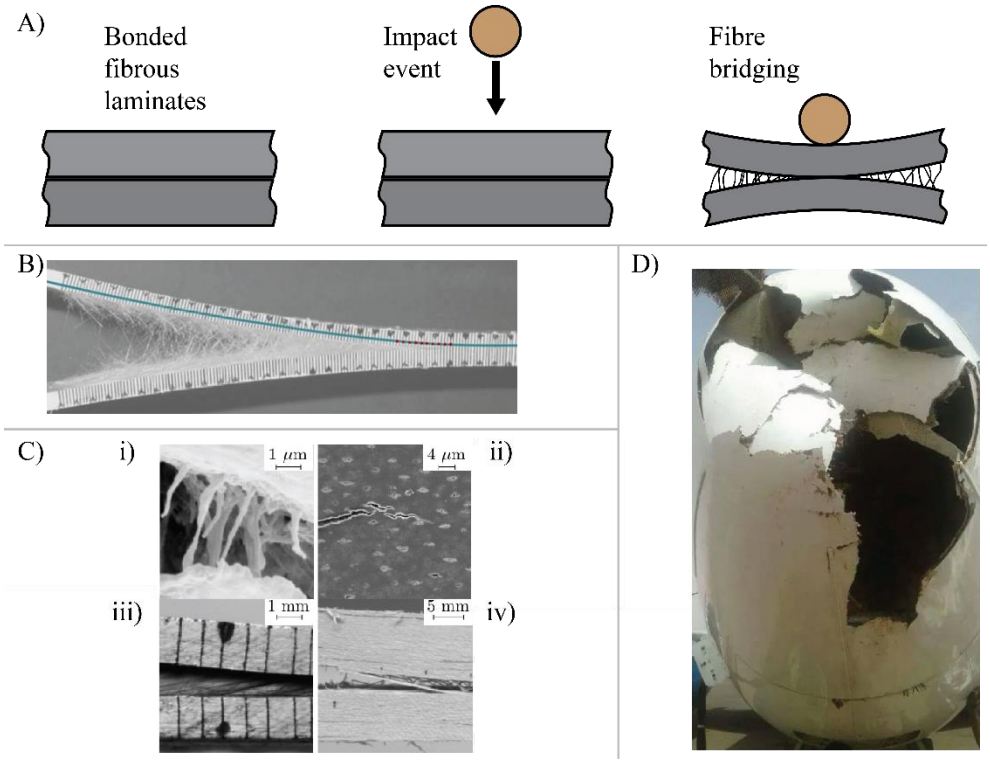

Figure 1-1 A) An impact event leading to delamination of plies, and fibre bridging. B) Fibre bridging in a composite DCB specimen [5]. C) fibre bridging at different length scales adapted from [9]; showing fibre bridging by i) collagen fibrils [10] ii) dehydrated dentin [11] iii) fibre reinforced polymer matrix composite materials [12] and iv) balsa wood [13]. D) The front end of an aircraft following a bird strike. Fibre bridging is present along the perimeter of the damaged area.

This behaviour is typically observed in mode I failure and mixed mode failure, excluding mode II/mode III. There is a mixed mode component to fibre bridging; but mode I opening motivates the mechanism. Increasing mode mixity reduces the level of fibre bridging observed [12]. Fibre bridging is typically of less interest in cyclic or fatigue loading as the load bearing capacity is only active in tension (complete load reversal is not possible) and the damage accumulated in the material at the onset of large-scale fibre bridging is typically too high to consider further fatigue loading.

Inter-ply extrinsic toughening is an important feature in composite materials, significantly increasing the overall damage tolerance of the material. A study by Olave et al. shows that increasing the tow size in woven composites (thus increasing the likelihood of “nesting” of tows between plies) increases the maximum load bearing capacity of the material [14]. The importance of fibre bridging is highlighted by other toughening strategies

such as Z-pinning [15], whereby a third material oriented perpendicular to the laminate is used to prevent crack opening during delamination. This is analogous to an extreme amount of fibre bridging. Z-pinning can increase fracture toughness by an approximate factor or 25 in mode I [16] and an approximate factor of 7 in mode II [17] at a Z-pin percentage volume content of 2%.

1.3 Research motivation and objectives

Ashby and Cebon compared engineering properties of materials and families of materials [3], highlighting the specific strength of engineering composite materials (Figure 1-2D). While intrinsic toughening mechanisms (acting ahead of the crack tip) such as crack tip plasticity, void coalescence, and cleavage fracture are well studied; extrinsic mechanisms (acting behind the crack tip), like fibre bridging, have received less attention in the literature. Extrinsic mechanisms are not fully understood, of particular interest is the effect on the rise in fracture toughness. As the amount of fibre bridging at an interface increases, the energy requirement to advance the crack front increases until a steady distribution of fibres is achieved [18].

Fibre bridging is of interest in engineering applications as the extrinsic toughening, which may be fully realised under impact loading and subsequent delamination, may be the deciding factor between a destructive brittle failure and a controlled ductile failure. In loading scenarios where the full fracture toughness is not realised, the rate of increase of the fracture toughness may be relevant as this will dictate the crack propagation before fibre bridging arrests crack growth. However, as the process is not fully understood, fibre bridging presents difficulties with experimental measurements, computational analyses, and physical interpretation.

Fracture toughness tests evaluate a materials resistance to cracking. Measuring the fracture toughness of a material is not simple. Approximations such as the compliance calibration method are often used in industry. Common test methods include the Charpy impact test, Compact

Tension (CT) test and Izod impact test. These test methods are not capable of capturing the increase in fracture toughness as the crack propagates; hence they are less relevant when fibre bridging is present. The Double Cantilever Beam (DCB) test is commonly used to capture the increase in fracture toughness as the crack propagates. A typical measured response is shown in Figure 1-2B; this response is then used to produce a fracture resistance curve (R-curve), which shows the evolution of fracture toughness with delamination length (Figure 1-2A).

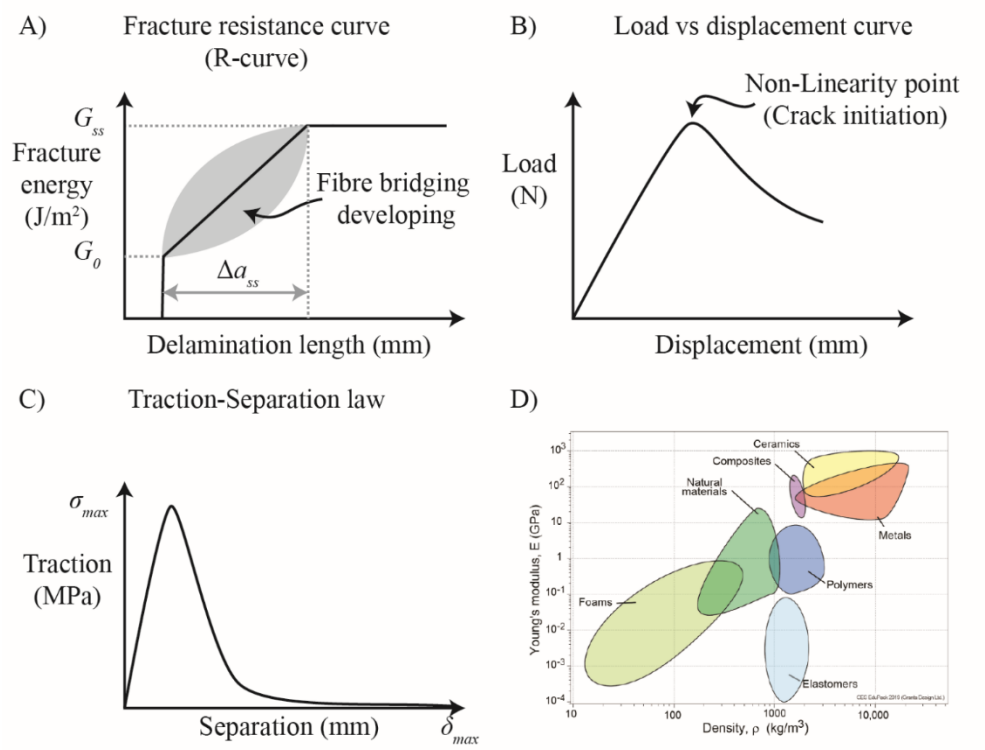

Figure 1-2 A) A fracture resistance curve (R-curve) showing the evolution of energy required to advance the crack front in the presence of extrinsic toughening. B) A typical load-displacement curve showing a decrease in measured load at crack initiation corresponding to the creation of a new crack surface. C) A traction-separation law relating the interfacial traction between debonded surfaces to the local separation between the surfaces. D) A modulus/density chart developed by Ashby [3] used to aid material selection. Materials are grouped into broad categories such as Engineering Composites, Elastomers, Engineering Alloys etc.

In the absence of a singularity, crack tip definition is arbitrary. In practice, definition of the crack tip can vary in experimental fracture tests, irrespective of the presence of fibre bridging. Visual techniques are commonly used to measure crack length. With fibre bridging present it becomes more difficult to accurately define the crack tip. Depending on the

test procedure used, approximate methods such as the compliance calibration technique, may exist to approximate the crack length based on beam curvature for example. These approximations do not account for the effect of fibre bridging on beam curvature. Crack tip rotation correction factors add to the difficulty in defining an appropriate crack tip.

Computationally, fibre bridging also presents difficulties. For instance, it is not feasible to model discrete fibres bridging a cracked interface as the computational cost would be far too high. The exact configuration of the fibres and the fracture properties between fibre tows and the matrix are also not well known. Continuum models are commonly used to approximate the attractive stresses of fibre bridging as a function of localised separation between surfaces. Continuum models typically use cohesive elements or surfaces and traction separation laws (TSL) (Figure 1-2C) to define the interfacial behaviour. Other available techniques such as virtual crack closure technique (VCCT) are discussed in the literature review section. It can be difficult to correctly identify parameters to define a traction separation law, which describes the interface behaviour. Rice developed a J-integral approach in 1968 which is used to determine cohesive properties in multiple studies (as described by Sorensen and Jacobsen [19]), but computing the integral is not straightforward.

The main research objective of this thesis is to further the understanding of how to model fracture processes involving fibre bridging. The objectives of the thesis are outlined below:

1) Develop a robust method of determining traction separation law parameters needed to model ASTM Double Cantilever Beam (DCB) specimens based on experimental observations.
2) Identify the relationship between the measured response and the fracture behaviour using a novel test procedure (the Double Rolling Arc Fracture Test method) which applies a specified beam curvature to composite specimens directly measuring fracture toughness with fibre bridging present, and controls crack growth rate.

3) Determine the true shape of a traction separation law and quantify the tractions exerted by the extrinsic toughening mechanism of fibre bridging.
4) Increase the usability/accessibility of simulation in industry by optimising test methods and data analysis techniques.

1.4 Thesis contents

The thesis contents are summarised below:

1) The current chapter provides introductory information regarding composite materials, toughening behaviour due to fibre bridging and the research goals of this thesis.
2) Chapter 2 provides a comprehensive review of current research on relevant topics; fracture mechanics of fibre reinforced composites, beam bending theory, the finite element method (cohesive zone modelling), and modelling considerations in the technical chapters of this thesis.
3) Chapter 3 details a technical discussion on a method of defining cohesive parameters based on DCB experimental observations.
4) Chapter 4 describes the development of a novel test procedure (the DRAFT method) which directly measures fracture toughness with bridging present, dictates beam curvature and controls crack growth rate. A method of extraction of traction separation law data from the measured response is also provided. This method is then applied to idealised data and experimental data.
5) Chapter 5 presents a modification the DCB test method which allows the interface tractions to be determined based on specimen rotation, recorded throughout the experimental procedure. The method is validated in finite element and applied to experimental data.
6) Chapter 6 provides a discussion of the thesis as a whole and offers concluding remarks.

7) Useful appendices are also attached. These include supplementary data on Chapter 3, a Graphical User Interface developed for industry partners, and a derivation of the compliance calibration method.

1.5 References

[1] Comley K, Fleck NA. The toughness of adipose tissue: measurements and physical basis. J Biomech 2010;43:1823–6. https://doi.org/10.1016/j.jbiomech.2010.02.029.

[2] Nalla RK, Kinney JH, Ritchie RO. Effect of orientation on the in vitro fracture toughness of dentin: The role of toughening mechanisms. Biomaterials 2003;24:3955–68. https://doi.org/10.1016/S0142-9612(03)00278-3.

[3] Ashby M, Cebon D. Materials selection in mechanical design Materials selection in mechanical design. J Phys IV 1993;3. https://doi.org/10.1051/jp4:1993701ï.

[4] De Morais AB. Double cantilever beam testing of multidirectional laminates. Compos Part A Appl Sci Manuf 2003;34:1135–42. https://doi.org/10.1016/j.compositesa.2003.08.008.

[5] Manshadi BD, Farmand-Ashtiani E, Botsis J, Vassilopoulos AP. An iterative analytical/experimental study of bridging in delamination of the double cantilever beam specimen. Compos Part A 2014;61:43–50. https://doi.org/10.1016/j.compositesa.2014.02.001.

[6] Gokgol C, Basdogan C, Canadinc D. Estimation of fracture toughness of liver tissue: Experiments and validation. Med Eng Phys 2012;34:882–91. https://doi.org/10.1016/j.medengphy.2011.09.030.

[7] Vasic S, Smith I. Bridging crack model for fracture of spruce. Eng Fract Mech 2002;69:745–60. https://doi.org/10.1016/S0013-7944(01)00091-1.

[8] Ammann S, Niemz P. FIBRE AND ADHESIVE BRIDGING AT GLUE JOINTS IN EUROPEAN BEECH WOOD. Wood Res 2014;59:303–12.

[9] Canal LP, Alfano M, Botsis J. A multi-scale based cohesive zone model for the analysis of thickness scaling effects in fiber bridging. Compos Sci Technol 2017;139:90–8. https://doi.org/10.1016/j.compscitech.2016.11.027.

[10] Nalla RK, Kinney JH, Ritchie RO. Mechanistic fracture criteria for the failure of human cortical bone. Nat Mater 2003;2:164–8. https://doi.org/10.1038/nmat832.

[11] Kruzic JJ, Nalla RK, Kinney JH, Ritchie RO. Crack blunting, crack bridging and resistance-curve fracture mechanics in dentin: Effect of hydration. Biomaterials 2003;24:5209–21. https://doi.org/10.1016/S0142-9612(03)00458-7.

[12] Borotto M. Bridging effects on Mixed Mode delamination : experiments and numerical simulation. École Polytechnique Fédérale de Lausanne, 2016. https://doi.org/10.5075/epfl-thesis-7056.

[13] Mohammadi MS, Nairn JA. Crack propagation and fracture toughness of solid balsa used for cores of sandwich composites. J Sandw Struct Mater 2014;16:22–41. https://doi.org/10.1177/1099636213502980.

[14] Olave M, Vara I, Husabiaga H, Aretxabaleta L, Lomov S V., Vandepitte D. Nesting effect on the mode i fracture toughness of woven laminates. Compos Part A Appl Sci Manuf 2015;74:166–73. https://doi.org/10.1016/j.compositesa.2015.03.017.

[15] Mouritz AP. Review of z-pinned composite laminates. Compos Part A Appl Sci Manuf 2007;38:2383–97. https://doi.org/10.1016/J.COMPOSITESA.2007.08.016.

[16] Freitas G, Magee C, Dardzinski P, Fusco T. Fibre insertion process for improved damage tolerance in aircraft laminates. J Adv Mater 1994;25:36–43.

[17] Cartié DDR. Effects of z-fibres on the delamination behaviour of carbon fibre/epoxy laminates. 2000.

[18] Khan R. Fiber bridging in composite laminates: A literature review. Compos Struct 2019;229. https://doi.org/10.1016/j.compstruct.2019.111418.

[19] Sørensen BF, Jacobsen TK. Determination of cohesive laws by the J integral approach. Eng Fract Mech 2003;70:1841–58. https://doi.org/10.1016/S0013-7944(03)00127-9.

Chapter 2. Background

2.1 Chapter summary

This chapter provides relevant information regarding fibre bridging in fibre-reinforced, non-woven, laminated, composite specimens, based on the existing literature.

Firstly, as experimental methods for composite laminates typically involve slender beam specimens, Section 2.2 discusses beam bending theories and the differential relationship present in the beam's response (i.e., the relationship between displacement y, slope θ, curvature κ, moment M, shear force V, and distributed load ω). Next, composite structures are discussed in Section 2.3. The fundamentals of fracture mechanics (i.e., Griffith theory, the J-integral, definitions of intrinsic and extrinsic toughening, failure modes and fracture toughness) are outlined in Section 2.4. Fracture specific to fibre reinforced materials is then considered (Section 2.5), including standardised fracture test methods, methods of approximating fracture toughness, and difficulties in defining the crack length. Computational modelling is considered in Section 2.6, topics here include: the finite element method, interfacial behaviour and modelling approaches used in the literature to capture toughening mechanisms present in the fracture of fibre-reinforced composites.

To limit the scope of this review, dynamic fracture and fatigue loading of materials exhibiting fibre bridging are not considered, but it has been studied by numerous researchers [1–3]. Mixed mode loading is reviewed briefly, however it has been shown that fibre bridging is motivated by mode I loading (Figure 2-13) [4].

2.2 Beam bending

A beam is a long structural element that typically deforms in bending. To simplify analyses, considerations based on slender beams are often considered rather than those of thick beams. Common cross-sectional beam

profiles include rectangular, circular and I-beam. Beams can be modelled using theories such as simple beam theory, Euler-Bernoulli beam theory and Timoshenko beam theory. These methods relate beam deflections, applied load, reaction forces and moments, beam curvature and local slope.

The three-dimensional theory of elasticity is the most accurate form of modelling beam bending; but is often difficult to implement. Timoshenko beam theory, Euler-Bernoulli theory and two-dimensional elasticity are common simplifications of the three-dimensional theory of elasticity. Euler-Bernoulli theory (also known as simple beam theory) is the most common of these theories and is a special case of Timoshenko beam theory. A comparison of linear beam theories has previously been published [5].

2.2.1 Euler-Bernoulli beam theory

Euler-Bernoulli beam bending theory, a simplification of linear elasticity, is used to calculate the deflection of beams. It is a simplification of the Timoshenko beam theory, that neglects the effects of shear loading. The Euler-Bernoulli equation relates the beam deflection to the applied load, slope, curvature, bending moment and shear force through a series of differential equations. If the flexural rigidity, EI, is constant the equations can be written as:

$$EI\,\frac{d^4y}{dx^4} = -w(x) \tag{2.1}$$

$$EI\,\frac{d^3y}{dx^3} = V(x) \tag{2.2}$$

$$EI\,\frac{d^2y}{dx^2} = M(x) \tag{2.3}$$

$$\frac{dy}{dx} = \theta(x) \tag{2.4}$$

Where y is the deflection of a point on the beam, w is the applied load, x is the distance along the beam, V is the shear force, M is the internal moment, θ is the slope of the beam, E is the bending modulus and I is the second

moment of area. The second moment of area for a beam with rectangular cross section is written below. From this, the beam thickness, h, has a greater impact on I than the beam width, b.

$$I = \frac{1}{12} b h^3 \qquad 2.5$$

The Euler-Bernoulli theory is limited to slender beams as it does not account for shear affects. The main assumptions in this theory are that:

1. The beam is subject to pure bending, there is no shear force.
2. Plane cross-sections remain planar during deformation. The cross-section does not vary along the length of the beam.
3. The deformed beam slopes are small (Such that $\sin(\theta) \approx \theta$), hence small deflections are considered.
4. The beam is initially straight and free of internal stresses.
5. The beam is isotropic and homogeneous across any cross-section.
6. The material is assumed to be linear elastic.
7. The beam has an axis of symmetry in the plane of bending.
8. The beam will fail by bending rather than by buckling or in compression.

The classic formula for determining the bending stress in a beam subject to simple bending is the flexure formula, shown below in equation 2.6.

$$\frac{\sigma}{q} = \frac{M}{I} = \frac{E}{R} \qquad 2.6$$

Where σ is the internal stress, q is the distance from the neutral axis, M is the internal moment, I is the second moment of area, E is the Young's modulus and R is the radius of curvature.

In order to solve the Euler-Bernoulli beam equations (equations 2.1 to 2.5), boundary conditions must be specified to solve for constants of integration. In simple load cases, an analytical solution to these equations can be found. Numerically, Runge-Kutta iterative methods are commonly used to approximate the system of differential equations [6,7].

The end conditions of a beam dictate the integration constants needed to solve the system of equations governing the behaviour of the beam. These conditions include, for example, simply supported at both ends, fixed, overhanging on one or both ends, cantilever beams fixed at one end and trussed beams supported by cables or rods. Figure 2-1B shows some of these conditions and the implications for the quantities shown in equations 2.1 to 2.5.

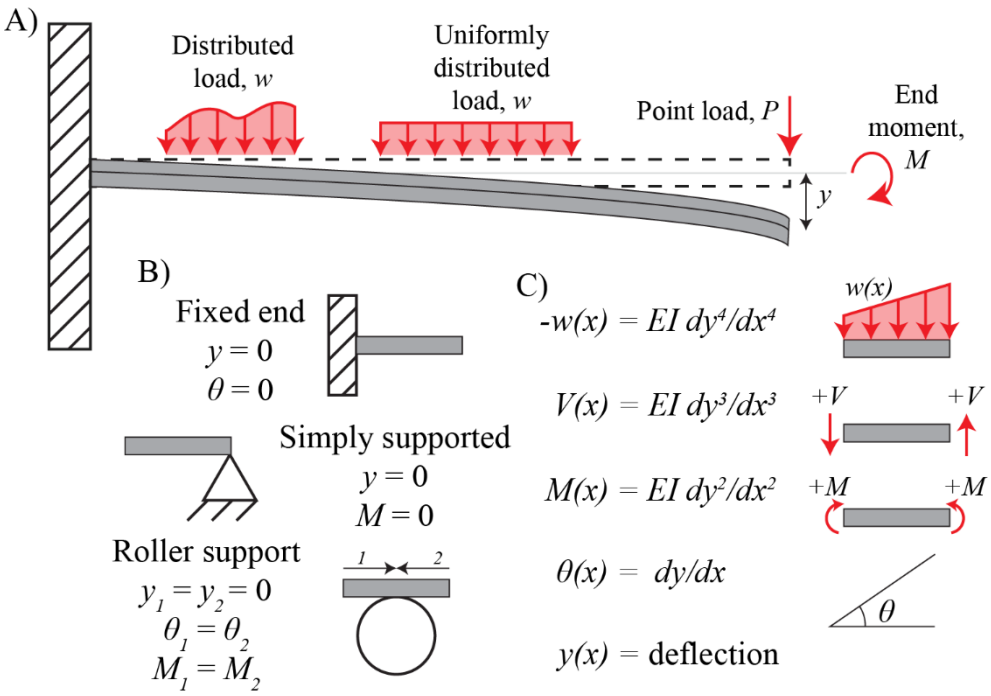

Figure 2-1 A) cantilever beam and loads which are commonly applied to such a structure. B) End conditions C) 4th order differential equations used in beam theory.

2.2.2 Timoshenko beam theory

Timoshenko beam theory is a more general case of beam bending theory than Euler-Bernoulli beam theory as it accounts for the effects of shear and rotary inertia. This theory is suitable for thick beams and composite sandwiches, where Euler-Bernoulli theory would not be appropriate. It is assumed that deformation does not affect beam thickness and the surface normals to the axis of the beam remain straight after deformation. The equation is 4th order, like the Euler equation; but also contains a 2nd order differential term, making it more difficult to solve analytically and numerically.

$$EI\ \frac{d^4y}{dx^4} = w(x) - \frac{EI}{kAG}\frac{d^2w}{dx^2} \qquad 2.7$$

Where y is the deflection of a point on the beam, w is the distributed load, x is the distance along the beam, E is the bending modulus, I is the second moment of area, A is the cross-sectional area, G is the shear modulus and k is the Timoshenko shear coefficient. Note that, this Timoshenko equation (equation 2.7) will collapse to the Euler-Bernoulli equation if the effects of shear are ignored. In this case, G would be set to infinity to provide rigidity to shear deformation, forcing the $\frac{EI}{kAG}$ term to 0.

The shear coefficient depends on the Poisson's ratio and generally must satisfy:

$$\int_A \tau\ dA = kAG\varphi \qquad 2.8$$

where φ is the beam rotation. Cowper found that the shear coefficient can be expressed in terms of the Poisson's ratio for solid rectangular and circular cross sections [8].

Rectangular:

$$k = \frac{10(1+\nu)}{12+11\nu} \qquad 2.9$$

Circular:

$$k = \frac{6(1+\nu)}{7+6\nu} \qquad 2.10$$

It is valid to use Euler-Bernoulli theory rather than Timoshenko beam theory when shear is low. The threshold value for low shear force is calculated in equation 2.11.

$$\frac{EI}{kL^2AG} \ll 1 \qquad 2.11$$

However, it is often simpler to use a criterion based on the specimen aspect ratio. An aspect ratio of 10 to 1 or 20 to 1 is commonly used to assume the Euler-Bernoulli theory is valid.

2.3 Composite structures

A composite material is a non-homogenous mixture of two or more component materials typically with different physical, chemical or electromagnetic properties. Here, the focus is on fibre-reinforced composites which can also be referred to as fibre-reinforced polymers (FRP). However, other types of composites exist for example: reinforced concrete, fibre metal laminates, honeycomb materials and synthetic foams.

While synthetic composites are most commonly discussed in engineering literature, natural materials can also be considered as composites. Natural timber and engineered timber composites are commonly used in the construction industry. Natural composite materials are relevant in biomedical fields; for example, fibrous biological tissue such as adipose tissue. Both biomedical and timber natural composites experience extrinsic toughening mechanisms similar to those found in FRP [9–12].

The main advantage of composite materials, and in particular fibre-reinforced polymers, is their high strength to weight ratio. As FRP lamina are non-isotropic, laminates typically consist of layers at different orientations to provide additional load bearing capacity in the transverse directions. Due to their lightweight nature, composite materials are increasingly being used in the construction of aircrafts [13], aerospace applications [14,15], the automotive industry [16] and in biomedical settings [17].

Composites are anisotropic by nature. A unidirectional composite material's strength in the tensile direction is approximately 15 – 50 times higher than in the shear direction [18]. This highly anisotropic nature means that single laminates are not used in practice. Composite layups are commonly manufactured from multiple laminates to improve material properties in the shear directions. Unidirectional (UD) laminates consist of multiple layers all

orientated in the same direction; while multidirectional (MD) laminates consist of layers in different orientations to provide tensile strength along more than one axis. Common angles used include $0°, 30°, 45°, 60°$ and $90°$. Each laminate is made up of several plies. Each of these plies consist of fibre tows aligned in a principal direction of the ply, and a resin/matrix material around the fibre tows (Figure 2-2).

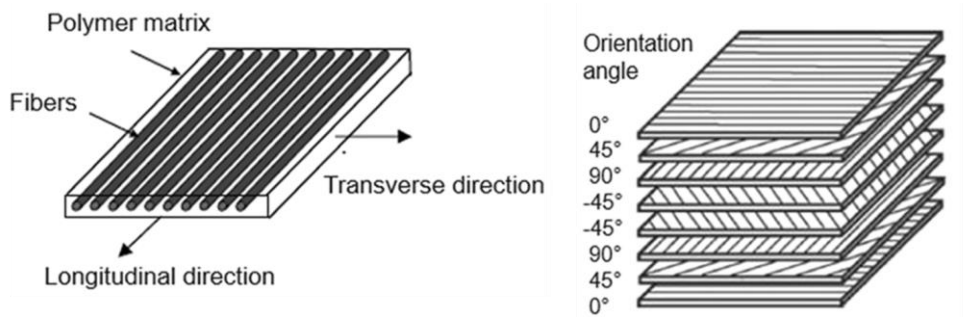

Figure 2-2 Left: a single ply consisting of fibre tows in a polymer matrix. Right: a composite layup consisting of laminates orientated at different angles. Each laminate typically consists of several plies orientated in the same direction. Original image source: [19]

2.4 Fundamental fracture mechanics

During fracture or delamination, there can be significant toughening behind the crack tip in fibre-reinforced composites. The fibrous nature of these materials effects the behaviour at the interface. Fibres from neighbouring surfaces remain attached during fracture. This causes an attractive force to act across the interface and increase the energy requirement for further separation. This phenomenon is an extrinsic toughening mechanism known as fibre bridging.

Fibre bridging in composite materials increases the material fracture toughness, decreasing the likelihood of crack propagation. This process has received much attention in academic literature. Fibre laminates are used in many applications for composite materials, such as aircraft wing and tail fin surfaces, wind turbine blades, and increasingly in the automotive industry. Under impact loading, delamination of neighbouring plies is an important failure mechanism. In the context of these failures, both intrinsic and extrinsic toughening mechanisms occur in composite materials [20–22]. Note that, intrinsic toughening mechanisms refer to mechanisms acting

ahead of the crack tip, while extrinsic mechanisms act in the wake of the crack tip. Fibre bridging is of interest in engineering applications as the additional extrinsic toughening, which may be fully realised under impact loading and subsequent delamination, could be the deciding factor between a destructive brittle failure and a controlled ductile failure.

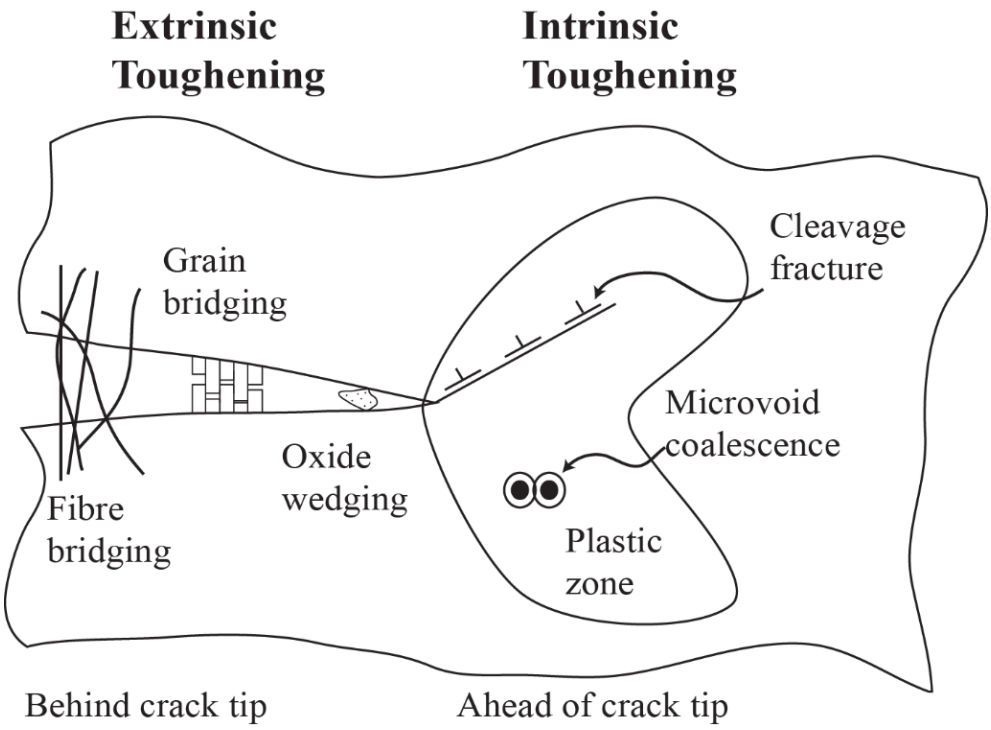

Figure 2-3 Examples of intrinsic (acting ahead of the crack tip) and extrinsic (acting behind the crack tip) toughening mechanisms. Image adapted from Liu et al. [23]

2.4.1 Griffith fracture theory: Crack initiation and crack propagation

Linear elastic fracture mechanics (LEFM) in brittle materials, including crack initiation and propagation theory, is largely based on the fundamental work of Griffith [24]. The Griffith theory states that a crack propagates if the reduction in potential energy (that occurs due to crack growth) is greater than or equal to the increase in surface energy due to the creation of new free surfaces. This theory is applicable to elastic materials undergoing brittle fracture. Griffith found that the energy release rate is defined as the rate of change of the potential energy with respect to the rate of fracture surface creation.

$$G = \frac{\partial \Pi}{\partial s} \qquad 2.12$$

Where s is the fracture surface and Π is the potential energy, given below in equation 2.13.

$$\Pi = \int_V W \, dV - \int_{S_t} \boldsymbol{t} \cdot \boldsymbol{u} \, dS - \int_V \boldsymbol{b} \cdot \boldsymbol{u} \, dV \qquad 2.13$$

The potential energy Π can be written in terms of the strain energy density W, the region occupied by the body V, the surface upon which the tractions $\boldsymbol{t}$ are prescribed S_t, the displacement field $\boldsymbol{u}$, and the body force $\boldsymbol{b}$.

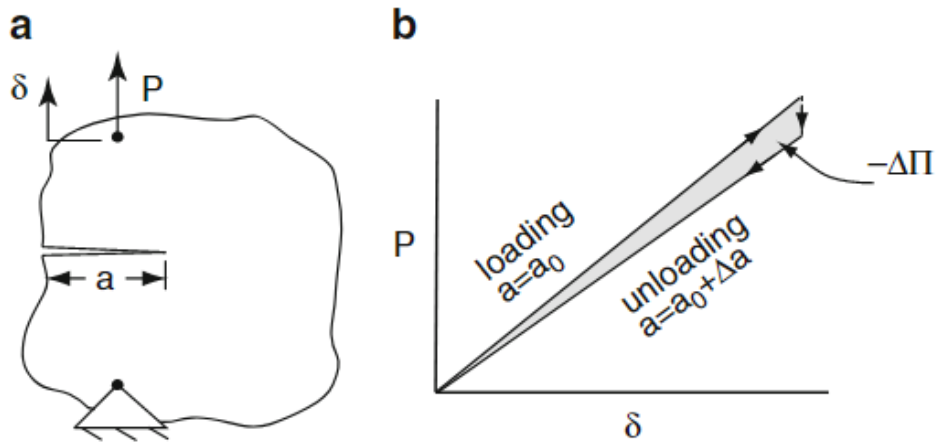

Figure 2-4 a) A cracked linear-elastic material subject to a point load. b) Load-displacement plot for a displacement-controlled crack. The shaded region indicates the reduction in elastic energy associated with the crack increment Δa. Image source Zehnder [25]

The energy released in the generation of a new fracture surface is calculated by taking the limit of the energy release rate as the crack increment tends to zero. The energy release rate can be expressed as:

$$G = -\lim_{\Delta a \to 0} \frac{1}{B} \frac{\Delta \Pi}{\Delta a} \qquad 2.14$$

The key points of Griffith's work that are used as building blocks in later research are that (i) crack initiation can be predicted to occur when the energy release rate exceeds a critical value and (ii) the shape of the material/specimen affects the critical release rate value. i.e., stress

concentrations differ based on test geometry. (iii) the crack will continue to propagate while the energy release rate is above this critical value.

The role intrinsic toughening mechanisms play in the fracture of traditional engineering materials is well studied, for example plasticity behind a crack tip in steels and other ductile metals [26]. The Griffith energy criterion for elastic crack propagation holds for an elastic, homogenous material; there are issues encountered in less idealised materials. Plasticity around the crack tip affects the energy balance [27]. Similarly, the introduction of fibres to the material changes the failure mode from a straightforward crack front advancement to include matrix cracking which is influenced by the presence of fibres, activating extrinsic toughening mechanisms. Extrinsic toughening mechanisms act behind the crack tip to increase fracture toughness as the crack propagates. These toughening mechanisms are not well understood. Of particular relevance to composite materials is fibre bridging, whereby fibres from neighbouring plies remain attached to both delaminated layers.

Griffith theory was developed with brittle elastic materials. Irwin developed a modification to Griffith theory to handle plasticity around the crack tip [28], making the theory applicable to ductile materials. The modification accounts for energy dissipation due to heat generated by plastic loading and unloading near the crack tip. The total energy is then twice the surface energy plus a plastic dissipation term.

It was noted by Sills and Thouless [29] that the terms *plasticity* and *damage* can be used to describe the same phenomena depending on the definition of the crack tip. The crack tip is theoretically a point where the separation between layers is zero and the adjacent point has a finite separation. In practice, the theoretical crack tip is too difficult to use consistently. While plasticity acts ahead of the crack tip, this can also be thought of as intrinsic damage.

2.4.2 The J-integral

The J-integral is a path independent line integral around a crack tip, it represents a method of calculating the strain energy release rate in a material. Inspired by difficulties involved in computing stresses near the crack surface in elastic and elastic-plastic materials. The J-integral can also be used to compute the energy release rate of plastic materials, assuming monotonic loading (and no plastic unloading).

The J-integral, developed by Rice [30], is the most common method of determining the traction separation law, used by numerous researchers as outlined by Sørensen and Jacobsen [31]. The J-integral is equivalent to the fracture toughness G in isotropic, perfectly brittle, linear elastic materials. The expression for the J-integral is shown below.

$$J = \int_{\Gamma} \left(W\, dy - t_i \frac{\partial u_i}{\partial x}\, ds \right) \qquad 2.15$$

Where W is the strain energy density, (x, y) are the coordinate directions with x running in the direction of crack propagation, t is the surface traction vector, u is the displacement vector and Γ is the region on which to integrate.

In monotonic mode I and mode II loading of elastic-plastic materials, the quantity *J* is no longer path-independent, so only a contour very close to the crack tip gives the energy release rate. As the J integral commonly assumes the crack surface is not loaded. Rice has also shown that the J-integral is path-independent in plastic materials when non-proportional loading is not present.

Experimental methods using the J integral were developed to measure critical fracture properties when sample sizes are too small for LEFM to be valid [32].

The integral is computed by taking a closed contour path around the crack tip. The contour is then split into four regions, as shown in Figure 2-5. The J-

integral has the same form as the static component of the energy momentum tensor introduced by Eshelby [33].

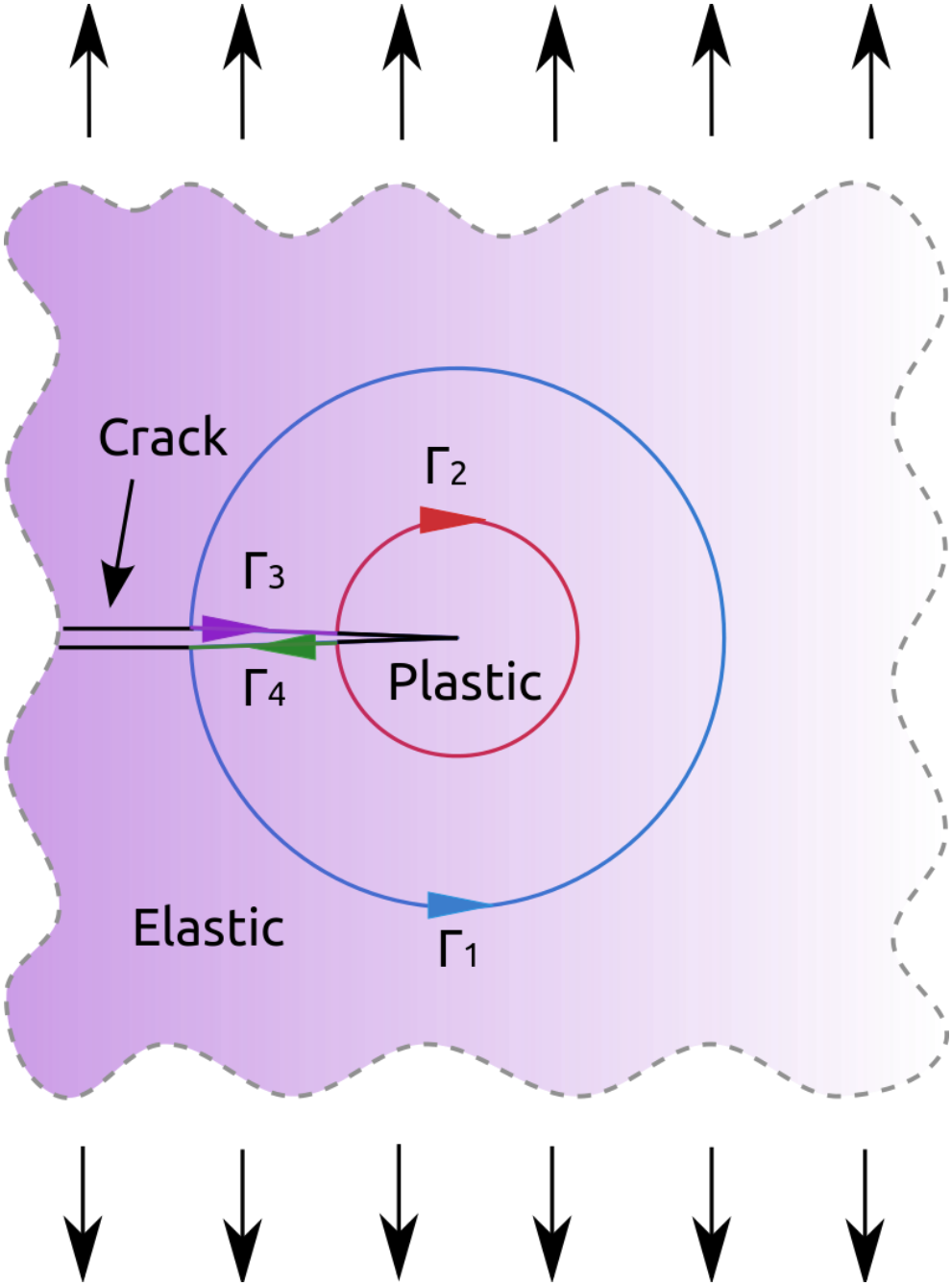

Figure 2-5 Paths taken for J-integral calculation in a 2-dimensional elastic-plastic material.

$$J = \int_{\Gamma_1} + \int_{\Gamma_2} + \int_{\Gamma_3} + \int_{\Gamma_4} = 0 \qquad 2.16$$

Noting the assumption that the crack surface is not loaded, Γ_3 and Γ_4 are assumed to be zero. Hence:

$$\int_{\Gamma_1} = -\int_{\Gamma_2} \qquad 2.17$$

Depending on the material, the integrals in equation 2.17 are calculated differently. If a far field stress is applied to the material and the path Γ_1 is entirely in the elastic zone as shown in Figure 2-5, then the J-integral is:

$$J_{\Gamma_1} = \pi(\sigma_{far})^2 \qquad 2.18$$

If the path is chosen to be entirely in the plastic domain, Hutchinson [34] has shown that:

$$J_{\Gamma_2} = -\alpha K^{n+1} r^{(n+1)(s-2)+1} I \qquad 2.19$$

Where K is the stress amplitude r, θ is a polar coordinate system with the origin at the crack tip, s is a constant and I is a dimensionless integral.

The practical use of the J-integral is later discussed. Determination of cohesive laws is possible by measuring the J-integral and the specimen end opening with pure bending moments [31].

2.4.3 Failure modes and mixed mode loading

Crack propagation can be brought on by applying a force in one or more of three opening modes. These modes are known as fracture modes. Mode I opening occurs when a tensile force is applied normal to the plane of the crack. Mode II sliding occurs when a shear stress acts parallel to the plane of the crack and perpendicular to the crack front. Mode III tearing occurs when a shear stress acts parallel to the plane of the crack and parallel to the crack front. The three modes are shown in Figure 2-6.

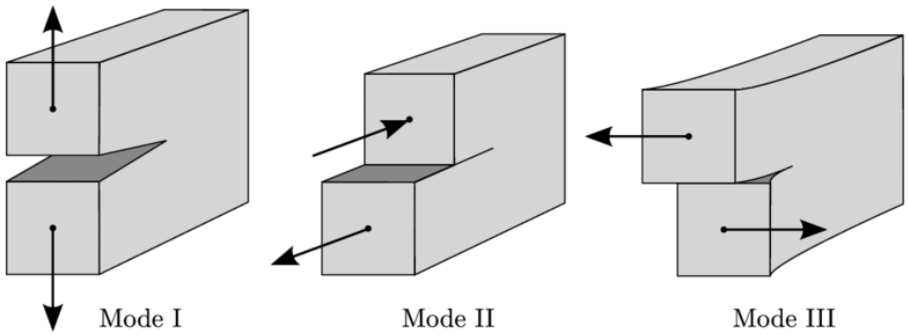

Figure 2-6 Fracture modes. Mode I: opening. Mode II: sliding. Mode III: tearing. Image source: [35]

Considering mode I loading of an elastic material. The material's deformation is recoverable without any permanent deformation to the material. Assuming there is no plasticity, which will introduce permanent material deformation, the load displacement response deviates from linear in the presence of a crack. The crack initiates at the transition from linearity to non-linearity, when the applied load has exceeded a critical value dictated by the material. The load carrying capacity of the material then continues to decrease as the crack propagates.

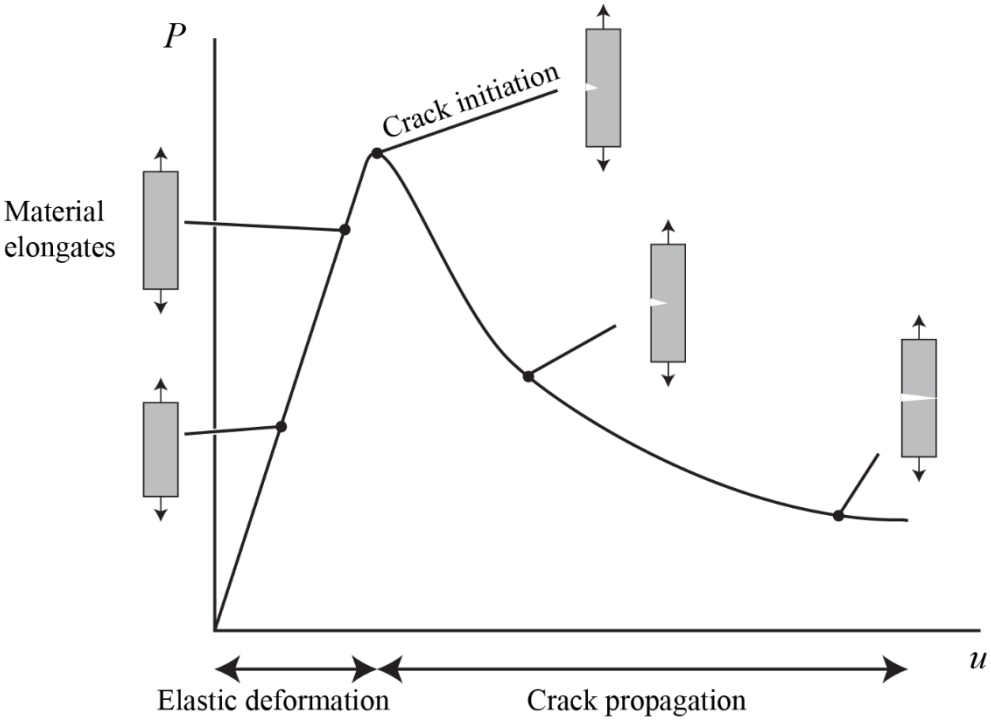

Figure 2-7 Drop in load carrying capacity of a material as a crack initiates and subsequently propagates following elastic behaviour.

In a computational framework, mixed mode loading can be analysed by combining cohesive laws for the modes to be considered or some other combination of the laws. For example, if an element was experiencing 0.01 mm displacement in mode I opening and 0.005 mm displacement in mode II opening and behaves in accordance with the traction separation laws shown below (Figure 2-8); the behaviour is calculated from the mode I and mode II behaviours, based on the following equations (2.20 and 2.21). The commercial finite element software *ABAQUS* use two measures on mode mixity, based on energy and traction. It is also possible to handle modes separately and use the maximum damage parameter from either loading mode [36].

$$\left(\frac{\langle t_n \rangle}{t_n^0}\right)^2 + \left(\frac{t_s}{t_s^0}\right)^2 + \left(\frac{t_t}{t_t^0}\right)^2 = 1 \qquad 2.20$$

$$G^c = G_n^c + (G_s^c - G_n^c)\left(\frac{G_s}{G_T}\right)^\eta \qquad 2.21$$

Where G_n, G_s, G_t and G_T are the energies in the normal, first and second shear directions and the total energy respectively. $G_T = G_n + G_s + G_t$.

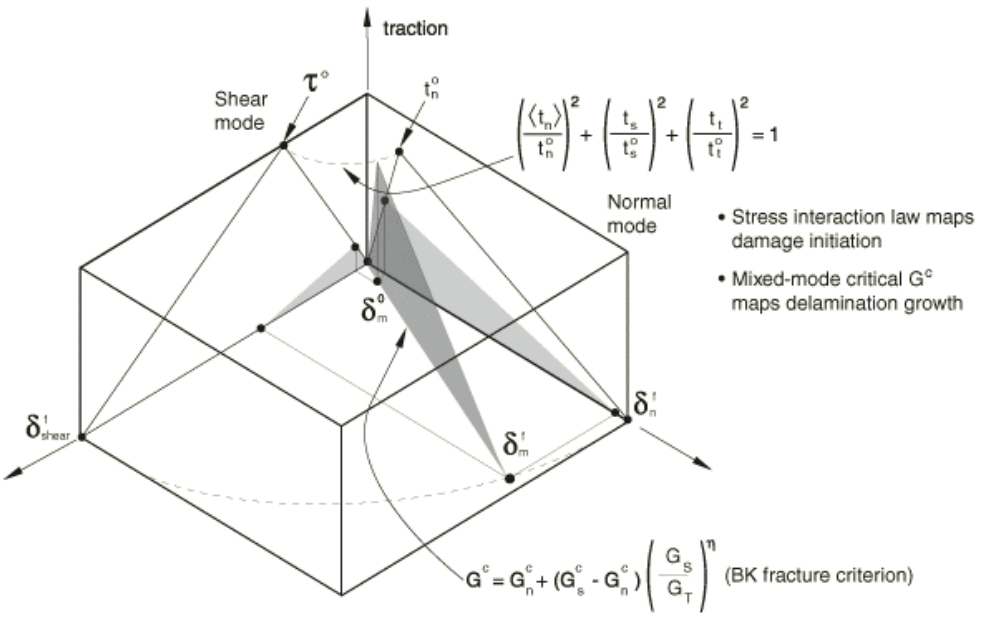

Figure 2-8 Mixed mode response for cohesive elements in the finite element software Abaqus

2.4.4 The crack growth resistance curve (R-curve)

Fracture toughness, $\hat{G}$, is not directly measured experimentally, hence it is evaluated using methods based on linear elastic fracture mechanics such as the compliance calibration method as used by [37,38] or the J-integral as used by [39,40]. Common methods for determining $\hat{G}$ are outlined in the ASTM standards [38] and include beam theory, modified beam theory, the compliance calibration method and the modified compliance calibration method. These methods all consider the change in beam compliance. Corrections are applied for loading block rotation, large displacements, and crack tip rotation. Details of these approximations are provided in section 2.5.4.1.

The crack growth resistance curve, also known as the R-curve, characterises the evolution of a material's fracture toughness as the crack propagation increases. Typically, the fracture energy increases monotonically up to a plateau; the plateau is achieved once a steady distribution of bridged fibres is created behind of the crack tip. In this scenario, bridged fibres which either undergo tensile failure or complete detachment from one of the surfaces are replaced by new fibres entering the bridging zone at the crack tip allowing the fracture energy to achieve a steady state. Materials exhibiting fibre bridging usually have an increasing R-curve; with the resistance to crack propagation increasing as the amount of fibre bridging increases. The amount of fibre bridging increases as the crack propagates until it reaches a steady state. The R-curve will reach a steady state value when a steady state distribution of fibres has been achieved.

R-curves are generally presented following a double cantilever beam (DCB) experiment. DCB experiments typically measure load, load-line displacement and crack propagation, this data is used to produce fracture resistance curves (R-curves) for a given material by approximating $\hat{G}$ using the J-integral of a LEFM method as outlined above (equations 2.27 to 2.30). Computational models attempt to replicate these R-curves and load-

displacement plots, to show the applied traction separation curve is accurate for the material being modelled.

Rising R-curve behaviour cannot be due to intrinsic mechanisms as they act ahead of the crack tip, hence the total intrinsic energy is realised on crack initiation. At this point extrinsic energy begins to be realised. An increase in R-curve behaviour is not always associated with fibre bridging. Other extrinsic toughening mechanisms can cause this type of behaviour.

Heidari-Rarani, et al. propose a trilinear traction separation model for unidirectional DCB specimens under large-scale fibre bridging. The R-curve fracture energy changes from initiation toughness, G_i, to steady state toughness, G_{ss}, over the length of the process zone, l_{pz}. Experimental results show that the rise in the R-curve corresponds with the length of the process zone. [40]

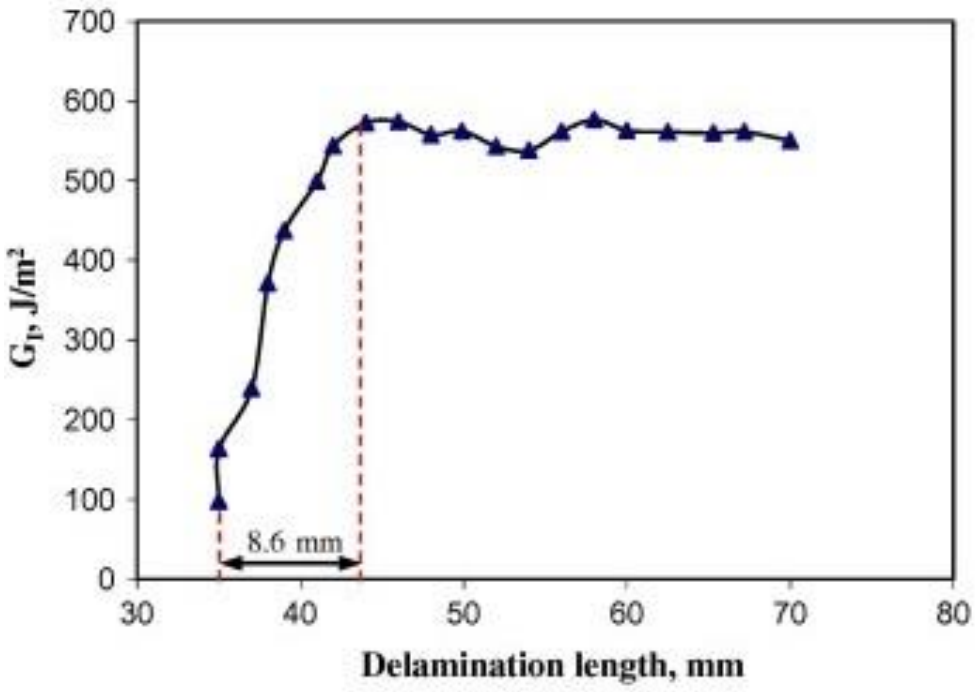

Figure 2-9 Fracture resistance curve (R-curve) (Source: [40]), relating fracture toughness to crack length. The fracture toughness increases on crack initiation until a steady state distribution of fibres is reached.

Crack growth stability is achieved if the strain energy release rate is less than the crack growth resistance curve. Materials that exhibit fibre bridging increase their fracture resistance G_R as the crack propagates. Unstable crack

growth can stabilise if the strain energy release rate is less than the fracture energy at that crack length according to the R-curve, $G < G_R$.

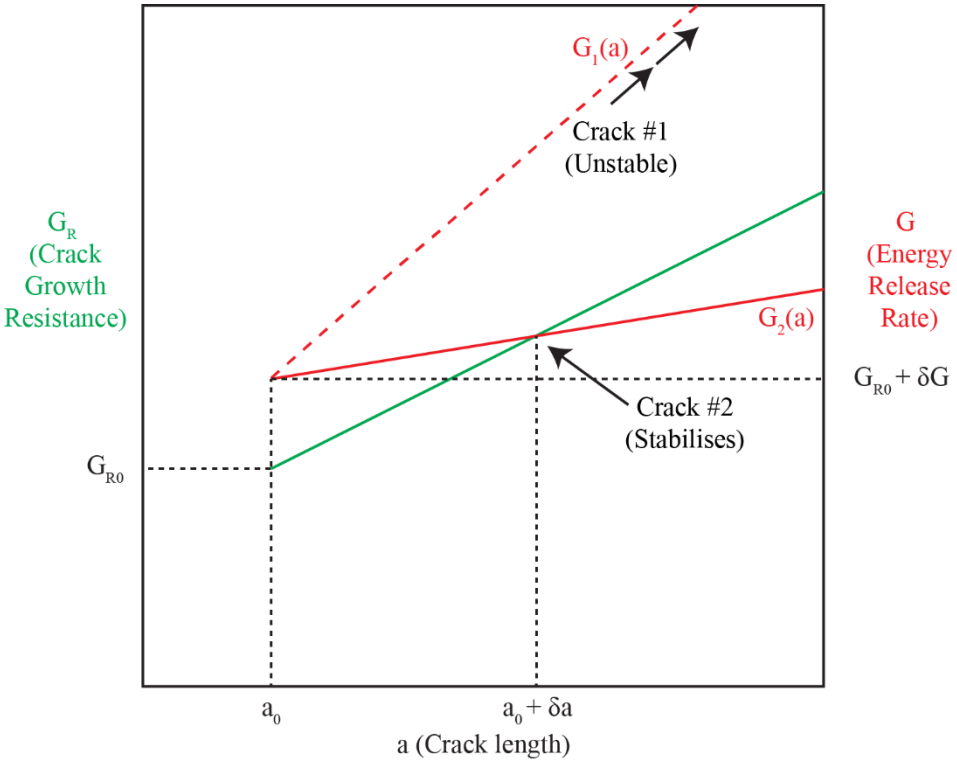

Figure 2-10 The crack growth resistance is shown in Green. Two loading scenarios are shown in red (dashed and solid). In the dashed case, the crack will propagate in an unstable manner as the energy release rate is always above the crack growth resistance $G > G_R$. In the case of the solid red line, the crack will stabilise when $G < G_R$.

The measured load-displacement response and R-curves are specimen dependent; it depends on beam properties such as laminate thickness, modulus, and pre-crack length. Using the J-integral to calculate bridging law parameters, Shokrieh, et al. [41] investigated the effect of initial crack length on unidirectional glass/epoxy DCB specimens. It was found experimentally that the initial crack length only slightly affects the shape of the traction-separation law. Gutkin, et al. also conducted a coupled experimental and computational study showing that an R-curve is specimen dependent. [42]

As the R-curve shows fracture energy as a function of crack length, the definition of crack length (and crack tip in particular) is important. Definition of the crack tip is more difficult when fibre bridging is present. Difficulty arises in experimental observations due to extrinsic toughening mechanisms obstructing the view of the crack tip. In computational research, the crack

tip can be defined more consistently based on the separation of the surfaces, but a finite separation is still required.

The crack length can be defined using approximations such as the compliance calibration method (equation 2.22). The crack can also be defined by observation, with the crack length being measured from an arbitrary crack tip (visually identifiable) to the point of load application (where the Crack Tip Opening Displacement (CTOD) is measured). The crack tip separation must have a finite value to allow detection using visual techniques such as a microscope or magnifying glass.

$$a = \sqrt[3]{\frac{3}{2}EIC} \qquad 2.22$$

In computational work using the finite element method, the Virtual Crack Closure Technique (VCCT) can also be used to approximate the crack length. VCCT assumes that the strain energy dissipated for a crack extension da is equal to the energy required to close the crack by the same amount. This method is a well-established method for computing the energy release rate when analysing fracture problems via the finite element method. VCCT is commonly used in mixed mode fracture problems. A drawback of the VCCT is that assumptions about crack growth must be made, such as the location of cracks, number of cracks and crack lengths.

2.5 Fracture of fibre-reinforced laminates

2.5.1 Failure mechanisms

In composite laminates, there are additional failure mechanisms to consider compared to an isotropic homogeneous material. Different failure mechanisms exist due to the material heterogeneity and the presence of interfaces between material phases (both interlaminar and intralaminar).

Matrix cracking is a major pattern in the failure of composites. Cracks in the matrix occur during manufacture or on an impact event for example. This can occur at laminate level or inside a single lamina/ply. Fibre debonding is

another intralaminar failure mechanism in which the bond between matrix and fibre is compromised. Shear-driven fracture of fibres can also occur (typically in mixed mode loading). As fibres are non-isotropic, shear loads required for fibre failure are typically lower than uniaxial.

Delamination between laminates or plies is an interlaminar failure mechanism in which neighbouring laminates/plies debond from one another. In fibre reinforced materials, fibre bridging typically occurs in delaminated regions. During delamination, fibre pull out can occur. This is a failure mechanism for bridging fibres whereby one end of the bridging fibre pulls out from the crack surface removing the load carrying capacity of that fibre. Another failure mechanism associated with bridging fibres (although it is also associated with internal fibres) is fibre breakage or rupture, whereby the tensile limit of the fibre is exceeded causing the fibre to fail.

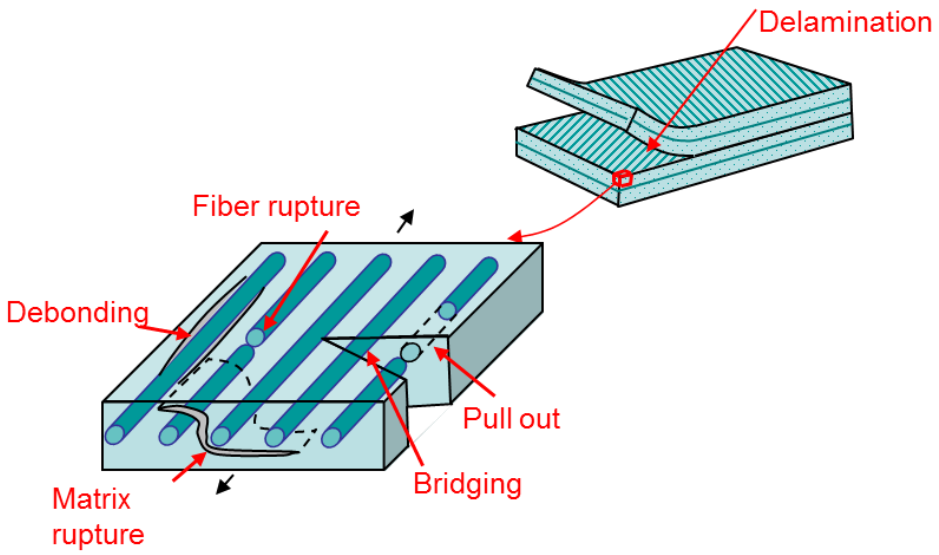

Figure 2-11 Fibre tows inside a matrix (right) showing failure mechanisms in a composite ply. Delamination occurs between laminates/plies (left) Image source: Noels [43].

2.5.2 Fibre bridging

On delamination or matrix failure, the fibres in the composite matrix can bridge between the cracked surfaces providing a traction between the previously bonded matrix surfaces in a process known as fibre bridging or crack bridging. This is an extrinsic toughening mechanism which acts behind the crack tip increasing fracture toughness in the wake of crack propagation.

During crack propagation, the density of fibres bridging the interface increases, raising the energy requirement for crack propagation, until a steady state distribution of fibres is reached. At which point there is a constant turnover of fibres at the interface, where fibre breakage or pull-out at one end of the interface is balanced by new fibres bridging the interface at the other end of the crack. Examples of fibre bridging in different material types are shown below in Figure 2-12.

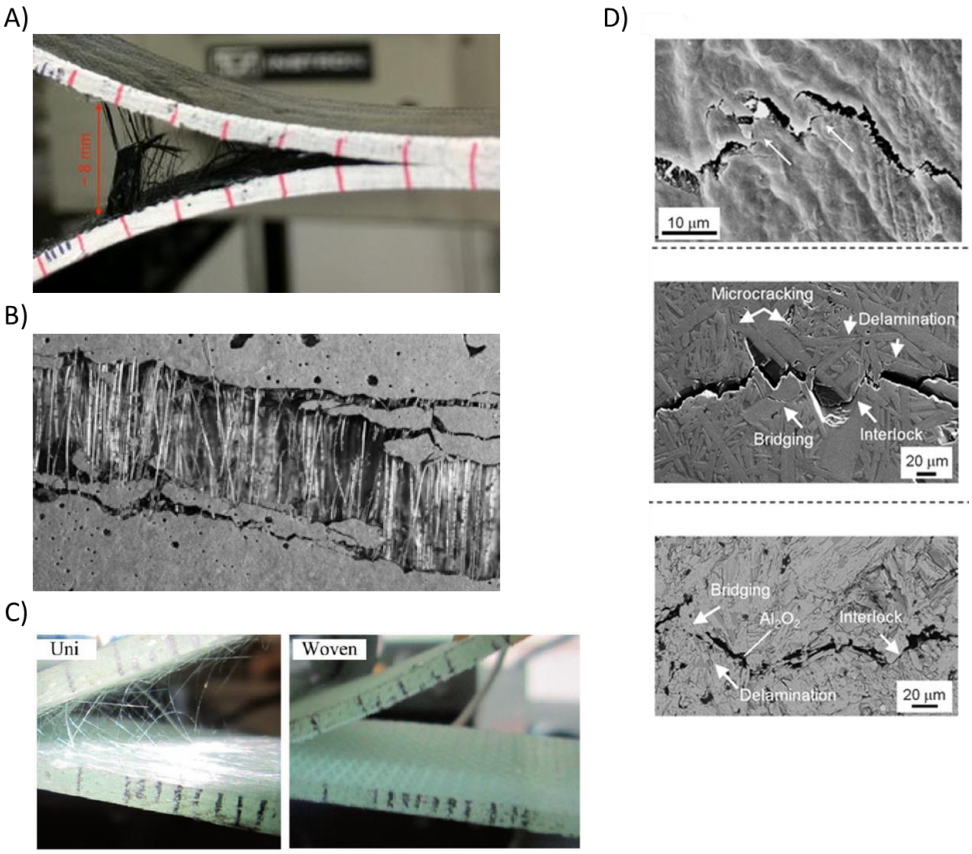

Figure 2-12 A) Fibre bridging in CFRP [44]. B) Fibre bridging across a microcrack in concrete [45]. C) fibre bridging in unidirectional GFRP not present in woven material [46]. D) fibre bridging in biological materials (bone and bone like materials) [47]

Fibre bridging is motivated by mode I opening, but mode II or mode III loading affects the behaviour of bridging fibres. Fibres typically do not provide a high resistance to mode II or III loading as they are comparatively weak to shear loading, as such the directional modulus is typically much higher for mode I loading [18,48]. Loading of fibres in pure mode II or pure mode III is not considered in this review. Naturally, there are loading scenarios where more than one fracture mode is to be considered (mixed

mode loading). Fibre bridging is relevant to mixed mode loading involving mode I opening.

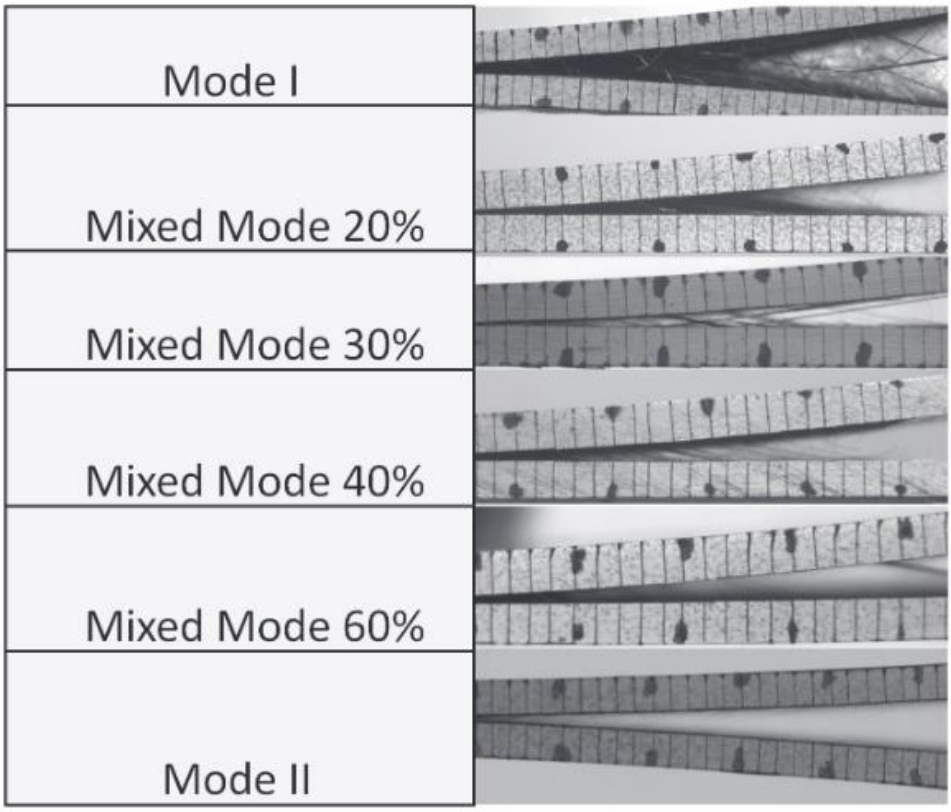

Figure 2-13 Side profile image of bridging fibres in a DCB test with various amounts of mixed mode I / mode II fracture [4]

From Figure 2-13, pure mode II shows little fibre bridging, Fibre bridging is most prevalent in pure mode I loading and the amount of bridging fibres visually decreases as higher levels of mode II are introduced.

2.5.3 Experimental observations of fibre bridging and computational models

While fibre bridging is of interest in engineered composite materials [49,50], such as CFRP [51], GFRP [52] and other fibre rich epoxies [40]; this mechanism also occurs in a range of different materials such as fibrous biological tissue (e.g. Liver tissue [53], adipose tissue [54], frozen arteries [55] and the cornea [12]) and timbers [9,10].

As an inter-laminate crack propagates in a DCB, the bridging fibres exert tractions on the delaminating surfaces, arresting the crack propagation. The

effect of fibre bridging is observed experimentally via the monotonic increase in fracture toughness or energy release rate with increasing crack length, shown in Figure 2-10. The initial value in the crack growth resistance (or R-curves), is set by the energy required for crack initiation. The amount of energy required to advance the crack front then increases as the amount of fibre bridging increases. The fracture toughness plateaus once new fibres bridging the interface compensate fibre breakage or fibre pull out at the other end of the crack.

Experimental research is often coupled with a computational component. Computationally, the effect of fibre bridging is often captured using continuum methods such as a traction separation law (TSL); rather than modelling discrete fibres bridging a crack interface. A TSL relates the local separation between surfaces to the attractive force between these surfaces. The different computational methods of capturing interfacial behaviour are discussed in section 2.6 with the finite element method.

The relationship between the behaviour of a single fibre and the continuum level behaviour (as represented by a TSL) are not well described although there have been several models proposed. Most of these models involve a single fibre bridging an interface but multiple fibres can also be modelled.

The role fibre bridging plays in crack deflection is difficult to predict, Thouless has a number of papers on the topic of energy dissipation around a crack in a fibre rich material [56,57]. Sørensen [58] extended a fibre cross-over model of Spearing and Evans [59] which considered mode I opening to a mixed mode model by considering a tangential crack opening displacement. This model can predict coupled mixed mode traction separation laws. This study found that toughening due to cross-over bridging is predicted to be much higher under mode II and mixed mode than pure mode I. Sørensen found that both normal and shear stresses depend on the normal and tangential crack opening displacements.

In fibre rich materials, bridged fibres can fail due to fibre breakage (either by stretching or tearing), fibres pulling out of the debonding surfaces, fibre buckling, fibre bending or fibre splitting. In a recent study [60], Sørensen also developed a micromechanical model for a single fibre fragmentation test. In this, the interface is characterised by an interfacial fracture energy and a frictional sliding shear stress.

Fibre bridging depends on the composite's constituent materials and specimen geometry [52]. An analytical approach is applied to a DCB specimen to express the through the thickness longitudinal strains in terms of the load and bridging tractions. Results show that the specimen thickness affects the form of the traction separation law but does not affect maximum crack opening displacement or the maximum stress in the traction separation law.

Typical observations of fibre bridging show over a doubling of the total energy compared to the intrinsic energy, as shown in Figure 2-14 [40,41,61]. This is observed in both carbon fibre laminates [61] and glass fibre laminates [40,41]. These tests also showed that (i) The initial slope of the load-displacement response is dependent on the pre-crack length, but the R-curves produced are not significantly different [41]. (ii) High levels of fibre bridging can make traditional fracture theories, such as the corrected beam theory, inappropriate for approximating the crack length in the DCB method [61]. (iii) A bilinear cohesive model cannot replicate this rising R-curve behaviour [40].

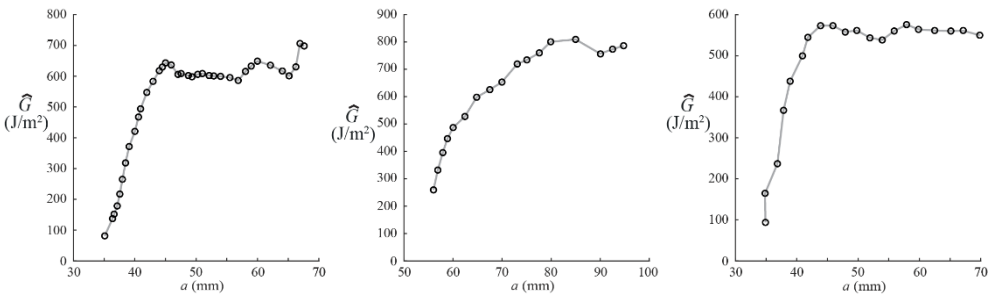

Figure 2-14 Experimental fracture resistance curves for E-glass/epoxy laminates [41] (left), carbon/epoxy laminates [61] (middle), E-glass/epoxy laminates [40] (right)

2.5.4 Fracture test methods in the presence of fibre bridging

In the absence of extrinsic toughening mechanisms (in materials such as steel), the fracture toughness is commonly found using a compact tension test. This fracture toughness data can then be used to define the traction separation law, or interface law, for that material. However, when fibre bridging is present the experimental determination of traction separation laws becomes more difficult.

Numerous test methods have been designed to test the fracture, adhesion, and cohesion of fibre composite materials. Examined in this review: The ASTM DCB fracture test as used by [42,51,62,63], the peel test as used by [64–66], the compact tension (CT) test as used by [67,68] and the end notched flexure test (ENF) as used by [69–71]. All these test methods subject the fibres in a composite to tensile loading.

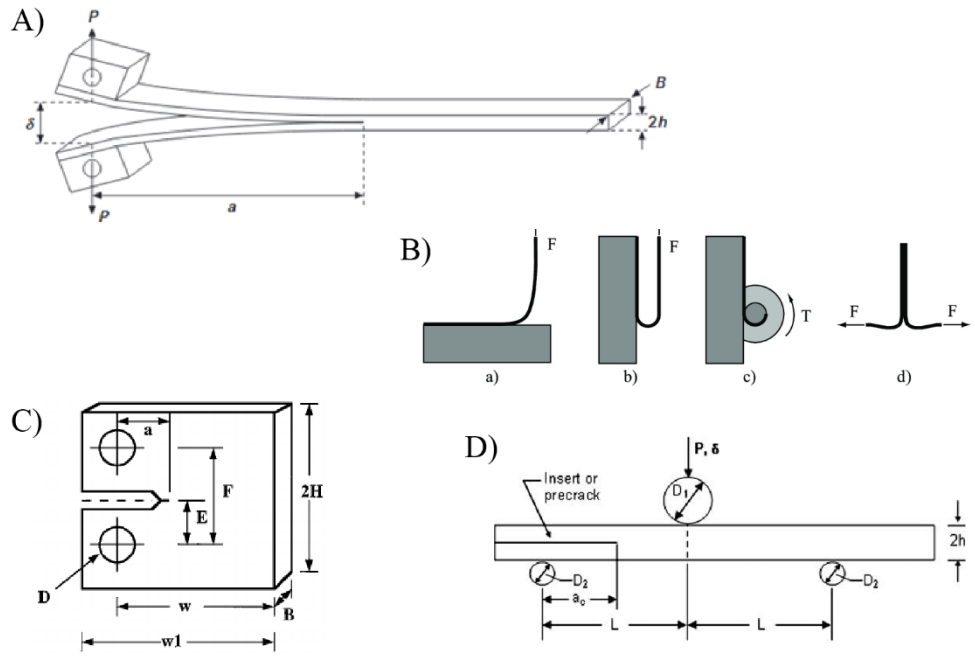

Figure 2-15 Fracture test methods A) DCB [62]. B) Common peel test configurations a) 90° peel test b) 180° peel test c) climbing drum peel test d) T-peel test [72]. C) CT specimen [73]. D) three point bend test also known as ENF test [74].

The compact tension (CT) test method can be performed in accordance with ASTM standards [75]. This test is useful to measure intrinsic toughening mechanisms; however, it has limited effectiveness when extrinsic mechanisms are present as the specimens are typically narrow and do not

have enough material present for the extrinsic mechanism to fully develop and the fibre orientation can affect the crack path [68]. The aspect ratio of the specimen makes the shear components of the load significant, whereas shear components are negligible in other test methods such as the Double Cantilever Beam (DCB) test.

The peel test is used to test the strength of adhesive bonds. The test can be conducted in various set ups but the most common set ups are the 90 degree peel test [76] and the T-peel test [77]. These tests are conducted to ASTM standards. The tests measure the load requirement to break adhesive bonds between the adherend surfaces.

The ENF test method [78] is used to determine the fracture toughness for mode II opening. While this behaviour is not critical for fibre bridging, as fibre bridging is mode I motivated [4], the mode II behaviour is important in mixed mode loading scenarios.

2.5.4.1 Standardised fracture test methods: The ASTM DCB test

Double cantilever beam (DCB) fracture tests often exhibit fibre bridging [51,52,79]. Depending on the material tested this effect can act over a large displacement [80] or a short displacement [81–83]. Even if fibre bridging acts over a seemingly short distance, it can still significantly affect the evolution of fracture toughness. The rate of increase of fracture toughness is of interest in cases where the full extrinsic toughness is not realised. DCB tests are most commonly performed in compliance with a standardised procedure. The most commonly used standards include the ASTM standard [38] and the ISO standard [84]. These procedures are broadly similar, hence only the ASTM standard will be discussed to avoid duplication.

Test specimens are generated from unidirectional 0° laminates, measuring a minimum of 125 mm long and nominally from 20 to 25 mm in width. The thickness is normally between 3 and 5 mm. A pre-cracked region is created by using a non-adhesive insert in the midplane of the laminate to form an initiation site for the delamination. The film is no thicker than 13 μm. The

initial delamination length and specimen height should satisfy equations 2.23 and 2.24 respectively.

$$a_0 \leq 0.042 \sqrt{\frac{h^3 E_{11}}{G_{1c}}} \qquad 2.23$$

$$h \geq 8.28 \left(\frac{G_{1c} a_0^2}{E_{11}}\right)^{1/3} \qquad 2.24$$

Where a_0 is the pre-crack length, $2h$ is the specimen thickness, E_{11} is the modulus in the fibre direction, and G_{1c} is the mode I fracture toughness. The standard states that at least five test specimens should be used for statistical significance unless valid results can be obtained from fewer specimens, such as the case of a designed experiment.

The test is conducted by attaching the specimen to a tensile test machine using either loading blocks or piano hinges. The test is load-controlled. Loading blocks or piano hinges are attached to the pre-cracked end of the specimen to allow the specimen to attach to the tensile test machine. Loading blocks should be as small as possible to minimise errors as a result of the applied moment arm. The correction factor N should be applied (equation 2.26) if the following criteria is not met:

$$t \leq \frac{h}{4} + 0.01 \sqrt{\frac{0.0434 h^3 E_{11}}{G_{1c}} + a^2} \qquad 2.25$$

$$N = 1 - \left(\frac{L'}{a}\right)^3 - \frac{9}{8}\left[1 - \left(\frac{L'}{a}\right)^2\right]\left(\frac{\delta t}{a^2}\right) - \frac{9}{35}\left(\frac{\delta}{a}\right)^2 \qquad 2.26$$

Where $2L'$ is the width of the loading blocks and $2t$ is the height of the loading blocks. In the case of piano hinges, $L' = 0$ and $2t$ is the thickness of the hinge when closed.

The onset of delamination can be determined by three methods (Figure 2-16A):

- Deviation form linearity (NL) – This method assumes that the delamination starts to grow when the load displacement plot deviates from a linear response.
- Visual observations (VIS) – A visual initiation value of G_{1c} is recorded at the visual onset of delamination. This method usually involves a microscope or a mirror.
- 5% Offset/Maximum Load (5%/Max) – The value of initiation G_{1c} is calculated from the intersection of the load-displacement curve and a line drawn from the origin with a 5% increase in the compliance from the original linear region of the load-displacement curve.

The difference is between these methods is small. A tough matrix has slightly more variation in the initiation point than a brittle matrix.

2.5.5 Approximating fracture toughness

The fracture toughness of the material is approximated based on the load-displacement response and the measured crack length. In some cases, the crack length is not measured and is approximated based on the compliance. The ASTM standard recommends measurement of the crack length.

The approximation of fracture toughness is completed based on modified beam theory (MBT), compliance calibration method (CC), or the modified compliance calibration method (MCC), which are described in the following equations. Round robin testing found that the data reduction methods listed here differed by no more than 3.1% in the calculation of G_{1c} [85].

MBT
$$G_1 = \frac{3P\delta}{2ba} \tag{2.27}$$

MBT (crack tip rotation correction)
$$G_1 = \frac{3P\delta}{2b(a + |\Delta|)} \tag{2.28}$$

CC
$$G_1 = \frac{nP\delta}{2ba} \tag{2.29}$$

MCC

$$G_1 = \frac{3P^2C^{2/3}}{2A_1bh} \qquad 2.30$$

These approximations are all based on linear elastic fracture mechanics. A derivation of the CC method is attached in the appendices as the CC method is used in research in this thesis.

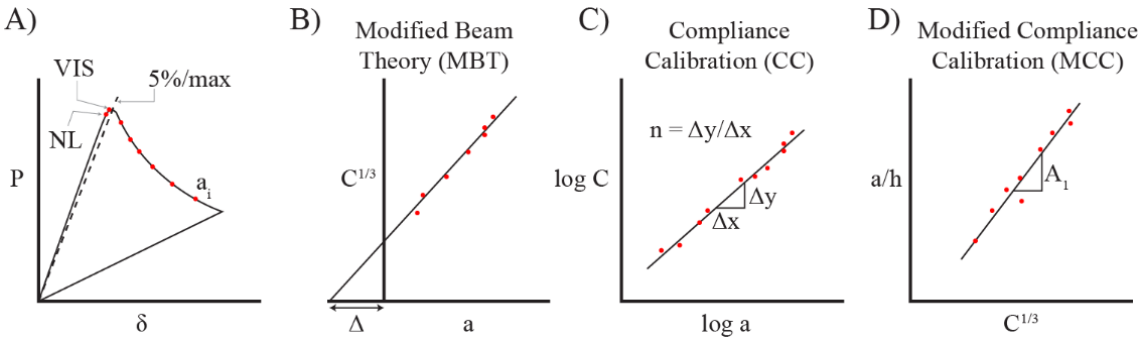

Figure 2-16 Parameters used in ASTM standard detailing mode I fracture of fibre-reinforced laminates [38]. A) Identification of crack initiation using three methods as outlined in ASTM standards. B) Definition of Δ used in Modified Beam Theory. C) Definition of n used in Compliance Calibration method. D) Definition of A_1 used in Modified Compliance Calibration method.

Large displacements effects can be corrected for by applying the parameter F to the calculation of G_{1c}. This parameter accounts for both stiffening of the moment arm and tilting of the end block rotation.

$$F = 1 - \frac{3}{10}\left(\frac{\delta}{a}\right)^2 - \frac{3}{2}\left(\frac{\delta t}{a^2}\right) \qquad 2.31$$

2.5.6 Determination of cohesive laws in the presence of fibre bridging

Sørensen and Jacobsen showed that cohesive law definitions can be obtained by using the J-integral approach [31]. The cohesive laws predicted in this study agree with micro mechanical modelling. This method produced a good agreement for both a fibre cross-over bridging [58] problem and an adhesive joint problem. Sørensen also found that solutions were not obtainable in every case. In particular, it was necessary for the load to be applied via an end moment rather than through a conventional mode I opening [1]. While these findings are interesting in academia, they are less applicable in industry due to the non-standard fracture test method.

The path independent J-integral can characterise the failure process zone under the assumption of bulk elastic behaviour, small strains, small displacements, and no body forces. Evaluating the J-integral locally along the crack faces enclosing the cohesive zone and the crack tip gives equation 2.32 below relating the J-integral in this region J_{loc} to the stress σ, opening δ, end opening δ^* and J-integral around the crack tip J_{tip} (which is typically assumed to be zero).

$$J_{loc} = \int_0^{\delta^*} \sigma(\delta) d\delta + J_{tip} \qquad 2.32$$

The length of the cohesive zone and the end-opening increase as the crack propagates. Thus, the energy uptake of the cohesive zone increases in accordance with equation 2.32. The value of J during crack growth, the fracture resistance J_R, increases as the crack propagates. This is R-curve behaviour as discussed in Section 2.4.4. When δ^* reaches a critical value the R-curve achieves a steady state value, J_{ss}.

$$\frac{\partial J_R}{\partial \delta^*} = \sigma(\delta^*) \qquad 2.33$$

Thus, by recording the J-integral and the end opening of the cohesive zone it is possible to derive the cohesive law.

To use equations 2.32 and 2.33 above, it is necessary to relate J_{loc} to the applied loads. This can be done by evaluating the J-integral along the external boundaries to obtain J_{ext} which is equivalent to J_{loc} due to the path independence of the J-integral. J_{ext} cannot be obtained from LEFM; it must be obtained by analysing the J-integral along the specimen where the cohesive zone is present. In most cases, it cannot be obtained in closed form as J_{ext} depends on the details of the cohesive law. An exception to this is a DCB specimen loaded with pure bending moments, which can be solved analytically as shown by Sørensen [31], yielding the relationship between moment M, beam breadth B, beam height H, Young's modulus E and Poisson's ratio ν.

$$J_{ext} = 12(1-\nu^2)\frac{M^2}{B^2H^3E} \qquad 2.34$$

Thus J_{ext} can be determined by applied moment alone. The end opening is recorded experimentally using an extensometer mounted to the DCB specimen. Hence the cohesive law is defined by measuring (in practice) moment M and end opening δ^*. It should be noted that the test apparatus must apply pure bending moments and J_{ext} cannot be obtained in closed form for the DCB test [83].

2.6 The finite element method

Here, the finite element method (FEM), a numerical approach to solving physical problems by discretising the problem domain into small elements, is discussed. FEM provides a discrete approximation of the differential equations governing a physical problem using numerical methods. This method divides the problem domain into a finite number of nodes/points which are connected to provide a mesh of finite elements [86].

Finite element models are often completed in conjunction with experimental studies to provide additional insight into the problem. These models can be used to (i) validate experimental findings [40,41] (ii) compare to experiments and identify discrepancies (iii) reduce the parameter space needed to explore during physical experiments.

The physical problems solved using FEM typically involve numerical calculation of the force and displacement at each of the nodes; and can also contain temperature and fluid flow effects. Both implicit and explicit solution methods exist and are commonly used. The research in this thesis uses the commercial finite element code ABAQUS with the implicit solver, developed by Dassault Systemes [36].

In general, FEM follows the flowchart shown in Figure 2-17. Equation 2.35 is the characteristic equation of the Finite Element Method. In FEM the force vector F is applied, the stiffness array K is inverted to solve for the displacement vector u [86].

$$Ku = F \qquad 2.35$$

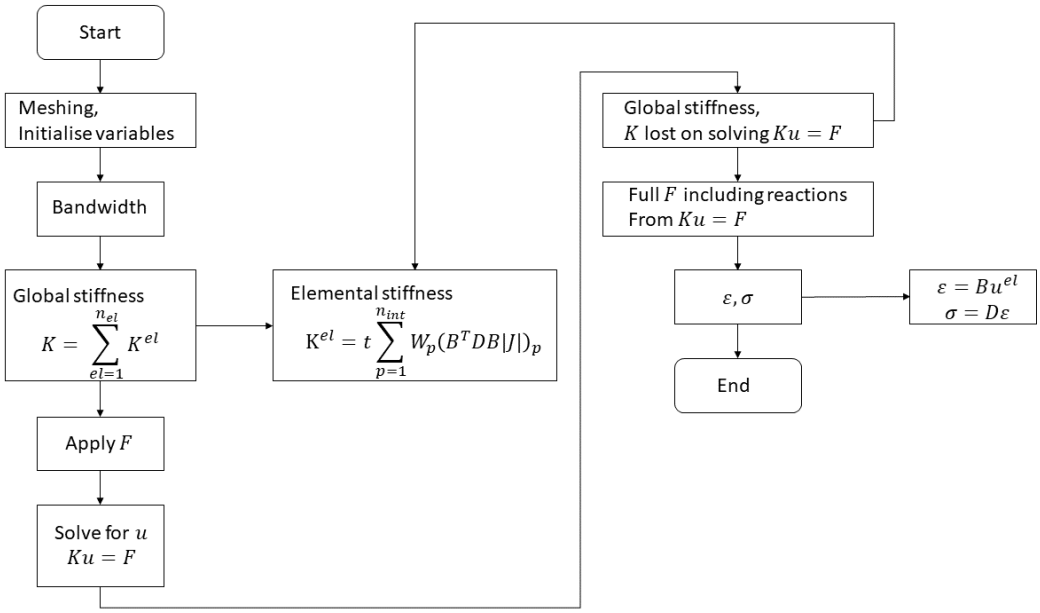

Figure 2-17 Flowchart of the finite element method.

The finite element equation (Equation 2.35) can also be written in elemental form as shown in Figure 2-17; such that $K^{el} = t \sum_{p=1}^{n_{int}} W_p(B^T DB|J|)_p$ where K_{el} is the elemental stiffness, t is the element depth, n_{int} is the number of integration points, p is the current integration point in the summation, W_p is the integration point weighting, B and B^T is the deformation matrix and its transpose, D is the shape function matrix and J is the Jacobian matrix. The full derivation of this is presented by Okereke [86].

The finite element method involves computing element level stiffness expressions which are used to assemble a global stiffness array, K. Boundary conditions are placed in the force vector, F, and the displacement vector, u, Matrix multiplication techniques such as Gaussian elimination or inversion are used to solve the matrix equation (Equation 2.35).

The first step, meshing, discretises the domain into discrete elements. Incorrect meshing can have adverse effects on the results of a FE model. Errors can occur due to the wrong choice of element type for the load case or using a coarse mesh incapable of capturing complex geometric features. A mesh convergence study should always be completed with FEA to ensure

the output results are not sensitive to the mesh used. This ensures that, at a minimum, the number of elements in the model is saturated and the results will not change by refining the mesh further. This study will not remove modelling inaccuracies related to element choice, reduced integration or other modelling choices related to the mesh. Over refining the mesh increases computational expense but does not necessarily increase the accuracy of the measured response.

The global stiffness array contains the stiffness values calculated at an element level. This array is symmetric and can be largely populated with zeros. Once individual elemental stiffness arrays are calculated; each element of that array is placed in the global stiffness array. Their position is based on the node and element number. Depending on the nature of the model (2D or 3D), each element receives 4 or 9 stiffness terms: typically for $x, y, z, xy, xz \,\&\, yz$ terms, forming a symmetric matrix. A global stiffness array entry contains the sum of elemental stiffness terms from overlapping node numbers.

The elemental stiffness array contains one entry for each degree of freedom for each node in the element along the diagonal of the matrix. The off-diagonal terms relate to shear terms if present. Hence for a simple two node truss element in 2D loaded in the x-direction only, the elemental stiffness array has the following shape:

$$k_{local} = \frac{EA}{L}\begin{bmatrix} 1 & 0 & -1 & 0 \\ 0 & 0 & 0 & 0 \\ -1 & 0 & 1 & 0 \\ 0 & 0 & 0 & 0 \end{bmatrix} \qquad 2.36$$

Assuming the nodes in the truss element are numbered 1 and 2, the global stiffness matrix is constructed by adding this local matrix in the correct location. The following global stiffness matrix assumes there is 3 elements in the structure and is hence a 6 by 6 array in 2D.

$$k_{global} = \frac{EA}{L}\begin{bmatrix} 1 & 0 & -1 & 0 & 0 & 0 \\ 0 & 0 & 0 & 0 & 0 & 0 \\ -1 & 0 & 1 & 0 & 0 & 0 \\ 0 & 0 & 0 & 0 & 0 & 0 \\ 0 & 0 & 0 & 0 & 0 & 0 \\ 0 & 0 & 0 & 0 & 0 & 0 \end{bmatrix} \quad 2.37$$

The same process is repeated for each element in the structure to fully populate the global stiffness matrix.

The bandwidth (calculated after mesh generation) is an indication of the speed with which an analysis will run. The bandwidth of a finite element analysis is computed from the global stiffness matrix. The bandwidth is equal to the maximum length along a row of the global stiffness matrix which is populated with non-zero entries. Commercial finite element codes run optimisation scripts which renumber nodes and elements in a simulation to minimise the bandwidth and provide a more efficient solution, as entries to the global stiffness array are based on node and element number.

In the case of non-linear solutions, i.e. using the Newton-Raphson method, it is useful to write the finite element equation in terms of a residual:

$$\int_V B^T(u_e)\sigma(u_e)dV - F = G(u_e) = 0 \quad 2.38$$

Where $B^T$is the transpose of the deformation matrix, u_e is the element deformation, σ is the stress, V is the element volume, F is the force vector and $G(u_e)$ gives us the residual forces vector.

Applying the Newton-Raphson method to this function gives

$$u_{i+1}^{t+\Delta t} = u_i^{t+\Delta t} - \left[\frac{\partial G\left(u_i^{t+\Delta t}\right)}{\partial u}\right]^{-1} G(u_i^{t+\Delta t}) \quad 2.39$$

Where i is the current increment, t is the current time, Δt is a small time increment.

This can be rewritten as:

$$K\left(u_i^{t+\Delta t}\right) = \left[\frac{\partial G\left(u_i^{t+\Delta t}\right)}{\partial u}\right] \qquad 2.40$$

$$K\left(u_i^{t+\Delta t}\right)\partial u_{i+1} = G\left(u_i^{t+\Delta t}\right)$$

Where K is the stiffness array. This form of the finite element equation is useful as it describes the behaviour from one increment to the next. In general, FE analyses contain numerous increments and iterations. An increment spans from one time point in the analysis to the next. Inside an increment there may be numerous iterations required to achieve a state of equilibrium. If the expected response is achieved immediately only one iteration is required; but if the expected response is not achieved in the first iteration the solver will reiterate to achieve an acceptable response. This iterative solving can be done using implicit or explicit techniques.

The implicit solution method provides a Newton-Raphson approximation of the measured response, shown in Figure 2-18. In this approximation, an initial estimate is used to approximate the response of an element. Subsequent iterations minimise the error in the response. This method is preferred to explicit solutions as a finite number of iterations will achieve the physical response. However, there are applications where this technique is not possible and explicit solvers must be used.

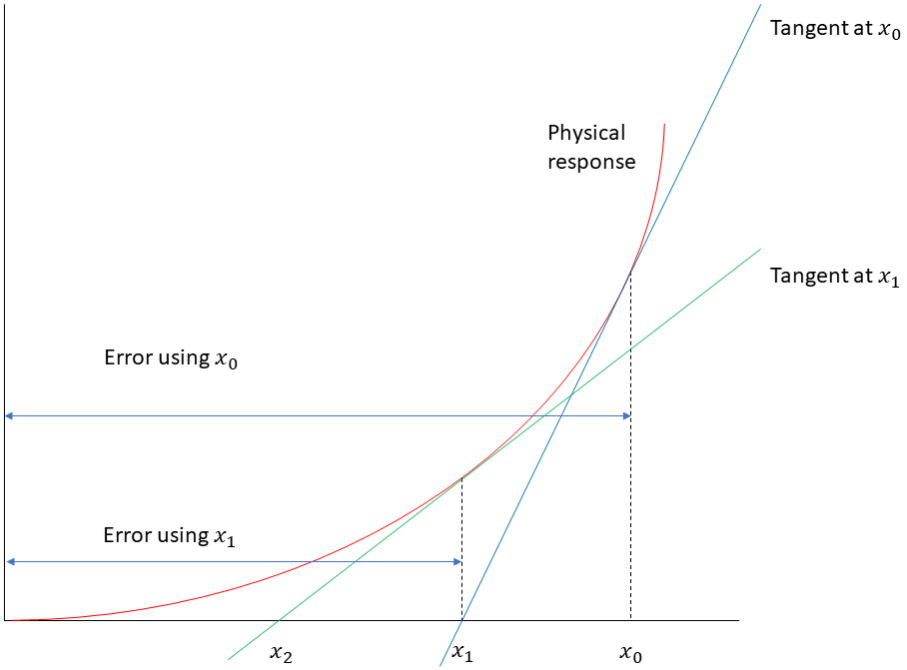

Figure 2-18 Newton-Raphson method of approximating the measured response

Under impact or dynamic loading, the rate of change of the response is typically too high to solve using the implicit method (obtaining a converged solution is not possible), hence explicit solvers are used. Explicit solvers perform a time integration that is analogous to Euler's method:

$$y_{n+1} = y_n + hf(t_n, y_n) \qquad 2.41$$

Where y_n is an approximation to the solution of the ordinary differential equation at time t_n. And h is the time increment size, such that $h = t_{n+1} - t_n$.

The time increment must be less than a stable time increment which is set by the time taken for a stress wave to propagate though the smallest elements in the model.

$$\Delta t \leq min\ (L_e \sqrt{\frac{\rho}{\lambda + 2\mu}}) \qquad 2.42$$

Where L_e is the characteristic length associated with an element, ρ is the density of the material, and λ and μ are Lamé's constants for the material (which are a function of Poisson's ratio and Young's modulus).

Mass scaling can be used to facilitate use of a larger time increment (and thus solve quasi static problems) provided the effects of inertia can be kept negligible.

This technique can be computationally less expensive than the implicit method and can be used when sudden changes in response are present, such as impact events or when discontinuities/sharp changes in response are present. Explicit solvers also scale better on HPC clusters and are often used on very large meshes, for example with aerospace and automotive assemblies. However, the accuracy of these results should always be validated.

2.6.1 Interface related theory

As this thesis is concerned with interfacial behaviour of composite materials undergoing fracture, methods of handling interfacial separation in FEM are discussed herein. When modelling interfaces such as cracks or voids for example, the behaviour of these regions differs from the rest of the model. Continuum elements are typically used in the main mesh in a model; and cohesive elements or cohesive surfaces are used to model interfacial behaviour. This research uses cohesive elements (with the behaviour of these elements governed through a traction separation law (TSL)) however similar theory applies for cohesive surfaces. Interfacial behaviour can also be modelled using other techniques, such as cohesive surfaces and spring elements [36].

Cohesive surfaces work in a similar manner to cohesive elements, with the interfacial behaviour of the surfaces defined by a traction separation law. When using cohesive surfaces, there are no elements along the interface. Hence elemental data cannot be extracted directly from the interface.

Spring elements can couple a force with a relative displacement. The spring constant can be specified as a function of displacement, which allows damage to be captured.

2.6.2 Cohesive elements

Cohesive elements are commonly used to define interfacial behaviour in FE simulations. These elements typically have no initial thickness or a small finite thickness (and use a unit thickness in the material response) and are capable of handling large displacements. Advantages of cohesive elements over cohesive surfaces include the presence of an integration point in the cohesive element (which allows simple extraction of data from the interface such as stress and strain), and a reduced computational cost as the contact tracking is implemented in the global stiffness array. The response of cohesive elements is defined by a TSL, which is user defined. The number of parameters defining a TSL increases with increasing complexity of response at the interface.

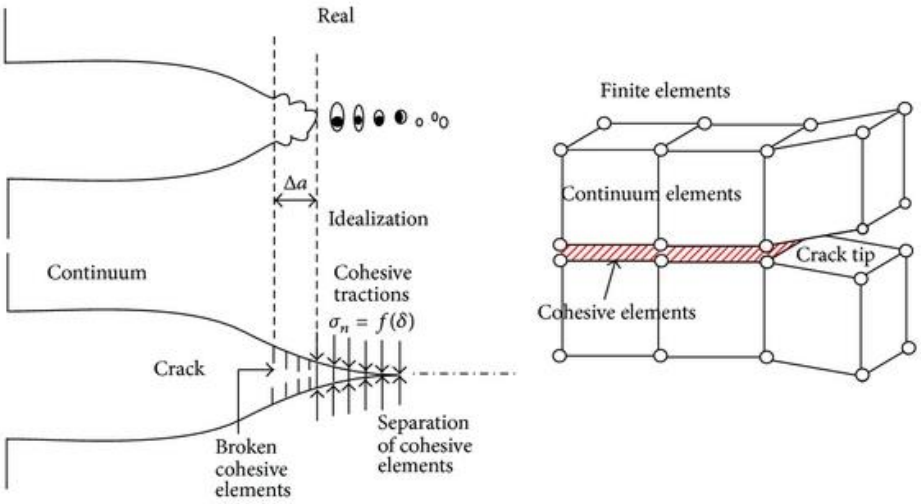

Figure 2-19 The fracture process using cohesive elements to capture the interfacial behaviour in a finite element simulation. Image source: [87]

Cohesive elements are capable of accurately capturing crack propagation. During crack propagation, the local elemental damage is defined (by the traction separation law) based on the separation experienced by the element. Cohesive elements typically behave linearly elastic until damage initiation. Although a traction separation law uses stress and displacement, strain is used in the constitutive matrix by means of a constitutive thickness, with a default value of one [36]:

$$\varepsilon_n = \frac{\delta_n}{T_0} \quad \varepsilon_s = \frac{\delta_s}{T_0} \quad \varepsilon_t = \frac{\delta_t}{T_0} \qquad 2.43$$

Where ε is the nominal strain, δ is the displacement and T_0 is the constitutive thickness. Subscripts n, s and t denote the normal, shear and tangential directions respectively.

The behaviour of the cohesive element after this initial linear elastic response is dependent on the damage profile of the material. After this elastic response, damage in the cohesive elements begins to accumulate and the traction is calculated as a function of the damage.

$$\sigma = \sigma_e(1 - D) \qquad 2.44$$

Where σ is the elemental stress, σ_e is the elemental elastic stress (stress experienced if damage is not present), and D is the damage.

2.6.3 The Traction Separation relationship

The TSL, as shown in shown in Figure 2-20, describes the traction exerted between two debonding surfaces based on the local displacement between the surfaces. The TSL affects the macroscopic material behaviour such as load displacement, crack growth and resulting R-curve behaviour which relates measured fracture energy to crack propagation.

The shape of the TSL is critical in determining the R-curve that will be produced by a simulation. There are several TSL shapes explored in the literature including trapezoidal commonly seen in stiff materials such as concrete [88], bilinear [49], trilinear [89] and a continuously changing function [41]. It has been found that a bilinear traction separation law (Figure 2-20A) is only capable to capture the initial stages of fibre bridging [37,42,50]; whereas a trilinear law (Figure 2-20B) is capable of capturing high levels of displacement typically found with fibre bridging [41,50,90].

When considering composite materials, with a large degree of extrinsic toughening, the TSL can be categorised by three regions; namely the initial linear elastic response, the cohesive fracture stage where a large amount of

damage is accumulated over a small displacement, and the fibre bridging stage where a small traction is exerted between the surfaces over a relatively large separation. The initial elastic response and the cohesive fracture zone are related to intrinsic toughening mechanisms. The fibre bridging region models extrinsic toughening mechanisms which act behind the crack tip.

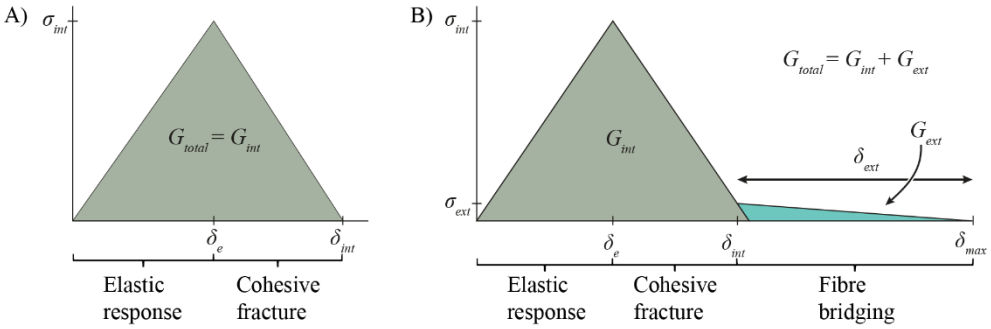

Figure 2-20 General shape of a traction separation law. A) without fibre bridging present (Bilinear). B) with fibre bridging present (Trilinear). In the case of fibre bridging $\delta_{ext} \gg \delta_e$ or δ_{int}. (Note: δ_{int} definition can vary but the area change is negligible.)

In experimental work, the measured fracture toughness $\hat{G}$ is approximated as detailed in section 2.5.4.1. In computational work, the fracture toughness can be defined in more detail. $\hat{G}$ is the measured fracture toughness which is approximated in the same manner as experimentally; but there is now also the fracture energy input into a finite element model, G_0, equivalent to the total area under a traction separation law. This fracture energy is further categorised as intrinsic energy, G_{int}, and extrinsic energy, G_{ext}, responsible for the respective toughening mechanisms. The definition here varies slightly as the transition from intrinsic to extrinsic toughening is not exact; in this thesis, the intrinsic and extrinsic energies are calculated by equations 2.45 and 2.46 respectively.

$$G_{int} \cong \frac{1}{2}\sigma_{int}\delta_{int} \qquad 2.45$$

$$G_{ext} \cong \frac{1}{2}\sigma_{ext}\delta_{ext} \qquad 2.46$$

Where all symbols are defined in Figure 2-20.

In composite materials, the sharp changes in slope are a good approximation as the intrinsic region occurs over such a small displacement and at a high strength. To overcome sharp peaks in the traction separation law, viscous damping is commonly introduced to the model. This acts in a similar manner as damping in a mechanical system. The introduction of a viscous term in the DCB model aids convergence. A similar approach is taken when investigating damping in the roller model in Chapter 4.

Determining the parameters for a traction separation law is not always straight forward. The J-integral is commonly used, but it typically assumes there is no loading on the crack surface and is difficult to implement in an industry setting. Heidari-Rarani details their justification for a maximum traction σ_m for different cases [40]. But there is no direct guide to fully define a traction separation law based on experimental observations. There has been no systematic exploration of the parameter space associated with a traction separation law.

There has been some research into experimental calculation of traction separation laws, however they are specimen dependent. Zhu, et al. propose a method of measuring traction separation laws using their experimental set up. [91]. However, this method requires the use of the J-integral, making it difficult to implement in an industry setting.

2.7 Conclusions

In this chapter, an overview of composite behaviour and fracture mechanics, with emphasis on fracture in composites, was given. While previous studies have modelled crack growth computationally, the presence of fibre bridging means many assumptions made in the underlying theories are no longer valid. Previous work [37,42,50,52,90,92] has found that computational results can replicate the results in an experimental procedure with fibre bridging present; however these works have not shown the effect of the computational parameters on the fit between numerical and experimental results. It is unclear how these studies choose their traction separation law

or whether other laws would give similar results. This forms the main motivation for the work in Chapter 3, which aims to provide an in-depth exploration of the traction separation law parameter space, which provides insight into how to select the cohesive parameters for a traction separation law with extrinsic toughening based on experimental observations in a standardised DCB test.

Detailed measurements of the tractions generated by fibre bridging are difficult to measure. Previous work has used approaches such as the J-integral to calculate tractions; however, both the analysis and collection of data are difficult. The J-integral cannot be applied in closed form to a standard DCB test, it must be applied to a DCB specimen loaded with pure bending moments to provide an analytical solution. There is a distinct need for a method of measuring a material's fracture energy that accounts for high levels of extrinsic toughness, while still being capable of use in an industry setting. The work in Chapters 4 and 5 seek to develop methods that can be quickly used to evaluate the role of fibre bridging and create traction separation laws for use in computational models.

2.8 References

[1] Holmes JW, Liu L, Sørensen BF, Wahlgren S. Experimental approach for mixed-mode fatigue delamination crack growth with large-scale bridging in polymer composites. J Compos Mater 2014;48:3111–28. https://doi.org/10.1177/0021998313507613.

[2] Yao L, Alderliesten R, Zhao M, Benedictus R. Bridging effect on mode I fatigue delamination behavior in composite laminates. Compos Part A 2014;63:103–9. https://doi.org/10.1016/j.compositesa.2014.04.007.

[3] Iarve E V, Hoos K, Braginsky M, Zhou E, Mollenhauer DH. Progressive failure simulation in laminated composites under fatigue loading by using discrete damage modeling. J Compos Mater 2016;0:1–19. https://doi.org/10.1177/0021998316681831.

[4] Borotto M. Bridging effects on Mixed Mode delamination : experiments and numerical simulation. École Polytechnique Fédérale de Lausanne, 2016. https://doi.org/10.5075/epfl-thesis-7056.

[5] Labuschagne A, van Rensburg NFJ, van der Merwe AJ. Comparison of linear beam theories. Math Comput Model 2009;49:20–30. https://doi.org/10.1016/j.mcm.2008.06.006.

[6] Li G, Jia J, Chen G. Solving Large-Deflection Problem of Spatial Beam with Circular Cross-Section Using an Optimization-Based Runge–Kutta Method. Int J Nonlinear Sci Numer Simul 2016;17. https://doi.org/10.1515/ijnsns-2015-0053.

[7] Barari A, Kaliji HD, Ghadim M, Domairry G. Non-linear vibration of Euler-Bernoulli beams. Lat Am J Solids Struct 2011;8:139–48. https://doi.org/10.1590/S1679-78252011000200002.

[8] Cowper GR. The Shear Coefficient in Timoshenko's Beam Theory. 1Journal Appl Mech 1966.

[9] Vasic S, Smith I. Bridging crack model for fracture of spruce. Eng Fract Mech 2002;69:745–60. https://doi.org/10.1016/S0013-7944(01)00091-1.

[10] Ammann S, Niemz P. FIBRE AND ADHESIVE BRIDGING AT GLUE JOINTS IN EUROPEAN BEECH WOOD. Wood Res 2014;59:303–12.

[11] Comley K, Fleck NA. The toughness of adipose tissue: measurements and physical basis. J Biomech 2010;43:1823–6. https://doi.org/10.1016/j.jbiomech.2010.02.029.

[12] Tonsomboon K, Koh CT, Oyen ML. Time-dependent fracture toughness of cornea. J Mech Behav Biomed Mater 2014;34:116–23. https://doi.org/10.1016/j.jmbbm.2014.01.015.

[13] Soutis C. Fibre reinforced composites in aircraft construction. Prog Aerosp Sci 2005;41:143–51. https://doi.org/10.1016/j.paerosci.2005.02.004.

[14] Cadogan D, Stein J, Grahne M. Inflatable composite habitat structures for lunar and mars exploration. Acta Astronaut 1999;44:399–406. https://doi.org/10.1016/S0094-5765(99)00103-4.

[15] Cataldo F, Prata M. Neutron radiation shielding composites for deep space exploration: An introduction. Elsevier Ltd.; 2020. https://doi.org/10.1016/b978-0-12-819459-1.00010-6.

[16] Smith GF. Design and production of composites in the automotive industry. Compos Manuf 1990;1:112–6. https://doi.org/10.1016/0956-7143(90)90246-S.

[17] De Santis R, Gloria A, Ambrosio L. Composite materials for hip joint prostheses. Biomed Compos 2009:276–95. https://doi.org/10.1533/9781845697372.2.276.

[18] Vasiliev V V, V ME. Advanced Mechanics of Composite Materials and Structures (Fourth Edition). Chapter 1. Mechanics of a Unidirectional Ply. 2018. https://doi.org/https://doi.org/10.1016/B978-0-08-102209-2.00001-3.

[19] Aamir M, Tolouei-Rad M, Giasin K, Nosrati A. Recent advances in drilling of carbon fiber reinforced polymers for aerospace applications: A review. Int J Adv Manuf Technol 2019.

[20] Argon AS, Cohen RE. Toughenability of polymers. Polymer (Guildf) 2003;44:6013–32. https://doi.org/10.1016/S0032-3861(03)00546-9.

[21] Cepeda-Jiménez CM, Pozuelo M, García-Infanta JM, Ruano OA, Carreño F. Influence of the alumina thickness at the interfaces on the fracture mechanisms of aluminium multilayer composites. Mater Sci Eng A 2008;496:133–42. https://doi.org/10.1016/j.msea.2008.05.015.

[22] Liu L, Jia C, He J, Zhao F, Fan D, Xing L, et al. Interfacial characterization, control and modification of carbon fiber reinforced polymer composites. Compos Sci Technol 2015;121:56–72. https://doi.org/10.1016/j.compscitech.2015.08.002.

[23] Liu B, Huang L, Geng L, Yin F. Multiscale Hierarchical Structure and Laminated Strengthening and Toughening Mechanisms. Lamination - Theory Appl 2018. https://doi.org/10.5772/intechopen.69976.

[24] Griffith AA. The phenomena of rupture and flow in solids. Philos Trans R Soc London Ser A 1921;221:163–98.

[25] Zehnder AT. Encyclopedia of Tribology. 2013. https://doi.org/10.1007/978-0-387-92897-5.

[26] Sorem WA, Dodds Jr. RH, Rolfe ST. Effects of crack depth on elastic-plastic fracture toughness. Int J Fract 1991;47:105–126.

[27] Orowan E. Fracture and strength of solids. Rep Prog Phys 1949;12. https://doi.org/10.1088/0034-4885/77/5/056502.

[28] Irwin G. Analysis of stresses and strains near the end of a crack traversing a plate. J Appl Mech 1957;24:361–4.

[29] Sills RB, Thouless MD. Cohesive-length scales for damage and toughening mechanisms. Int J Solids Struct 2015. https://doi.org/10.1016/j.ijsolstr.2014.06.010.

[30] Rice JR. A Path Independent Integral and the Approximate Analysis of Strain Concentration by Notches and Cracks. J Appl Mech 1968;35:379–86.

[31] Sørensen BF, Jacobsen TK. Determination of cohesive laws by the J integral approach. Eng Fract Mech 2003;70:1841–58. https://doi.org/10.1016/S0013-7944(03)00127-9.

[32] Lee RF, Donovan JA. J-Integral and Crack Opening Displacement as Crack Initiation Criteria in Natural Rubber in Pure Shear and Tensile Specimens. Rubber Chem Technol 1987;60:674–88.

[33] Eshelby JD. The Continuum Theory of Lattice Defects. Solid State Phys 1956;3:79–144.

[34] Hutchinson JW. Singular Behaviour At the end of a Tensile Crack in a Hardeningf Material. J Mech Phys Solids 1968;16:13–31.

[35] Kammer DS. Slip Fronts at Frictional Interfaces : A Numerical and Theoretical Study par. EPFL, 2014. https://doi.org/10.5075/epfl-thesis-6492.

[36] Systemes D. Abaqus user manual 2010:Section 29.5.6.

[37] Davidson P, Waas AM. Non-smooth mode I fracture of fibre-reinforced composites: an experimental, numerical and analytical study. Philos Trans R Soc A 2012;370:1942–65. https://doi.org/10.1098/rsta.2011.0381.

[38] ASTM. Standard Test Method for Mode I Interlaminar Fracture Toughness of Unidirectional Fiber-Reinforced Polymer Matrix Composites 1 2013. https://doi.org/10.1520/D5528-13.

[39] Gutierrez-Lemini D. The initiation J -integral for linear viscoelastic solids with constant Poisson's ratio. Int J Fract 2002;113:27–37.

[40] Heidari-Rarani M, Shokrieh MM, Camanho PP. Finite element modeling of mode I delamination growth in laminated DCB specimens with R-curve effects. Compos Part B Eng 2013;45:897–903. https://doi.org/10.1016/j.compositesb.2012.09.051.

[41] Shokrieh MM, Salamat-Talab M, Heidari-Rarani M. Effect of initial crack length on the measured bridging law of unidirectional E-glass/epoxy double cantilever beam specimens. Mater Des 2014;55:605–11. https://doi.org/10.1016/j.matdes.2013.09.064.

[42] Gutkin R, Laffan ML, Pinho ST, Robinson P, Curtis PT. Modelling the R-curve effect and its specimen-dependence. Int J Solids Struct 2011;48:1767–77. https://doi.org/10.1016/j.ijsolstr.2011.02.025.

[43] Noels L. Fracture Mechanics Online Class. Univ Liége 2015.

[44] Carolan D, Ivankovic A, Kinloch AJ, Sprenger S, Taylor AC. Toughened carbon fibre-reinforced polymer composites with nanoparticle-modified epoxy matrices. J Mater Sci 2017;52:1767–88. https://doi.org/10.1007/s10853-016-0468-5.

[45] Li V. Can Concrete Be Bendable? Am Sci 2012;100.

[46] Fotouhi M, Ahmadi Najafabadi M. Investigation of the mixed-mode delamination in polymer-matrix composites using acoustic emission technique. J Reinf Plast Compos 2014;33:1767–82. https://doi.org/10.1177/0731684414544391.

[47] Osada T, Watabe A, Yamamoto J, Brouwer JC, Kwakernaak C, Ozaki S, et al. Full strength and toughness recovery after repeated cracking and healing in bone-like high temperature ceramics. Sci Rep 2020;10.

[48] Yashiro S, Yamasaki T, Nagai H, Yoshimura A. Effect of material nonlinearity on the toughness evaluation in quasi-static mode II interlaminar fracture toughness tests of composite laminates. Eng Fract Mech 2021:107879. https://doi.org/10.1016/j.engfracmech.2021.107879.

[49] Meo M, Thieulot E. Delamination modelling in a double cantilever beam. Compos Struct 2005;71:429–34. https://doi.org/10.1016/j.compstruct.2005.09.026.

[50] De Morais AB. A new fibre bridging based analysis of the Double Cantilever Beam (DCB) test. Compos Part A Appl Sci Manuf 2011;42:1361–8. https://doi.org/10.1016/j.compositesa.2011.05.019.

[51] De Morais AB. Double cantilever beam testing of multidirectional laminates. Compos Part A Appl Sci Manuf 2003;34:1135–42. https://doi.org/10.1016/j.compositesa.2003.08.008.

[52] Manshadi BD, Farmand-Ashtiani E, Botsis J, Vassilopoulos AP. An iterative analytical/experimental study of bridging in delamination of the double cantilever beam specimen. Compos Part A 2014;61:43–50. https://doi.org/10.1016/j.compositesa.2014.02.001.

[53] Gokgol C, Basdogan C, Canadinc D. Estimation of fracture toughness of liver tissue: Experiments and validation. Med Eng Phys 2012;34:882–91. https://doi.org/10.1016/j.medengphy.2011.09.030.

[54] Comley K, Fleck NA. A micromechanical model for the Young's modulus of adipose tissue. Int J Solids Struct 2010;47:2982–90. https://doi.org/10.1016/j.ijsolstr.2010.07.001.

[55] Shahmansouri N, Cartier R, Mongrain R. Characterization of the toughness and elastic properties of fresh and cryopreserved arteries. J Biomech 2015;48:2205–9. https://doi.org/10.1016/j.jbiomech.2015.03.033.

[56] Parmigiani JP, Thouless MD. The roles of toughness and cohesive strength on crack deflection at interfaces. J Mech Phys Solids 2006;54:266–87. https://doi.org/10.1016/j.jmps.2005.09.002.

[57] Li S, Thouless MD, Waas AM, Schroeder JA, Zavattieri PD. Use of mode-I cohesive-zone models to describe the fracture of an adhesively-bonded polymer-matrix composite. Compos Sci Technol 2005;65:281–93. https://doi.org/10.1016/j.compscitech.2004.07.009.

[58] Sørensen BF, Gamstedt EK, Østergaard RC, Goutianos S. Micromechanical model of cross-over fibre bridging – Prediction of mixed mode bridging laws. Mech Mater 2008;40:220–34. https://doi.org/10.1016/j.mechmat.2007.07.007.

[59] Spearing SM, Evans AG. The role of fiber bridging in the delamination resistance of fiber-reinforced composites. Acta Metall Mater 1992;40:2191–9. https://doi.org/10.1016/0956-7151(92)90137-4.

[60] Sørensen BF. Micromechanical model of the single fiber fragmentation test. Mech Mater 2017;104:38–48. https://doi.org/10.1016/j.mechmat.2016.10.002.

[61] De Morais AB, Pereira AB. Application of the effective crack method to mode I and mode II interlaminar fracture of carbon/epoxy unidirectional

laminates. Compos Part A 2007;38:785–94. https://doi.org/10.1016/j.compositesa.2006.09.001.

[62] Laffan MJ. Testing the toughness of polymer matrix composites. Fail Mech Polym Matrix Compos Criteria, Test Ind Appl 2012:110–28. https://doi.org/10.1016/B978-1-84569-750-1.50005-7.

[63] Morais JJL, de Moura MFSF, Pereira FAM, Xavier J, Dourado N, Dias MIR, et al. The double cantilever beam test applied to mode I fracture characterization of cortical bone tissue. J Mech Behav Biomed Mater 2010;3:446–53. https://doi.org/10.1016/j.jmbbm.2010.04.001.

[64] Kawashita LF, Moore DR, Williams JG. Protocols for the Measurement of Adhesive Fracture Toughness by Peel Tests Protocols for the Measurement of Adhesive Fracture Toughness by Peel Tests. J Adhes 2006;82:973–95. https://doi.org/10.1080/00218460600876142.

[65] Kawashita LF, Moore DR, Williams JG. Analysis of peel arm curvature for the determination of fracture toughness in metal-polymer laminates. J Mater Sci 2005;40:4541–8. https://doi.org/10.1007/s10853-005-0856-8.

[66] Grouve WJB, Warnet LL, Akkerman R. Critical assessment of the mandrel peel test for fiber reinforced thermoplastic laminates. Eng Fract Mech 2013;101:96–108. https://doi.org/10.1016/j.engfracmech.2012.07.005.

[67] Minnetyan L, Chamis C. The Compact Tension, C(T), Specimen in Laminated Composite Testing. Compos Mater Fatigue Fract (Sixth Vol 2009:531-531–20. https://doi.org/10.1520/stp19946s.

[68] Slepetz JM, Carlson L. Fracture of Composite Compact Tension Specimens. Am Soc Test Mater 1975.

[69] Costa M, Carbas R, Benedita M, Marques E, Viana G, Da Silva LFM, et al. Static assessment of the mixed-mode behaviour of three epoxy adhesives. Eng Fract Mech 2017;182:552–65. https://doi.org/10.1016/j.engfracmech.2017.05.028.

[70] De Morais AB, De Moura MFSF. Assessment of initiation criteria used in interlaminar fracture tests of composites. Eng Fract Mech 2005;72:2615–27. https://doi.org/10.1016/j.engfracmech.2005.05.003.

[71] Yoshihara H, Satoh A. Shear and crack tip deformation correction for the double cantilever beam and three-point end-notched flexure specimens for mode I and mode II fracture toughness measurement of wood. Eng Fract Mech 2009;76:335–46. https://doi.org/10.1016/j.engfracmech.2008.10.012.

[72] Sekulic A. Experimental Identification of Adhesive Properties between Epoxy and Glass. EPFL, 2008. https://doi.org/10.5075/epfl-thesis-4001.

[73] Wang TWH, Blum FD, Dharani LR. Effect of interfacial mobility on flexural strength and fracture toughness of glass/epoxy laminates. J Mater Sci 1999;34.

[74] Davidson BD, Teller SS. Recommendations for an ASTM standardized test for determining G IIc of unidirectional laminated polymeric matrix composites. J ASTM Int 2010;7. https://doi.org/10.1520/JAI102619.

[75] ASTM. Standard Test Method for Measurement of Fracture Toughness. ASTM Stand 2019:E 1820 – 01. https://doi.org/10.1520/E1820-18AE01.

[76] Conshohocken W. Standard Test Method for 90 Degree Peel Resistance of Adhesives 1 2019;11:1–6. https://doi.org/10.1520/D6862-11R16.adherends.

[77] Standard Test Method for Peel resistance of adhesives (T-Peel test) 2015. https://doi.org/10.1520/D1876-08R15E01.

[78] ASTM D7905. Standard test method for determination of the mode II interlaminar fracture toughness of unidirectional fiber-reinforced polymer matrix composites. Astm 2014;i:1–18. https://doi.org/10.1520/D7905.

[79] Shokrieh MM, Salamat-talab M, Heidari-Rarani M. Effect of interface fiber angle on the R-curve behavior of E-glass/epoxy DCB specimens. Theor Appl Fract Mech 2016;86. https://doi.org/10.1016/j.tafmec.2016.06.006.

[80] Joki RK, Grytten F, Hayman B, Sørensen BF. A mixed mode cohesive model for FRP laminates incorporating large scale bridging behaviour. Eng Fract Mech 2020;239:107274. https://doi.org/10.1016/j.engfracmech.2020.107274.

[81] Barenblatt GI. The Mathematical Theory of Equilibrium Cracks in Brittle Fracture. Adv Appl Mech 1962;7:55–129.

[82] Cox B, Marshall D. Concepts for bridged cracks in fracture and fatigue. Mater Sci 1994.

[83] Suo Z, Bao G, Fan B. Delamination R-curve phenomena due to damage. J Mech Phys Solids 1992;40:1–16.

[84] ISO. Adhesives — Determination of the mode 1 adhesive fracture energy of structural adhesive joints using double cantilever beam and tapered double cantilever beam specimens. ISO 25217 2009.

[85] O'Brien TK, Martin RH. Results of ASTM Round Robin Testing for Mode I Interlaminar Fracture Toughness of Composite Materials. J Compos Technol Res 1993;15.

[86] Okereke M, Keates S. Finite Element Applications A Practical Guide to the FEM Process. 2018.

[87] Liong RT, Proppe C. Finite element multibody simulation of a breathing crack in a rotor with a cohesive zone model. ISRN Mech Eng 2013;2013. https://doi.org/10.1155/2013/249035.

[88] Elices M, Guinea G V., Omez JG, Planas J. The cohesive zone model: advantages, limitations and challenges. Eng Fract Mech 2002;69:137–63. https://doi.org/https://doi.org/10.1016/S0013-7944(01)00083-2.

[89] Mirzaei B, Sinha A, Nairn JA. Measuring and modeling fiber bridging: Application to wood and wood composites exposed to moisture cycling. Compos Sci Technol 2016;128:65–74. https://doi.org/10.1016/j.compscitech.2016.03.017.

[90] Blackman BRK, Hadavinia H, Kinloch AJ, Paraschi M, Williams JG. The calculation of adhesive fracture energies in mode I: revisiting the tapered double cantilever beam (TDCB) test. Eng Fract Mech 2003;70:233–48. https://doi.org/10.1016/S0013-7944(02)00031-0.

[91] Zhu Y, Liechti KM, Ravi-Chandar K. Direct extraction of rate-dependent traction–separation laws for polyurea/steel interfaces. Int J Solids Struct 2009;46:31–51. https://doi.org/10.1016/j.ijsolstr.2008.08.019.

[92] Airoldi A, Dávila CG. Identification of material parameters for modelling delamination in the presence of fibre bridging. Compos Struct 2012;94:3240–9. https://doi.org/10.1016/j.compstruct.2012.05.014.

Chapter 3. Fibre bridging: Continuum modelling of extrinsic toughening in Double Cantilever Beams

Abstract

Extrinsic toughening, such as fibre bridging, acts behind the crack tip to increase toughness in composite laminates. Computational studies have captured this phenomenon; however, the uniqueness of fit between computational results (which vary based on the interface traction-separation relationship) and experimental results has not been explored in detail. Here, detailed exploration of the parameter space for various traction-separation laws (TSL) using finite elements is presented to investigate the role of fibre bridging.

In the absence of extrinsic toughening, a linear softening TSL is sufficient to capture the key R-curve features, the total input fracture energy is of primary importance. Where extrinsic toughening is present, the ratio between intrinsic and extrinsic energy dictates the shape of the crack growth resistance curve (where fracture toughness (energy) increases with increasing crack growth). The influence of fibre bridging length on the crack growth required to reach a plateau in toughness is examined. A strategy for determining key cohesive properties from a double cantilever beam test is presented and applied to experimental results.

Nomenclature

a	Crack length
a_0	Pre-crack length
Δa_{ss}	Crack length to achieve steady-state distribution of fibres
b	Beam width
E	Young's modulus
G_{total}	Total fracture energy
G_{ext}	Extrinsic fracture energy
G_{int}	Intrinsic fracture energy
$\hat{G}$	Observed fracture energy
$\hat{G}_0$	The initial value of fracture toughness on a resistance curve (R-curve)
$\hat{G}_{ss}$	Plateau value of fracture toughness on a R-curve
h	Beam thickness (one laminate)
L	Beam length
L_{el}	Length of one side of an element
n	Linear regression fitting parameter for compliance calibration method
P	Load
u	Load-line displacement
δ_e	Traction-separation law length for elastic damage
δ_{int}	Traction-separation law length for intrinsic behaviour
δ_{ext}	Traction-separation law length for fibre bridging
δ_{max}	Traction-separation law maximum length
σ_{int}	Maximum allowable traction
σ_{ext}	Fibre bridging maximum traction
$\sigma_{yt,\ 90°}$	Transverse ply tensile strength

3.1 Introduction

Composite materials composed from stacked layers of continuous fibres, embedded within a polymeric matrix provide high specific strength and stiffness properties. As such, composites find increasing use in aircraft structures, automotive components, and wind turbine blades. A direct consequence of motion is a greater susceptibility to impact loads; if this includes a cyclical element, fatigue life can also be of concern. Both impact and fatigue can result in delamination between the stacked layers of the composite. Both intrinsic and extrinsic toughening mechanisms (which act ahead of the crack tip and behind the crack tip, respectively, as seen in Figure 3-1B) influence the onset and progression of failures [1–3].

3.1.1 Intrinsic and extrinsic toughening

Intrinsic toughening mechanisms act ahead of the crack tip and extrinsic toughening mechanisms act behind the crack tip (see Figure 3-1B); however, the definition of the crack tip can vary significantly. The terms *'damage'* and *'toughening'* can describe the same phenomena depending on the crack tip definition [4]. Sills and Thouless also suggest that a change in cohesive length scale can be used to define the transition from intrinsic to extrinsic toughening [4].

The role of intrinsic toughening mechanisms in traditional engineering materials is well studied, for example, micro-matrix cracking [5]. Other examples of intrinsic mechanisms include: plasticity ahead of a crack tip in steels and other ductile metals [6,7], crack deflection by secondary phases [8]; crack bifurcations [9] and void coalescence [10]. In composites, the intrinsic toughness is dictated by the resin properties [11], fibre volume fraction [12], and the mean fibre diameter [13]

Extrinsic toughening mechanisms act behind the crack tip to increase fracture toughness. Of particular relevance to composite materials is fibre bridging, an extrinsic toughening mechanism whereby fibres from neighbouring plies remain attached to both delaminated layers. This

generates a traction across the crack and, hence, raises the energy required to advance the crack front. This effect can act over a large separation, as found in Carbon Fibre Reinforced Polymers (CFRP) composites [14], or a short separation, as found in biological tissue [15]. Fibre bridging acting over a seemingly short distance still significantly affects the evolution of fracture toughness. The role fibre bridging plays in crack deflection is difficult to predict in mode I or mixed-mode loading [16–18].

Fibre bridging is of interest in engineered composite materials [14,19] as the additional extrinsic toughening, which may be fully realised under impact loading and subsequent delamination, could be the deciding factor between a destructive brittle failure and a controlled ductile failure. Fibre bridging has been characterised in composites such as CFRP [20], Glass Fibre Reinforced Polymers (GFRP) [21] and other fibre-rich epoxies [22]. Fibre bridging also occurs in a range of biological & natural materials such as fibrous biological or natural materials (e.g., Liver tissue [23], adipose tissue [24], frozen arteries [25] and the cornea [15]) and timbers [26,27].

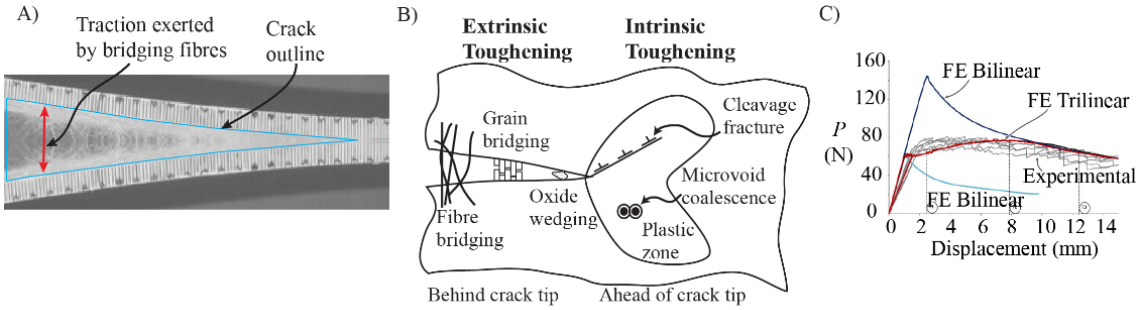

Figure 3-1 A) Example of fibre bridging in GFRP [21] B) Examples of extrinsic and intrinsic toughening mechanisms. Image adapted from Liu et al. [28]. C) Experimental load-displacement behaviour replicated computationally [29].

3.1.2 Experimental fracture tests with fibre bridging

The effect of fibre bridging is observed experimentally via the monotonic increase in fracture toughness or energy release rate with increasing crack length, shown in Figure 3-2C. As an inter-laminate crack propagates in a DCB, the bridging fibres exert tractions on the delaminating surfaces, arresting the crack propagation. The initial value in the crack growth resistance (or R-curves), is set by the energy required for crack initiation. The energy required

to advance the crack front increases as the amount of fibre bridging increases. The fracture toughness plateaus once new fibres bridging the interface compensate fibre breakage or fibre pull out at the other end of the crack and a steady-state turnover of fibres occurs.

Double cantilever beam (DCB) fracture tests of continuous fibre composites often exhibit fibre bridging [19]. Typically, DCB experiments measure load, load-line displacement, and crack propagation and are used to produce fracture resistance curves for a given material. DCB tests are most commonly performed in accordance with ASTM standards [30]. Four methods of data analysis are outlined in the standards: beam theory, modified beam theory, the compliance calibration method, and the modified compliance calibration method. The compliance calibration method is used in the present work and also, for example, Davidson and Waas [31]. Compact tension shear type specimens are also used to investigate interlaminar fracture [32]; however, generating a specimen of sufficient height involves a large number of laminates or compound specimens where the fibre composite is bonded to other materials. Other geometries, such as three point bend tests can also test the interlaminar properties, although this also requires more complicated specimen fabrication [33]. In the current study, we focus on the DCB test specimen which consists of only the fibre composite.

Fibre bridging is observed experimentally via the monotonic increase in fracture toughness or energy release rate with increasing crack length, the so-called resistance curve (or R-curve), shown in Figure 3-2C. Fibre bridging depends on the composite's constituent materials and specimen geometry [21,29,34]. On initiation, the fracture toughness is exclusively determined by the intrinsic mechanisms. However, as the crack front advances, fibre bridging develops in its wake, and the observed fracture toughness increases monotonically as the contribution from bridging increases. The fracture toughness plateaus, reaching a steady state once a steady distribution of bridged fibres is created behind the crack tip. The key features of an R-curve are: the initial value of fracture toughness $\widehat{G}_0$, the plateaued value of

fracture toughness $\hat{G}_{ss}$, the initial crack length a_0, and the length of the new crack surface created while achieving a steady state fracture toughness measurement Δa_{ss} as illustrated in Figure 3-2. Heidari-Rarani, et al. model unidirectional DCB specimens under large-scale fibre bridging and experimental results show that the rise in the R-curve (from $\hat{G}_0$ to $\hat{G}_{ss}$) corresponds with the length of the process zone (which is defined by Heidari-Rarani, et al. in their work as the distance between (i) the point where bridging and the fracture process initiate and (ii) the first point in the wake of damage zone that is unable to sustain cohesive tractions) [22].

3.1.3 Data analysis

Using the compliance calibration method (as described in the ASTM standard), the fracture toughness $\hat{G}$ is determined from the applied load P, the load-line displacement u and the current crack length a:

$$\hat{G} = \mathrm{n}\frac{\mathrm{Pu}}{2\mathrm{ba}} \qquad 3.1$$

where b is the specimen thickness, and n is a linear regression fitting parameter relating the compliance ($C = u/P$) to the crack length [30]. This regression parameter accounts for beam rotations at the crack tip. In DCB tests, measured load-displacement response and R-curves are dependent on the choice of certain material and specimen parameters, such as laminate thickness, modulus, and pre-crack length. Shokrieh et al. investigated the effect of initial crack length on unidirectional glass/epoxy DCB specimens [34]. While the values of $\hat{G}$ do not vary with specimen, the crack length for each value does. It was found experimentally that the initial crack length a_0 only slightly affects the shape of the response. Gutkin, et al. also conducted a coupled experimental and computational study showing that an R-curve is dependent on thickness of the lever arm [29].

3.1.4 Determining cohesive properties

Experimental research on fibre bridging is often coupled with a model of the experimental procedure. In computational models of fibre bridging, it is

necessary to formulate the appropriate traction-separation law (TSL), which is also referred to as a cohesive zone model (CZM). The TSL describes the traction exerted between two debonding surfaces at each point on the crack face based on the local separation between the surfaces. The integral of the function is the work done to fracture. Many studies consider the bridged fibres in this manner, i.e., not as discrete fibres in the model geometry; however, there has not been an in-depth systematic exploration of the influence of TSL parameters.

The shape of the TSL (typical examples are shown in Figure 3-2) is critical in determining and the load-displacement response and the R-curve that will be produced by the simulation. There are several TSL shapes explored in the literature including trapezoidal [35], bilinear [14], trilinear [17] and a continuous function [34,36]. It has been found that a bilinear TSL (Figure 3-2A) is only able to capture the initial stages of fibre bridging [19,29,31] as shown in blue in Figure 3-1B; whereas a trilinear law (Figure 3-2B) is capable of capturing high levels of separation typically found with fibre bridging [19,34,37] as shown in red in Figure 3-1B. Intrinsic toughening mechanisms are collectively captured in the cohesive fracture zone of the TSL (as shown in Figure 3-2), which acts over short separations.

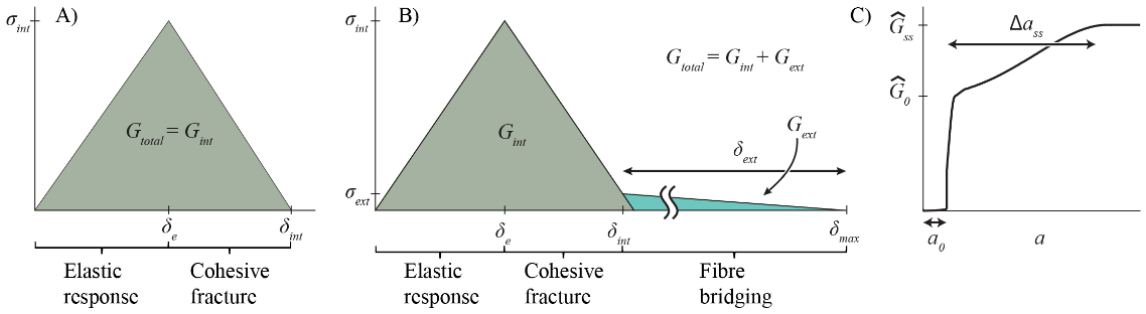

Figure 3-2 General shape of a traction-separation law. A) Bilinear curve without fibre bridging present. B) Trilinear curve with fibre bridging present. In the case of fibre bridging $\delta_{ext} \gg \delta_{e,}\delta_{int}$ and diagram is not to scale C) Idealised experimental observation of crack growth resistance showing key quantities.

Figure 3-2 shows the general form of the traction-separation laws and establishes the terminology used in the current work (for use with the finite element method). For clarity, all fracture energies pertaining to the traction-

separation laws are denoted by G with various subscripts and all measured/observed (either experimentally or in the simulations) quantities are denoted by a circumflex, i.e., $\hat{G}$. The fracture energy, G_{total}, is the total area under the TSL. This fracture energy can be split into intrinsic and extrinsic contributions, related to the respective toughening mechanisms, and can also be determined as the areas of the respective regions:

$$G_{int} \cong \frac{1}{2}\sigma_{int}\delta_{int} \qquad 3.2$$

$$G_{ext} \cong \frac{1}{2}\sigma_{ext}\delta_{ext} \qquad 3.3$$

where all symbols are defined in Figure 3-2. Note that there is a small area overlap in equations 3.2 and 3.3, as $G_{tot} \neq G_{int} + G_{ext}$. The size of the area which is included in both the definition of G_{int} and G_{ext} is equivalent to $\frac{\sigma_{ext}}{\sigma_{int}}(\delta_{int} - \delta_e)$. This value typically accounts for less than 1% of the total fracture toughness in the analyses considered.

While numerous studies have coupled experimental and computational work [19,31,34,38], there is no simple procedure to select cohesive parameters for a finite element model based on experimental observations. In many studies, the J-integral method [39] is used to determine a TSL for laminates as part of a theoretical analysis [40,41] or numerical study [22]. The J-integral method has also been used in ceramic composites [42] and for coatings [43]. In most applications of the J-integral approach, the stresses on the crack surface are assumed to be zero and this is not true in the case of fibre bridging. In a series of works, Sørensen and colleagues [40,44] apply the J integral method to fibre bridging to determine the cohesive law; but the loading of the specimen is via end moments [45].

Previous studies of crack growth in fibre composites have found that computational results can replicate the results in an experimental procedure with fibre bridging present [19,21,29,31,37,46]. However, the effect of the input parameters on the fit between numerical and experimental results has

not been explored and documented; the dominant parameters governing the observed phenomena are not described. Although for example, Heidari-Rarani et al details their justification for a maximum traction σ_{int} for different cases [22], no algorithm to fully define a TSL based on experimental observations is available. Dávila et al. [47] present an approach to determine fracture properties for a tri-linear TSL for a CT fracture specimen. Their approach superimposes two cohesive elements, each with linear softening and the same separation for the maximum traction. In this way, two triangular areas are superimposed, and the intrinsic and extrinsic toughness can be related to these areas and the ratios of the peak strengths and total energy for each element. However, this approach requires non-standard implementation in a finite element package, and they do not fully explore the sensitivity of the overall response to each of the input parameters. The present work provides an insight into selecting cohesive parameters for a TSL with extrinsic toughening based on experimental observations, via a systematic exploration of the TSL parameter space. Key relationships are presented and an approach to reconstruct a TSL based on a small set of experimentally observed variables is described. Several case studies are used to demonstrate the approach.

3.2 Modelling approach

3.2.1 Finite element model

Finite element models of a typical DCB fracture toughness test geometry, in line with ASTM standards, [30] are created in Abaqus (Dassault Systèmes, Rhode Island, USA) using 2D plane strain elements (Abaqus element code: CPE4) to represent the beams and the interfacial behaviour is captured using cohesive elements (shown in Figure 3-3). The mesh used is highly structured, consisting of square elements and the element size is determined by the height of a laminate arm; such that 25 elements are present along the vertical dimension of the laminate arm. A TSL is used to define behaviour of the cohesive layer. The response of the cohesive element (Abaqus element code: COH2D4) follows the default behaviour, whereby the strain is

equivalent to the displacement as a unit thickness is used in the material calculation. The nodes in the cohesive layer are adjusted so that the layer has geometrically zero thickness in the *y*-direction [48]. If the cohesive layer has a finite geometric height, the stiffness applied to the layer (via the TSL) would artificially stiffen the model.

The features of the ASTM standard DCB test are captured in the finite element model: the loading blocks are represented by using the *Coupling Constraint* method and displacements are applied to the associated reference points (with resulting reaction forces). For simplicity, and in line with previous studies of crack growth in CFRP [19], the laminate properties used in this model are linear elastic with Young's modulus of 170 GPa and Poisson ratio of 0.3 unless otherwise stated. As the transverse behaviour is not relevant to the investigations (as only axial stretching is considered for simplicity), the laminates are modelled as isotropic; however, the methodology can be applied to anisotropic laminates. The isotropic nature of these models allows the results to be applied to other materials with in-plane isotropic properties.

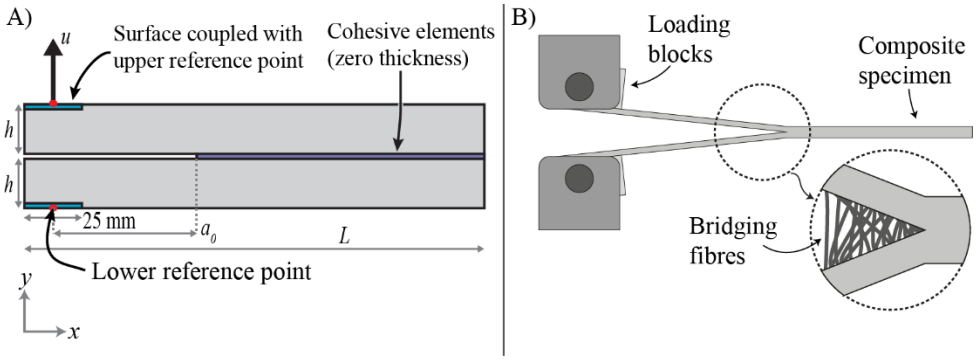

Figure 3-3 A) FE model geometry, based on B) a typical composite test specimen with loading blocks in compliance with ASTM standards [30].

The load-displacement response is measured at the upper reference point, Figure 3-3A. The fracture toughness is calculated by the compliance calibration method [30]. Definition of the crack tip can be difficult and somewhat arbitrary when fibre bridging is present. The crack tip can be defined by observation or using the beam compliance. Difficulty arises in experimental observations due to extrinsic toughening mechanisms

obstructing the view of the crack tip. In this study, the crack length is defined as the distance from the pre-crack to where the separation of the surfaces is equal to δ_e (as defined in Figure 3-2). As this study is computational, a separation of δ_e can be measured in postprocessing to identify the crack tip; in practice measuring this separation (of δ_e) is not simple. The crack length measurement is used in equation 3.1 to produce the R-curve.

A TSL is shown in Figure 3-2 where the traction in a cohesive element σ is defined in terms of the local separation δ. The shape of the curve is defined by an initial cohesive stiffness k_c, a maximum traction σ_{int} , and subsequent pairs of σ and δ which define the traction-separation response. In the current study, only mode I cracks are considered, and any tangential displacements are not considered.

The simulation is solved using a non-linear implicit scheme in Abaqus/Standard. The lower reference point is fixed in all translational degrees of freedom while being free to rotate, and the upper block is displaced vertically upwards. The displacement of this point u, the resulting reaction force P, and the crack length a are recorded and used to calculate the measured fracture energy $\hat{G}$ using the same compliance calibration method as used in the ASTM experimental methods (equation 3.1).

3.2.2 Parameter variation details

A systematic variation of the parameters associated with the TSL (governing the material behaviour of the interface) is conducted, along with specimen specific parameter variation. To represent intrinsic toughness only, it is sufficient to describe a TSL using k_c, σ_{int}, and δ_{int} (note $\delta_e = \sigma_{int}/k_c$ is not independent). Extrinsic toughening (bridging behaviour) is considered by using a TSL which includes tractions which act over larger separations; in the case of the tri-linear law, as shown in Figure 3-2B, two extra parameters δ_{ext} and σ_{ext} are required.

For intrinsic toughness only, a wide range of TSL parameters are considered and the details and results are shown in Appendix 1. In terms of the shape

of the TSL, the energy, i.e., the area under the curve, dictates the observed response as long as δ_{int} is small. If δ_{int} is too large, then the peak in the load-displacement response becomes less distinct and would not capture typical experimentally observed behaviour. The elastic loading slope and the softening/unloading slope will affect the computational cost, but uncertainty in the experimental data would frustrate any attempt at calibrating these values. For computational efficiency, setting $\delta_e = \delta_{int}/2$ is recommended; estimation of σ_{int} is discussed below in Section 3.4. Note that numerical noise is observable in the load-displacement response for $L_{el}/\delta_{int} \geq 50$ (data not shown).

For materials with both intrinsic and extrinsic toughness, the parameter space is explored systematically in four phases I-IV (with the details in Table 3-1,Table 3-2 and Table 3-3). The intrinsic toughness is not varied in these phases; the parameters relating to the intrinsic part of the TSL are fixed, unless otherwise noted; previous simulations of experimental data are used to determine appropriate ranges for parameters [19].

The four phases are:

I. The intrinsic properties $(\sigma_{int}, \delta_e, \delta_{int})$ are held constant and the extrinsic toughness G_{ext} is varied by increasing the bridging length δ_{ext}. The values of these parameters are based on CFRP as presented by De Morais [19].

II. The total fracture energy G_{total} is held constant but the ratio of G_{int}: G_{ext} is varied. This means that the elastic region (σ_{int}, δ_e) is constant but the cohesive fracture zone $(\delta_{int},\ \sigma_{ext})$ is allowed to move to ensure the total energy G_{total} remains constant across analyses.

III. The R-curve specimen dependence is examined by varying dimensions and modulus with fixed TSL parameters ($\delta_e = 0.005$ mm, $\delta_{int} = 0.01$ mm, δ_{ext} = 1 mm, σ_{int} = 40 MPa, σ_{ext} = 0.4 MPa,

$G_{int} = 200\,J/m^2$ & $G_{ext} = 200\,J/m^2$). Details are found in Table 3-2.

IV. The shape of the extrinsic region is varied by adjusting the extrinsic parameters (δ_{ext} and σ_{ext}) for constant extrinsic toughness. As the bridging length δ_{ext} increases, the bridging stress σ_{ext} decreases so that the extrinsic toughness stays constant. This is repeated for four values of G_{ext} as shown in Table 3-3.

Table 3-1 Details of parameter variation I & II (examining the ratio of intrinsic to extrinsic toughness). This study has been completed for $\sigma_{ext} = 0.1, 0.4, 1.0$ & 4.0 MPa. All results show the same trend regardless of σ_{ext}.

Phase	$\boldsymbol{\sigma_{int}}$ (MPa	$\boldsymbol{\sigma_{ext}}$ (MPa	$\boldsymbol{\delta_e}$ (μm)	$\boldsymbol{\delta_{int}}$ (μm)	$\boldsymbol{\delta_{ext}}$ (mm)	$\boldsymbol{G_{int}}$ ($\mathbf{J/m^2}$)	$\boldsymbol{G_{ext}}$ ($\mathbf{J/m^2}$)	$\boldsymbol{G_{total}}$ ($\mathbf{J/m^2}$)
I	40	0.4	5	15	0.05	300	10	310
	40	0.4	5	15	0.1	300	20	320
	40	0.4	5	15	0.3	300	60	360
	40	0.4	5	15	0.5	300	100	400
	40	0.4	5	15	1.0	300	200	500
II	40	0.4	5	19.5	0.05	390	10	400
	40	0.4	5	19	0.1	380	20	400
	40	0.4	5	17	0.3	340	60	400
	40	0.4	5	15	0.5	300	100	400
	40	0.4	5	10	1.0	200	200	400

Table 3-2 Summary of parameter variation III, examining R-curve specimen dependence, full list of parameter combinations is in the supplementary material.

Phase	Parameter	Values
III	$\boldsymbol{L}$ (mm)	150, 300, 400, 600, 1000
	$\boldsymbol{a_0}$ (mm)	0, 10, 25, 50, 60, 70, 100
	$\boldsymbol{E}$ (GPa)	50, 170, 300, 600, 1000, 1700
	$\boldsymbol{h}$ (mm)	2, 3, 4, 5, 6, 7, 8, 12, 16

Table 3-3 Values of σ_{ext} (MPa) for the shape variation of the extrinsic toughening region (phase IV). Intrinsic toughening properties are fixed. $\delta_e = 0.005$ mm, $\delta_{int} = 0.01$ mm, $\sigma_{int} = 40$ MPa, $G_{int} = 200$ J/m^2.

		$\boldsymbol{\delta_{ext}(mm)}$	0.05	0.1	0.25	0.5	1	2.5	10
IV	$\boldsymbol{\sigma_{ext}}$ **(MPa)**	$\boldsymbol{G_{ext} = 200\ J/m^2}$	8	4	1.5	0.8	0.4	0.16	0.04
		$\boldsymbol{G_{ext} = 400\ J/m^2}$	16	8	3.2	1.6	0.8	0.32	0.08
		$\boldsymbol{G_{ext} = 1000\ J/m^2}$	N/A	20	8	4	2	0.8	0.2
		$\boldsymbol{G_{ext} = 2000\ J/m^2}$	N/A	N/A	16	8	4	1.6	0.4

3.3 Results

Figure 3-4 shows the deformed configuration of a DCB simulation with an intrinsic toughness of 300 J/m^2 and an extrinsic toughness of 200 J/m^2 (with properties as shown in the final row of Table 3-1 phase I and in Figure 3-4B). The cohesive tractions, shown as arrows in Figure 3-4A in the steady-state (i.e., once the measured toughness has reached a plateau), are at a maximum at the crack tip (defined here as $\delta = \delta_e$) and decrease monotonically in the bridging zone behind the crack tip. The load vs load-line displacement (Figure 3-4C) shows a peak at which time crack propagation commences followed by a reduction in force as the crack grows as a result of the reduction in compliance of the DCB arms. The substantial amount of extrinsic fracture energy results in a rising R curve behaviour (Figure 3-4D); the initial value of the measured fracture energy is a direct result of the intrinsic toughness, and a final/plateaued value is determined by the total fracture energy (i.e., intrinsic plus extrinsic). The crack growth which occurs before the plateau is reached (and a steady-state toughness is obtained) is hereafter referred to as Δa_{ss}.

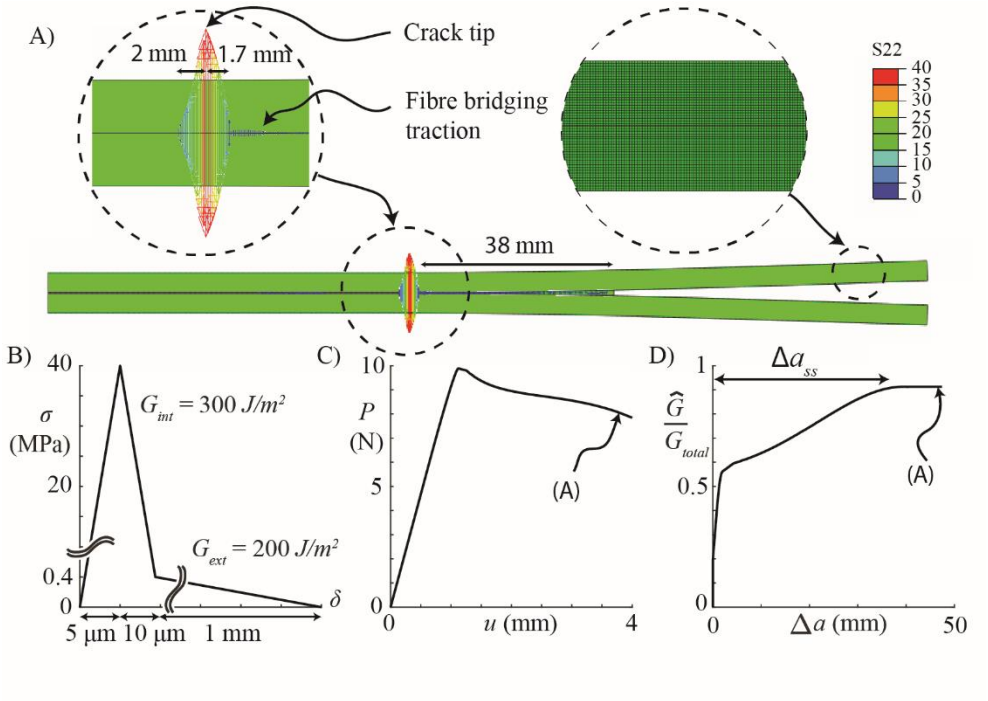

Figure 3-4 A) Deformed shape of DCB specimen with overlaid traction vectors. The dimensions of 2 mm, 1.7 mm and 38 mm show the differing crack length scales over which intrinsic and extrinsic toughening mechanisms act. Applied traction-separation law shown (B) with the measured load-displacement response (C) and resulting R-curve, normalised with input fracture energy G_{total} (D).

3.3.1 The ratio of extrinsic to intrinsic toughness ($\boldsymbol{G_{ext}}$: $\boldsymbol{G_{int}}$)

The effect of the ratio of intrinsic toughness to extrinsic toughness on the overall R-curve behaviour is summarised in Figure 3-5 based on the parameters listed above (I & II in Table 3-1). In the first set of results (Figure 3-5A-D), the intrinsic toughness is fixed and the extrinsic varied and, in the second (Figure 3-5E-H), the total toughness is fixed and the ratio of intrinsic to extrinsic toughening is varied. In the case of the former (A-D), the following observations are made: (i) the peak load is constant, (ii) the crack growth length to reach the steady-state measured toughness Δa_{ss} increases with increasing G_{ext}, (iii) the plateau/steady-state measured toughness increases with G_{total}, and (iv), when normalized by the total toughness, the steady-state measured toughness ≈ 1, as expected.

In second set of results (E-H), and similar to the above, we note: (i) the peak load increases with increasing G_{int}, (ii) Δa_{ss} increases with increasing G_{ext}, and (iii) the plateau/steady-state measured toughness is constant with

constant G_{total}. In these simulations, the extrinsic energy is increased by increasing δ_{ext} and correspondingly, δ_{int} is reduced to keep the total energy constant.

These results show that the R-curve behaviour is dominated by changes in the extrinsic toughness, as expected; however, in these simulations only δ_{ext} is varied. A further investigation of the other extrinsic parameters is shown below.

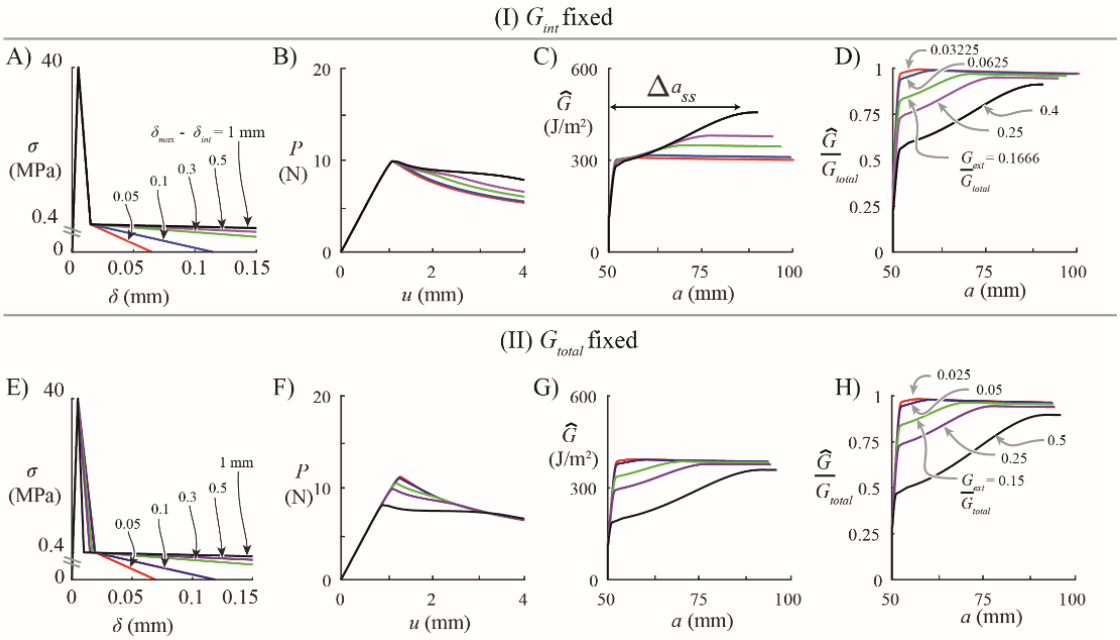

Figure 3-5 Summarised input parameters and results from phase I (where G_{int} is fixed and G_{ext} is varied) and II (where G_{tot} is fixed and the ratio of G_{int}: G_{ext} is varied) of the parameter variation, examining the ratio of intrinsic to extrinsic toughness.

3.3.2 Effect of fracture test properties

In the current section, the effect of test specimen parameters (h, E, a_0) on the response are explored (the series of simulations III in Table 3-2). Figure 3-6 shows that increasing h (Figure 3-6A) or increasing E (Figure 3-6D) causes an increase in Δa_{ss}. For a valid beam test (i.e., $\frac{a_0}{h} > 10$), Δa_{ss} is linearly proportional to h for all values of E considered (Figure 3-6B, C), as evident from the 1:1 relationship on a log-log scale indicating a linear relationship. Similarly, Δa_{ss} is linearly proportional to $\sqrt[3]{E}$ for all values of h considered (Figure 3-6E, F), as evident from the 1:3 relationship on a log-log

scale. The original crack length a_0 does not affect the behaviour for slender beams (data not shown).

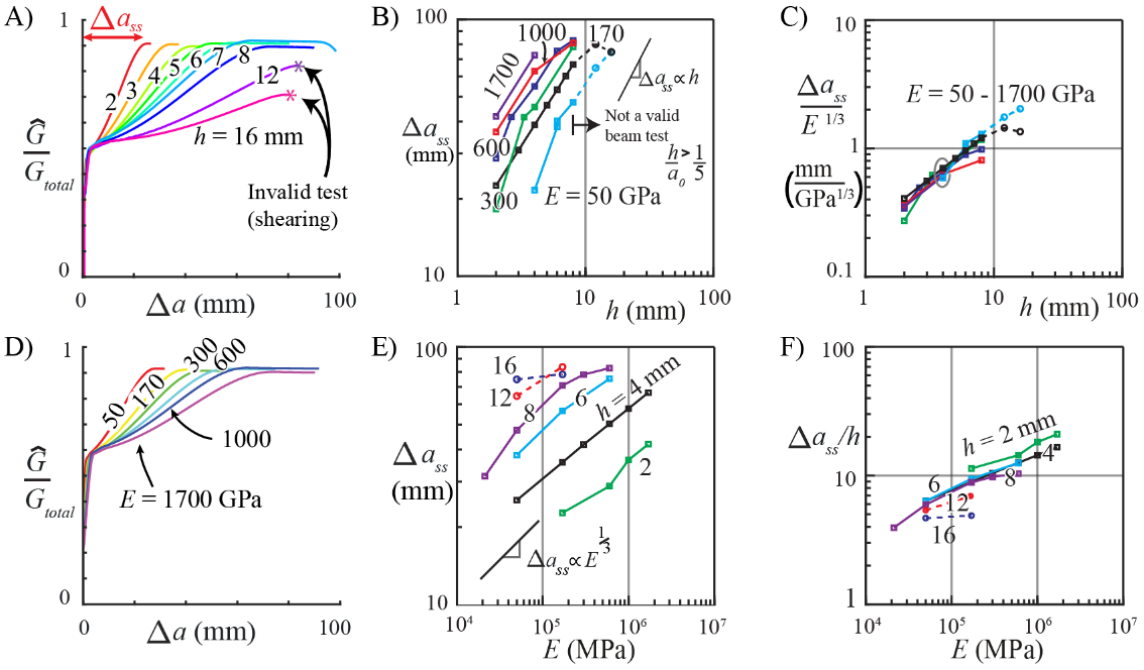

Figure 3-6 Top row: Relationship between steady-state crack growth Δa_{ss} and beam thickness h for $E = 170$ GPa A) R-curves. (B&C) A linear relationship (note 1:1 relationship is also shown) between Δa_{ss} and h for various laminate moduli. Bottom row: Relationship between steady-state crack growth Δa_{ss} and beam modulus E for $h = 4$ mm. D) R-curves. (E&F) showing relationship between Δa_{ss} and E for various laminate thicknesses.

3.3.3 Bridging length and steady-state crack length

Previously, G_{ext} was shown to control the shape of the R-curve by varying δ_{ext}; here we show the G_{ext} does not substantially change the ratio $\Delta a_{ss}/\delta_{ext}$. Therefore, the bridging length is the most important parameter – bridging tractions will influence the overall toughness, but not the slope of an R-curve ($\hat{G}/G_{total}$ vs Δa). A range of behaviours are considered ; within each group of simulations δ_{ext} is varied such that $G_{ext} = 0.5\,\sigma_{ext}\delta_{ext}$ is constant (Figure 3-7A); this is repeated for 4 different values of G_{ext} in total (Table 3-3). For all values of G_{ext}, Δa_{ss} is shown to linearly increase with δ_{ext}. In all cases, $G_{int} = 200\ \mathrm{J/m^2}$

We note in passing that the input fracture energies in the cohesive law (i.e., the total, G_{total}) are not completely recovered in the measured values $\hat{G}$, i.e., $\hat{G}/G_{total} < 1$. This error arises from the ASTM data reduction methods which are replicated here *in silico.* The data reduction methods consider the

bending of the arms of the DCB specimen and beam rotations at the crack tip are accounted for; however, this method does not account for the tractions behind the crack as a result of fibre bridging. A follow-up study will examine this effect in detail in the context of the data reduction methods as described in the ASTM standard [30] and their appropriateness in the presence of fibre bridging or other extrinsic mechanisms.

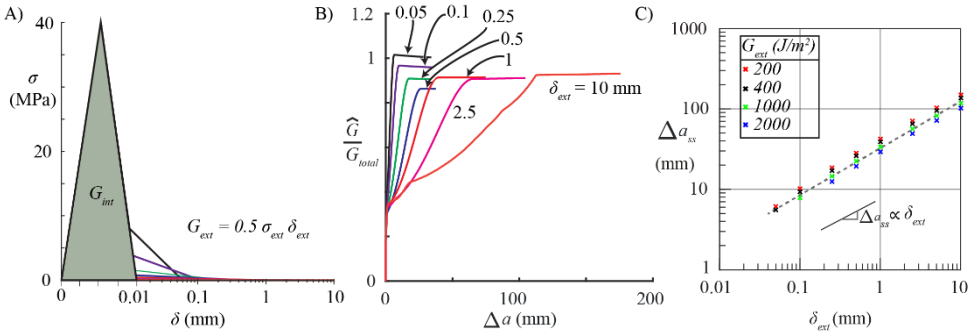

Figure 3-7 A) Traction-separation laws with constant G_{ext}. Note: the extrinsic part of the horizontal axis is shown on a log scale. B) R-curves showing effect of δ_{ext} for the case with $G_{ext} = 400\ J/m^2$ and C) the relationship between the bridging length δ_{ext} and steady-state crack length Δa_{ss}.

3.3.4 Reproduction of experimentally observed behaviour

Based on the above results, a strategy for determining traction-separation properties (suitable for use in simulation) from experimental data is suggested (Table 3-4). The previously established relationships above ($\Delta a_{ss} \propto E^{1/3}$ and $\Delta a_{ss} \propto h$) are combined with the relationship established in Figure 3-7C ($\Delta a_{ss} \propto \delta_{ext}$) to relate Δa_{ss} to E, h & δ_{ext} as shown in Figure 3-8B.

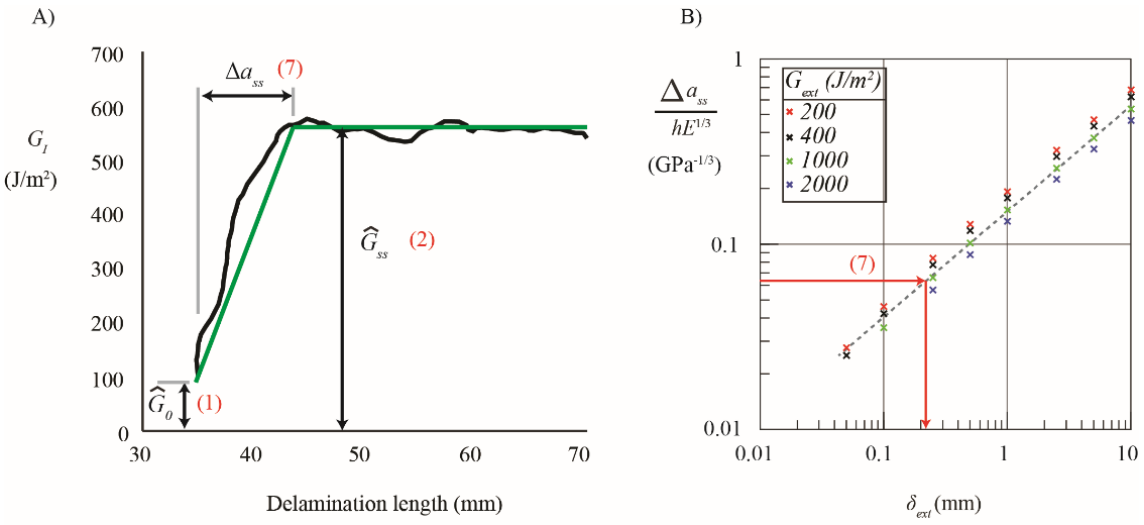

Figure 3-8 A) Measurement of G_{int}, G_{ext} and Δa_{ss} from bilinear approximation of an R-curve [22]. B) Previously established relationship between Δa_{ss} and E, h & δ_{ext}; used to calculate δ_{ext}.

Table 3-4 Origin of traction-separation law parameters

	Parameter	Source	Notes
1	G_{int}	Directly measure from R-curve ($G_{int} = \hat{G}_0$).	
2	G_{ext}	Plateau value on fracture resistance curve ($G_{ext} = \hat{G}_{ss} - \hat{G}_0$).	Small errors are noticed for large extrinsic toughness. ASTM data reduction methods do not properly account for the large tractions behind the crack tip when accounting for rotation of the beams at the crack tip.
3	σ_{int}	σ_{int} can be approximated by the ply transverse tensile strength [19,49,50].	Note: that once G_{int} is determined σ_{int} and δ_{int} are inversely proportional. Setting σ_{int} too low will lead to a less pronounced peak on a plot of P, u in disagreement with experimental observations. See below regarding δ_{int}
4	δ_{int}	σ_{int} and G_{int} constrain the choice of δ_{int} (equation 3.2).	Too small a value of δ_{int} would require an excessively fine mesh to avoid numerical issues (if $L_{el}/\delta_{int} \geq 50$)

5	δ_e	It is recommended to use a symmetric intrinsic region, $\delta_e = \delta_{int}/2$	An asymmetric load vs unload slope will lead to increased computation cost related to the ratio of L_{el} to $\min(\delta_e, \delta_{int} - \delta_e)$
6	k_c	k_c is not independent. $k_c = \sigma_{int}/\delta_e$	
7	δ_{ext}	Determined from Figure 3-8 using the steady state crack length Δa_{ss} (measured from R-curve).	
8	σ_{ext}	G_{ext} and δ_{ext} constrain the choice of σ_{ext} (equation 3.3).	

3.3.5 Case studies

The method outlined above is applied to three test case studies using existing data [22,34,38]. Figure 3-9 below shows the experimental data from these studies (black), the bilinear approximations used as model inputs (green) and resulting simulations (red). The TSL used in these simulations is obtained from the bilinear approximation.

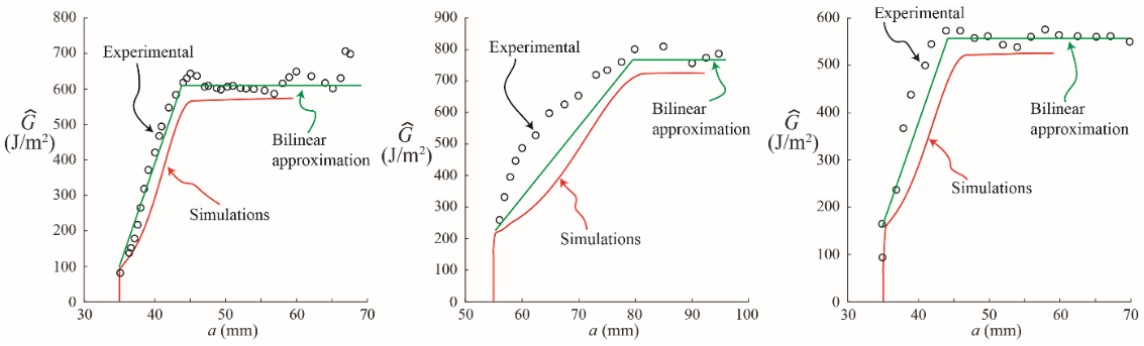

Figure 3-9 Case studies comparing experimental data (black) with simulated R-curves (red) using a traction-separation law approximated based on the method described in this study, bilinear approximation shown in green. Left: Shokrieh et al. [34], Middle: De Morais & Pereira [38], Right: Heidari-Rarani et al [22].

The materials used in these case studies encompass a range of material parameters; their properties and resulting traction-separation laws are summarised in Table 3-5. In all cases, the key features are captured, namely

the initial and plateau values of observed tractions, and the crack growth required to get the plateau. The form of the TSL assumed in this work does result in a difference between the slope of the R-curve during the transition region, particularly for the case of the experimental observations of De Morais and Pereira. Capturing the exact shape would require an arbitrarily shaped TSL and is beyond the scope or intent of the present work. Similar to the observations made above regarding the influence of fibre bridging on the ASTM data reduction methods, the plateau value of the measured toughness is below that of the bi-linear approximation (which informed the model inputs).

Table 3-5 Summary of parameters and resulting traction-separation law used in case studies.

Parameter	*Shokrieh et al.*	*De Morais & Pereira*	*Heidari-Rarani et al.*
L (mm)	150	200	150
a_0 (mm)	35	55	35
E (GPa)	29.5	119	30.54
h (mm)	2	1.8	2.1
G_{int} (J/m^2)	100	250	175
G_{ext} (J/m^2)	500	550	375
Δa_{ss} (mm)	8.5	25	8.6
δ_e (mm)	0.0025	0.005	0.005
δ_{int} (mm)	0.005	0.01	0.01
σ_{int} (MPa)	40	50	35
δ_{ext} (mm)	0.65	2.3	0.65
σ_{ext} (MPa)	1.538	0.478	1.154

3.4 Concluding remarks

By providing an in-depth exploration of the parameter space associated with a traction-separation law (TSL), the shape of a fracture resistance curve (R-curve) can be explained in detail. For extrinsic toughening mechanisms such as fibre bridging, the maximum separation at which the bridging tractions act was found to be the key cohesive property to be tuned to capture the

main features of an R-curve (i.e., the initial and steady state toughness values and the crack growth required to reach the steady state value). For cohesive behaviour with only intrinsic toughening mechanisms, the cohesive stiffness and maximum traction do not control the behaviour – it is the intrinsic fracture toughness which dictates the behaviour. However, as bridging tractions are substantially less than the maximum intrinsic traction, a trilinear TSL is required to capture bridging behaviour. These observations are used to establish a procedure to robustly identify the input parameters for use in a computational model (i.e., with a traction-separation law)

For cohesive behaviour with extrinsic toughening mechanisms such as fibre bridging, the relationship between the key features of an observed crack growth resistance curve and the input TSL have been robustly explored and key trends are identified. Examination of these trends has shown that the key features on an R-curve (the initial value, the plateau in toughness and the steady-state crack length) can be explained in terms of the interfacial law. The initial value $\hat{G}_0$ required for crack initiation is the intrinsic fracture toughness G_{int}, the plateaued value $\hat{G}_{ss}$ is the total fracture energy G_{total} in the model. The steady-state crack length Δa_{ss}, required to achieve a plateau in the R-curve, is a function of beam thickness, modulus and fibre bridging length δ_{ext} (a cohesive property).

Reproduction of experimental results has shown that this method of determining a TSL is accurate. These results facilitate improved understanding of crack growth resistance through quick interpretation of experimental data. By replicating the experimental procedures in the processing of the simulations (rather than for example numerical calculating the J-integral), our results are directly relevant to the experimental testing and calibration of models. The input parameters for finite element simulations can be quickly determined and employed in analyses of end-use scenarios and applications, e.g., in composite structures such as wing surfaces or turbine blades. Correctly capturing the effect of such toughening

mechanisms is critical for prediction of failure via inter-laminate cracking in large scale composite structures.

3.5 References

[1] Argon AS, Cohen RE. Toughenability of polymers. Polymer (Guildf) 2003;44:6013–32. https://doi.org/10.1016/S0032-3861(03)00546-9.

[2] Cepeda-Jiménez CM, Pozuelo M, García-Infanta JM, Ruano OA, Carreño F. Influence of the alumina thickness at the interfaces on the fracture mechanisms of aluminium multilayer composites. Mater Sci Eng A 2008;496:133–42. https://doi.org/10.1016/j.msea.2008.05.015.

[3] Liu L, Jia C, He J, Zhao F, Fan D, Xing L, et al. Interfacial characterization, control and modification of carbon fiber reinforced polymer composites. Compos Sci Technol 2015;121:56–72. https://doi.org/10.1016/j.compscitech.2015.08.002.

[4] Sills RB, Thouless MD. Cohesive-length scales for damage and toughening mechanisms. Int J Solids Struct 2015. https://doi.org/10.1016/j.ijsolstr.2014.06.010.

[5] Nairn JA, Hu S. Matrix Microcracking. Damage Mech. Compos. Mater., vol. 1, 1994, p. 1–46.

[6] Sorem WA, Dodds Jr. RH, Rolfe ST. Effects of crack depth on elastic-plastic fracture toughness. Int J Fract 1991;47:105–126.

[7] Orowan E. Fracture and strength of solids. Rep Prog Phys 1949;12. https://doi.org/10.1088/0034-4885/77/5/056502.

[8] Kovar D, Thouless MD, Halloran JW. Crack Deflection and Propagation in Layered Silicon Nitride/Boron Nitride Ceramics. J Am Ceram Soc 1998;81:1004–12. https://doi.org/10.1111/j.1151-2916.1998.tb02438.x.

[9] Smith E. Crack bifurcation in brittle solids. J Mech Phys Solids 1968;16:329–36.

[10] Beachem CD, Yoder GR. Elastic-plastic fracture by homogeneous microvoid coalescence tearing along alternating shear planes. Metall Trans 1973;4:1145–53. https://doi.org/10.1007/BF02645619.

[11] Watanabe H, Khera SC, Vargas MA, Qian F. Fracture toughness comparison of six resin composites. Dent Mater 2008;24:418–25. https://doi.org/10.1016/j.dental.2007.06.018.

[12] Compston P, Jar PYB. Influence of fibre volume fraction on the mode I interlaminar fracture toughness of a glass-fibre/vinyl ester composite. Appl Compos Mater 1999;6:353–68. https://doi.org/10.1023/A:1008973211347.

[13] Cha Y-H, Kim K-S, Kim D-J. Evaluation on the fracture toughness and strength of fiber reinforced brittle matrix composites. KSME Int J 1998;12:370–9. https://doi.org/10.1007/bf02946351.

[14] Meo M, Thieulot E. Delamination modelling in a double cantilever beam. Compos Struct 2005;71:429–34. https://doi.org/10.1016/j.compstruct.2005.09.026.

[15] Tonsomboon K, Koh CT, Oyen ML. Time-dependent fracture toughness of cornea. J Mech Behav Biomed Mater 2014;34:116–23. https://doi.org/10.1016/j.jmbbm.2014.01.015.

[16] Parmigiani JP, Thouless MD. The roles of toughness and cohesive strength on crack deflection at interfaces. J Mech Phys Solids 2006;54:266–87. https://doi.org/10.1016/j.jmps.2005.09.002.

[17] Li S, Thouless MD, Waas AM, Schroeder JA, Zavattieri PD. Use of mode-I cohesive-zone models to describe the fracture of an adhesively-bonded polymer-matrix composite. Compos Sci Technol 2005;65:281–93. https://doi.org/10.1016/j.compscitech.2004.07.009.

[18] Li S, Thouless MD, Waas AM, Schroeder JA, Zavattieri PD. Use of a cohesive-zone model to analyze the fracture of a fiber-reinforced polymer-matrix composite. Compos Sci Technol 2005. https://doi.org/10.1016/j.compscitech.2004.08.004.

[19] De Morais AB. A new fibre bridging based analysis of the Double Cantilever Beam (DCB) test. Compos Part A Appl Sci Manuf 2011;42:1361–8. https://doi.org/10.1016/j.compositesa.2011.05.019.

[20] De Morais AB. Double cantilever beam testing of multidirectional laminates. Compos Part A Appl Sci Manuf 2003;34:1135–42. https://doi.org/10.1016/j.compositesa.2003.08.008.

[21] Manshadi BD, Farmand-Ashtiani E, Botsis J, Vassilopoulos AP. An iterative analytical/experimental study of bridging in delamination of the double cantilever beam specimen. Compos Part A 2014;61:43–50. https://doi.org/10.1016/j.compositesa.2014.02.001.

[22] Heidari-Rarani M, Shokrieh MM, Camanho PP. Finite element modeling of mode I delamination growth in laminated DCB specimens with R-curve effects. Compos Part B Eng 2013;45:897–903. https://doi.org/10.1016/j.compositesb.2012.09.051.

[23] Gokgol C, Basdogan C, Canadinc D. Estimation of fracture toughness of liver tissue: Experiments and validation. Med Eng Phys 2012;34:882–91. https://doi.org/10.1016/j.medengphy.2011.09.030.

[24] Comley K, Fleck NA. A micromechanical model for the Young's modulus of adipose tissue. Int J Solids Struct 2010;47:2982–90. https://doi.org/10.1016/j.ijsolstr.2010.07.001.

[25] Shahmansouri N, Cartier R, Mongrain R. Characterization of the toughness and elastic properties of fresh and cryopreserved arteries. J Biomech 2015;48:2205–9. https://doi.org/10.1016/j.jbiomech.2015.03.033.

[26] Ammann S, Niemz P. FIBRE AND ADHESIVE BRIDGING AT GLUE JOINTS IN EUROPEAN BEECH WOOD. Wood Res 2014;59:303–12.

[27] Vasic S, Smith I. Bridging crack model for fracture of spruce. Eng Fract Mech 2002;69:745–60. https://doi.org/10.1016/S0013-7944(01)00091-1.

[28] Liu B, Huang L, Geng L, Yin F. Multiscale Hierarchical Structure and Laminated Strengthening and Toughening Mechanisms. Lamination - Theory Appl 2018. https://doi.org/10.5772/intechopen.69976.

[29] Gutkin R, Laffan ML, Pinho ST, Robinson P, Curtis PT. Modelling the R-curve effect and its specimen-dependence. Int J Solids Struct 2011;48:1767–77. https://doi.org/10.1016/j.ijsolstr.2011.02.025.

[30] ASTM. Standard Test Method for Mode I Interlaminar Fracture Toughness of Unidirectional Fiber-Reinforced Polymer Matrix Composites 1 2013. https://doi.org/10.1520/D5528-13.

[31] Davidson P, Waas AM. Non-smooth mode I fracture of fibre-reinforced composites: an experimental, numerical and analytical study. Philos Trans R Soc A 2012;370:1942–65. https://doi.org/10.1098/rsta.2011.0381.

[32] Rikards R, Buchholz FG, Wang H, Bledzki AK, Korjakin A, Richard HA. Investigation of mixed mode I/II interlaminar fracture toughness of laminated composites by using a CTS type specimen. Eng Fract Mech 1998;61:325–42. https://doi.org/10.1016/S0013-7944(98)00068-X.

[33] Schiffer A, Tagarielli VL. Predictions of the interlaminar tensile failure of a carbon/epoxy composite laminate. Compos Struct 2015;133:997–1008. https://doi.org/10.1016/j.compstruct.2015.07.070.

[34] Shokrieh MM, Salamat-Talab M, Heidari-Rarani M. Effect of initial crack length on the measured bridging law of unidirectional E-glass/epoxy double cantilever beam specimens. Mater Des 2014;55:605–11. https://doi.org/10.1016/j.matdes.2013.09.064.

[35] Elices M, Guinea G V., Omez JG, Planas J. The cohesive zone model: advantages, limitations and challenges. Eng Fract Mech 2002;69:137–63. https://doi.org/https://doi.org/10.1016/S0013-7944(01)00083-2.

[36] Jacobsen TK, Sørensen BF. Mode I intra-laminar crack growth in composites - modelling of R-curves from measured bridging laws. Compos Part A Appl Sci Manuf 2001;32:1–11. https://doi.org/10.1016/S1359-835X(00)00139-1.

[37] Blackman BRK, Hadavinia H, Kinloch AJ, Paraschi M, Williams JG. The calculation of adhesive fracture energies in mode I: revisiting the tapered double cantilever beam (TDCB) test. Eng Fract Mech 2003;70:233–48. https://doi.org/10.1016/S0013-7944(02)00031-0.

[38] De Morais AB, Pereira AB. Application of the effective crack method to mode I and mode II interlaminar fracture of carbon/epoxy unidirectional laminates. Compos Part A 2007;38:785–94. https://doi.org/10.1016/j.compositesa.2006.09.001.

[39] Rice JR. A Path Independent Integral and the Approximate Analysis of Strain Concentration by Notches and Cracks. J Appl Mech 1968;35:379–86.

[40] Sørensen BF, Jacobsen TK. Determination of cohesive laws by the J integral approach. Eng Fract Mech 2003;70:1841–58. https://doi.org/10.1016/S0013-7944(03)00127-9.

[41] Li V, Ward R. A Novel Testing for Post-peak Tensile Behavior of Cementitious Composites. Fract Toughness Fract Energy 1989.

[42] Brenet P, Conchin F, Fantozzi G, Reynaud P, Rouby D, Tallaron C. Direct measurement of crack-bridging tractions: A new approach to the fracture behaviour of ceramic/ceramic composites. Compos Sci Technol 1996;56:817–23. https://doi.org/https://doi.org/10.1016/0266-3538(96)00026-7.

[43] Zhu Y, Liechti KM, Ravi-Chandar K. Direct extraction of rate-dependent traction–separation laws for polyurea/steel interfaces. Int J Solids Struct 2009;46:31–51. https://doi.org/10.1016/j.ijsolstr.2008.08.019.

[44] Sørensen BF, Jacobsen TK. Large-scale bridging in composites: R-curves and bridging laws. Compos Part A Appl Sci Manuf 1998;29:1443–51. https://doi.org/10.1016/S1359-835X(98)00025-6.

[45] Holmes JW, Liu L, Sørensen BF, Wahlgren S. Experimental approach for mixed-mode fatigue delamination crack growth with large-scale bridging in polymer composites. J Compos Mater 2014;48:3111–28. https://doi.org/10.1177/0021998313507613.

[46] Airoldi A, Dávila CG. Identification of material parameters for modelling delamination in the presence of fibre bridging. Compos Struct 2012;94:3240–9. https://doi.org/10.1016/j.compstruct.2012.05.014.

[47] Dávila CG, Rose CA, Camanho PP. A procedure for superposing linear cohesive laws to represent multiple damage mechanisms in the fracture of composites. Int J Fract 2009;158:211–23. https://doi.org/10.1007/s10704-009-9366-z.

[48] Systemes D. Abaqus user manual 2010:Section 29.5.6.

[49] De Morais AB, De Moura MFSF. Assessment of initiation criteria used in interlaminar fracture tests of composites. Eng Fract Mech 2005;72:2615–27. https://doi.org/10.1016/j.engfracmech.2005.05.003.

[50] Hodgkinson JM. Mechanical Testing of Advanced Fibre Composites. 2000.

[51] Borotto M. Bridging effects on Mixed Mode delamination : experiments and numerical simulation. École Polytechnique Fédérale de Lausanne, 2016. https://doi.org/10.5075/epfl-thesis-7056.

Chapter 4. Double Rolling Arc Fracture Test (DRAFT): Analysis of a Novel Test Method for Directly Measuring Fracture Properties in Composite Beams

Abstract

Fracture toughness in composite beams is typically calculated by approximate methods (e.g., the compliance calibration method). Composite specimens undergoing fracture often exhibit toughening behaviour during crack propagation. Traditional methods such as compact tension and three-point or four-point bend tests do not accurately capture the extrinsic toughening mechanisms, as the mechanism may not fully develop during the test. Here, a novel fracture test method is replicated using the finite element method. This test applies an end moment to a composite beam specimen; while the test apparatus dictates the curvature achieved by the specimen and the specimen's strain energy. The crack propagation rate is controlled in this method. Due to the loading nature of the test fixture, the fracture toughness can be read as a function of the measured load. As the specimen holds a constant curvature, the separation between laminates can be calculated as a function of applied displacement and geometric features. The fracture toughness and interlaminar separation can be manipulated to yield an expression for the interface traction. These expressions are applied to experimental measurements to produce an interface law. This interface law is then used in finite element software to reproduce the original experimental data with a high level of fidelity. The method defined here does not accurately capture intrinsic behaviour but captures the evolution of the R-curve behaviour well. It is recommended to use a traditional DCB test for intrinsic properties and the novel DRAFT method for extrinsic properties. The shape of the interface law is important as; even if the full fracture toughness is not realised – the shape of the law influences the

transitional response as the complete interface law is being realised. The material tested exhibits a second peak in the traction-separation response. This indicates that the material gets somewhat tougher as separation increases. The Double Cantilever Beam (DCB) test is limited when handling materials that experience high levels of extrinsic toughening. This method supplements the DCB method's limitations by handling large scale extrinsic mechanisms well; albeit without accurately capturing the intrinsic response.

Nomenclature

a	Crack length
a_0	Pre-crack tab length
a_i	Crack length at a crosshead displacement of u_i
a_j	Crack length at a crosshead displacement of u_j
b	Specimen width
D	Damage variable
E	Young's modulus
G	Measured fracture energy
G_{ext}	Extrinsic fracture energy
G_i	Fracture energy achieved at a crosshead displacement u_i
G_{int}	Intrinsic fracture energy
G_j	Fracture energy achieved at a crosshead displacement u_j
G_{tot}	Total fracture energy
h	Specimen half thickness
I	Moment of Inertia

L	Specimen length
M	Moment
P	Measured load
P_d	Reaction force due to energy dissipation
P_e	Load required to elastically deform the specimen
P_i	Measured load at a crosshead displacement u_i
P_j	Measured load at a crosshead displacement u_j
P_{max}	Maximum value achieved reaction force, associated with dissipated energy realisation
P_1	Reaction force between lower and upper plateaus. Denotes transition from intrinsic to extrinsic toughening
P_r	Load measured at one rolling arc. Note that $P = 2P_r$
r	Rolling arc radius
R	Effective rolling arc radius (measured from rolling arc centre point to midline of nearest lever arm)
R_o	Outer rolling arc radius (measured from rolling arc centre point to cracked surface of nearest lever arm)
u	Applied displacement
u_i	Crosshead displacement at time i
u_j	Crosshead displacement at time j
x_c	The current expected location of the crack tip directly underneath the centre of the rolling arc
W_d	Energy dissipated in the fracture process
W_e	Elastic energy stored in the beam
W_{fric}	Energy loss to friction in the system
W_{tot}	Total energy of the system
δ	Separation

δ_a	Distance between the surfaces of the beam ends at the specimen
δ_f	Maximum allowable separation between surfaces
δ_i	Separation between surfaces at a crosshead displacement u_i
δ_j	Separation between surfaces at a crosshead displacement u_j
δ_k	Distance between the surfaces of the beam ends at the specimen at the point k
Δa	Crack propagation
ΔA	New crack surface area created in the fracture process
Δa_{ss}	Crack propagation required to achieve a steady state in the fracture toughness response
Δu_k	Displacement undergone from when the point k passed the line between rolling arc centres
ΔW_d	Incremental change in energy dissipated in the fracture process
ΔW_e	Incremental change in elastic energy stored in the beam
ΔW_{fric}	Incremental change in energy loss to friction in the system
ΔW_{tot}	Incremental change in total energy of the system
κ	Beam curvature
σ	Traction
σ_{el}	Elastic traction (assuming no damage has occurred)
σ_i	Traction between surfaces at a crosshead displacement u_i
σ_j	Traction between surfaces at a crosshead displacement u_j
ϕ	Rotation of the rolling arc

4.1 Introduction

Extrinsic toughening, which acts in the wake of a crack front, is a differentiating factor between a controlled ductile failure and an unstable brittle failure. The rate of toughening will affect the crack propagation behaviour of the material regardless of whether the full extrinsic toughness is realised. In composite laminates, fibre bridging is a common observed extrinsic toughening mechanism.

Traditional fracture test methods, such as the double cantilever beam (DCB) test, typically perform better in the absence of large-scale extrinsic toughening. The underlying theory here does not account for traction acting behind of the crack tip, which alters the deflection of the beam. Traditional test methods can accurately capture intrinsic toughening mechanisms and the initial stages of crack propagation before extrinsic mechanisms have fully developed.

The DCB test is largely calibrated with a focus on intrinsic toughening mechanisms such as plasticity. Corrections can be applied to account for specimen size and rotation of the crack root [1]. These corrections do not account for the change in specimen profile in the presence of large-scale extrinsic toughening. Similar effects are found in other fracture test methods such as the compact tension test.

The DCB test, does not give details of the shape of traction-separation law (TSL) required to reproduce the measured response. Further approximate methods must be applied to the measured response to obtain the TSL. Understanding how different shapes of TSL affect laminate behaviour at a specimen level will have a direct impact on understanding the macroscopic behaviour of the material in structural applications, giving insight to future work.

The Double Rolling Arc Fracture Test (DRAFT) method, used here, is not entirely unique. Previous studies have used similar test methods. Sorensen et al [2] developed a fixture which applied pure bending moments to DCB

specimens, and used a scanning electron microscope is used to measure the delamination length. In another study by Sorensen and Jacobsen [3], the J-integral was applied to a beam loaded with applied end moments to determine the interfacial cohesive law.

Peel tests also use similar principles to those in the DRAFT method. In previous studies, peel tests have used mandrels to apply the force, resulting in a known curvature at the load point, as used by Breslauer and Troczynski [4]. The DRAFT method differs as the strained region of the beam remains conformed to the arc curvature for the duration of the experiment. Climbing drum peel tests work in a similar manner to the DRAFT rig, offering control of the curvature at separation. These tests have been standardised by ASTM [5]. There are similarities between the DRAFT method and two simultaneous climbing drum peel tests.

The authors believe the interpretation of the measured response has not been fully understood in previous studies. An analytical solution for a DCB with prescribed end rotations has been presented recently [6]. This study provides a similar solution, with specimen curvature dictated by the experimental apparatus. In another study, Škec and co-workers [7] note that when a prescribed moment is applied (to a DCB), the work of separation and the fracture toughness are the same; however when a prescribed load is applied they are not. This implies that the derivative of the J-integral with respect to crack opening displacement does not exactly capture the TSL.

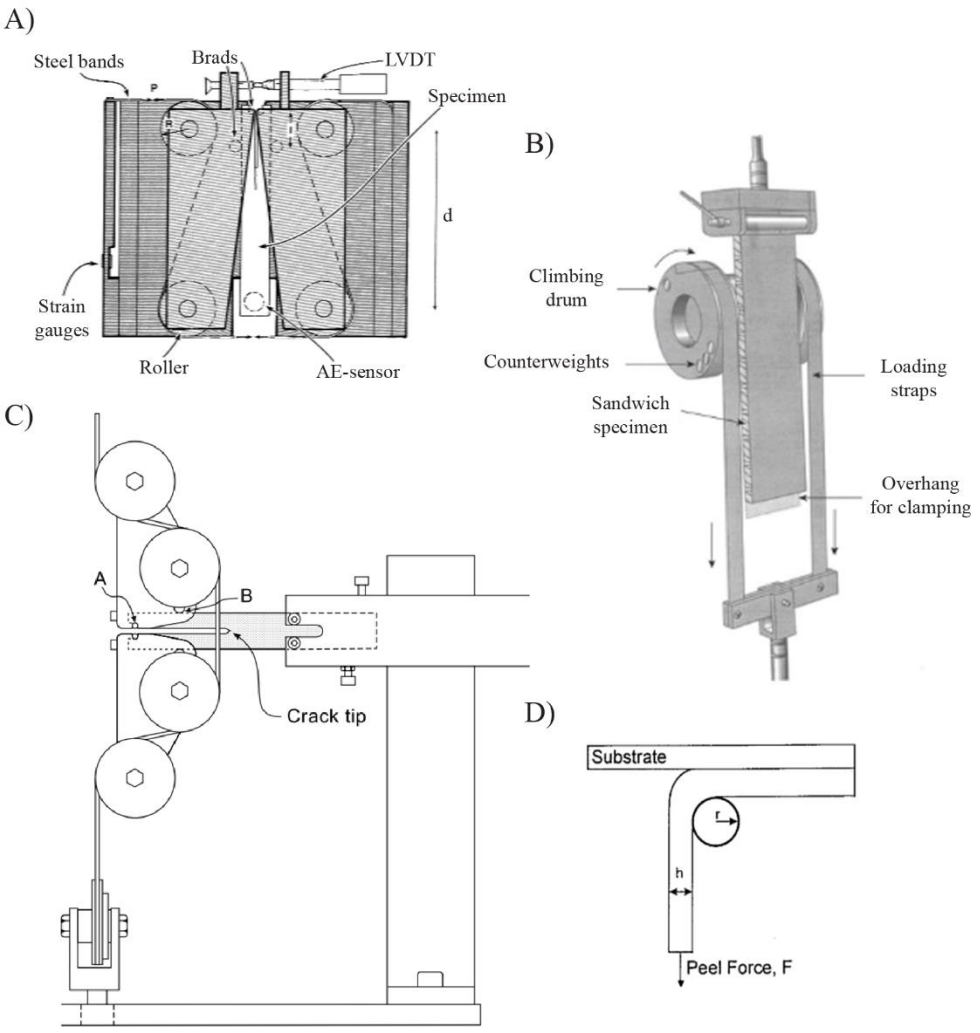

Figure 4-1 Examples of existing experimental configurations used in the literature (A) a DCB specimen loaded using a steel band and rollers by Sorensen et al. [2] (B) Broughton [8] used a climbing drum peel test to determine adhesive strength, the mechanism is similar to the DRAFT mechanism (C) Test fixture used by Sorensen and Jacobsen [3] to apply pure bending moments using steel wires and a pulley system (D) Peel test with a mandrel used by Breslauer and Troczynski [4], the mandrel dictates the local specimen curvature.

Studies of laminates experiencing extrinsic toughening [9–11] typically perform an inverse simulation; whereby experimental measurements are reproduced using a bilinear, trilinear or exponential TSL. These studies showcase that experimental measurements can be replicated in-silico but do not show how computational parameters affect the measured response. This study shows the effect of computational parameters on the measured response; and describes how these parameters should be chosen to replicate a given experimental response.

In a previous study we presented a systematic exploration of the parameter space for a TSL that considers both intrinsic and extrinsic toughening mechanisms. However, the TSLs were generally piecewise-linear with a small number of linear sections to reduce the parameter space. While this approach captures the key observed results (quantified by the initial toughness, the final toughness, and the crack growth to reach the final steady state value), it does not capture the exact shape of the TSL.

Here, we present an experimental approach that controls the beam curvature during crack propagation, which is directly controlled by machine crosshead displacement. A theoretical framework to determine the strain energy and fracture energy contributions during crack propagation are presented. As the crack opening displacements are imposed by the rollers, an arbitrarily shaped TSL can be determined from the energy release rate. Two different materials are tested experimentally and the resulting TSLs compared: providing insight into the material behaviour and guidance for future performance improvements. The TSLs generated are compared to DCB tests on the same materials and the limitations of the methods are discussed.

4.2 Methods

4.2.1 Experimental apparatus

The DRAFT mechanism is presented below (Figure 4-2A&B) and consists of two carriages; the outer carriage holds the rolling arcs, and the inner carriage holds the specimen. The inner carriage is also connected to the rolling arcs via two flexible, but inextensible, shims. The specimen is fixed at one end to the inner carriage and the beam ends at the pre-cracked end of the specimen are attached to the rolling arcs.

During a test, the outer carriage moves upwards. This pushes the rolling arcs upwards; however, the shims attached to the rolling arcs and the fixed stationary inner carriage cause the rolling arcs to rotate as they move. In turn, this imparts a curvature on the two ends of the pre-cracked specimen.

The assumed crack front is at the tangent point between the rolling arc and the uncracked section of the specimen and is colinear with the centre points of the rolling arcs. Therefore, as the carriage moves, it is assumed that the change in crack length a is equal to the carriage displacement u. The validity of this assumption is questioned in Section 4.4.1.2.

After the carriage has moved, the curved section of the beam will have length a and the rolling arc has rotated through an angle ϕ with $a = u = r\phi$, where r is the radius of the rolling arc. The distance between the centres of the rolling arcs is $2(r + h) = 2R_0$ and the distance δ_a between the surfaces of the beam ends at the specimen end can be determined.

$$\delta_a = 2R_o\left(1 - cos\frac{u}{r}\right) \qquad 4.1$$

In general, for a point k on the crack path, the separation for that point can be expressed in terms of the displacement undergone from when that point passed the line between the roller centres (i.e., the crack front) to the current time (Δu_k):

$$\delta_k = 2R_o\left(1 - cos\frac{\Delta u_k}{r}\right) \qquad 4.2$$

The motion of the system is shown in Figure 4-2; as the rolling arcs rotate and move upwards, note that the straight section of the shims and the straight section of the beam are a constant length as both are attached to either end of the inner carriage.

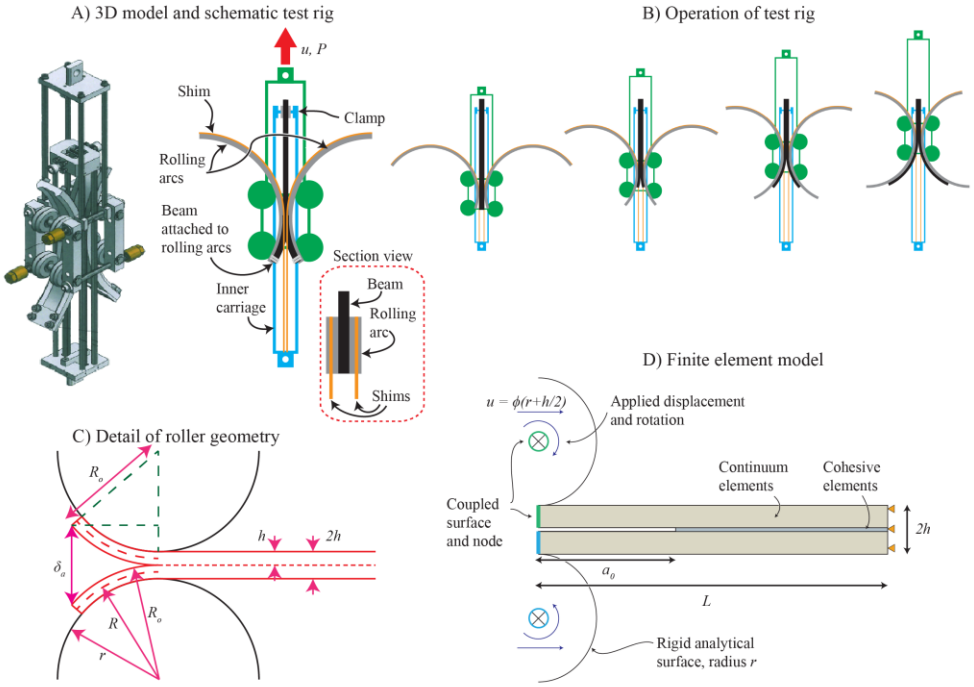

Figure 4-2 A) 3D model and schematic representation and B) 3D visualisation of the novel test rig. In both A) and(B), the applied load pulls the inner carriage (blue) downwards. Two flexible plates (orange) are connected to the rolling arcs so that downwards movement of the carriage causes rotation of the arcs; the arc rotate about a centre which is stationary relative to the outer frame (green). C) distinction between rolling arc radius, r, the radius of curvature, R, and the outer radius, R_o. R_o dictates the separation between layers, while R determines the current rotation of the rolling arc. D) Finite element model of novel test rig. Rolling arcs are modelled using rigid analytical surfaces and the interface is modelled with cohesive elements, governed by a traction-separation law.

4.2.2 Experimental approach

The specimen was mounted in the DRAFT rig which was controlled via crosshead displacement at a fixed velocity of $0.1\dot{6}\ mm/s$. The reaction loads generated were recorded and the interpretation of these is discussed in full below. The measured response (reaction force) has an initial rise from zero to a value of P_e , which is shown below to correspond to the strain energy in bending the beam arms. As the rolling arcs move along the beam, the crack length increases linearly (at the rate of applied displacement). Once the crack front reached the end of pre-cracked region, a_0, the measured force began to rise again; as there is now a dissipated energy contribution (in creating the new crack surface), along with the strain energy contribution to the total reaction force.

Two example materials were tested which are known to exhibit high and low amounts of fibre bridging, respectively; and are referred to as High Extrinsic Toughness (HET) and Low Extrinsic Toughness (LET). Both materials use the same resin and changes were made to the fibre tows to alter the extrinsic toughness. The details of these changes are commercially sensitive and not revealed by the manufacturer. The laminate lay-up in the test specimens was 24:$[0_9/-5/+5/0]_s$; the 5° offset is introduced to prevent "nesting" whereby fibres tows from neighbouring plies become intertangled; which occurs in purely 0° lay-ups. In other studies, increasing the fibre concentration has shown an increase in the composite tensile strength [12].

The specimens measured 250 mm in length, 2 mm in thickness and have a 25 mm breadth. A film insert was used in the manufacture of these specimens to produce a pre-cracked length of 20 mm. Additionally, DCB tests were performed on the same materials using the DCB fracture test method performed in accordance with the ASTM standards [1]. The compliance calibration method was used to calculate the crack growth release rate. The DCB specimens measure 250 mm in length, 3 mm in thickness and have a 25 mm breadth. A film insert was also used in the manufacture of these specimens to produce a pre-cracked of 30 mm.

4.2.3 Finite element model

A finite element model of the experimental setup is created; however, only the test specimen and rollers (rolling arcs) are considered (Figure 4-2D). The rollers are modelled as analytical rigid surfaces and are constrained to rotate as they move via an equation constraint, which represents the shims and moving carriage used in the experiment. The test specimen is modelled using two-dimensional plane strain elements CPE4I with a uniform out-of-plane thickness. Isotropic linear elasticity is assumed. The test specimen is constrained at one end and attached to the roller at the other. The end point of the roller is coupled to the end face of each of the beam ends (Figure 4-2D) such that the face follows the rotation and displacement of the roller.

The outer surface of the test specimen is in contact with the roller surfaces and the penalty contact method with frictionless behaviour is used.

The test specimen includes a pre-crack of length a_0 and the crack path is modelled using cohesive element with zero height. The cohesive elements in this model are four node 2D quadrilaterals with two integration points (COH2D4). The cohesive elements use a traction separation material definition which uses an elastic component which undergoes damage once a defined traction is reached. The damage variable allows for a piecewise linear traction separation law. Only normal displacements contribute to the damage criteria. Once the element is fully damaged, it is deleted from the finite element model. The traction in the material is calculated as:

$$\sigma = \sigma_{el}(1 - D) \qquad 4.3$$

where σ_{el} is the undamaged elastic traction across the interface. Thus, any TSL can be defined with the evolution of D described in terms of the separation.

In each simulation, the specimen is loaded via a displacement boundary condition applied to each roller, which also causes the roller to rotate via a constrain equation. A solution is obtained using an implicit solver (Abaqus 2018, Dassault Systèmes, RI, USA). In addition to the field variables in the test specimen, the reaction forces and displacements at the rollers are recorded. Due to the test geometry, the crack is assumed to advance in direct proportion to the roller displacement.

4.3 Theory

Here, we present a method of calculating the fracture toughness based on the measured reaction force in the experimental set up. By neglecting frictional losses and considering the strain energy and dissipated energy terms separately, it is shown that increases in the measured force (from the strain energy baseline P_e) can be directly attributed to the fracture energy.

The separation between laminates is directly related to the displacement, which is equivalent to the crack length, through the rolling arc radius. This relationship allows us to calculate the interfacial traction as the derivative of the fracture energy with respect to separation.

4.3.1 Simplified approach

The intrinsic and extrinsic fracture energies are related to the reaction forces generated during the test. First consider the curvature of the curved section of the beam which is in contact with the roller surface. The roller has radius r and the neutral surface of the beam is $h/2$ beyond that (Figure 4-2C), giving a radius of curvature $R = r + h/2$. We also note that the outer surface of the beam (on which the tractions will act) has radius $R_o = r + h$. Assuming the curvature remains constant (i.e., the beam remains in contact with the roller surface), the moment-curvature relationship for the beam is:

$$\kappa = \frac{1}{R} = \frac{M}{EI} \qquad 4.4$$

where E is the modulus and I is the second moment of area. This moment can be considered as applied to the end of the beam and is related to the reaction force on each roller (taken at the centre) using the same distance R as the moment lever arm:

$$P_r = \frac{M}{R} \qquad 4.5$$

Note the total reaction $P = 2P_r$ is the sum of both roller reactions. At the beginning of the test, there is no contribution from the fracture process as the beam includes a pre-crack of length a_o; therefore, the load applied is the load required to elastically deform the beam P_e and is a constant value (as the curvature is constant:

$$P_e = 2\frac{EI}{R^2} \qquad 4.6$$

Note that this includes contributions from both lever arms of the specimen.

The total work done during a test can be decomposed as follows:

$$W_{tot} = W_d + W_{fric} + W_e \qquad 4.7$$

where W_d is the energy dissipated during the fracture process, W_{fric} is energy lost to frictional losses, and W_e is energy stored during elastic deformation of the beams.

The amount of work done to advance the crosshead displacement from u_i to u_j can be treated similarly:

$$\Delta W_{tot} = \Delta W_d + \Delta W_{fric} + \Delta W_e \qquad 4.8$$

The stored elastic energy is equal to the elastic contribution of the work:

$$\Delta W_e = P_e(u_j - u_i) = P_e(a_j - a_i) = P_e \Delta a \qquad 4.9$$

Neglecting the contribution of friction, the total reaction force P can be similarly decomposed:

$$P = P_e + P_d \qquad 4.10$$

Where P_d is the force associated with the fracture process.

The strain energy release rate can be similarly compared to the dissipated work and the new crack surface area ΔA:

$$G = \frac{\Delta W_d}{\Delta A} = \frac{P_d \Delta a}{b \Delta a} = \frac{P_d}{b} \qquad 4.11$$

$$G(a) = \frac{P_d(a)}{b} \qquad 4.12$$

For materials where there is no change in G with crack growth, e.g., in the absence of extrinsic toughening mechanisms, G_{tot} is the key parameter and is readily determined from the load displacement plot (Figure 4-3B)

$$G_{tot} = \frac{P_{max} - P_e}{b} \qquad 4.13$$

In the case of a significant amount of extrinsic toughening, and the corresponding increase in crack growth resistance, the intrinsic toughness and extrinsic toughness are determined as follows. The intrinsic toughness is apparent on the force – displacement plot: once the crack begins to grow,

an almost instantaneous increase in force to $P_1$is apparent associated the intrinsic toughness. A similar calculation as for the total fracture energy in absence of extrinsic mechanisms is used:

$$G_{int} = \frac{P_1 - P_e}{b} \qquad 4.14$$

Note that amount of crack opening associated with the intrinsic fracture energy is small (on the order of 10-50 μm is typically used to capture intrinsic behaviour in fibre reinforced composites [13,14]). Consequently, the crack growth during the rise in force from P_e to P_1 is small (following Equation 4.1)

As the crack progresses, the force contributions to continue elastically deforming the beams and to create new crack surface (the intrinsic component only) remain constant as the curved region and crack area grow directly with displacement. Therefore, the remaining component of the force is associated with the extrinsic toughness:

$$G_{ext} = \frac{P_{max} - P_1}{b} \qquad 4.15$$

where P_{max} is the same final maximum value as before.

The crack growth Δa_{ss} required to reach a steady state toughness value (i.e., $G_{tot} = G_{ext} + G_{int}$) is easily identified from the load-displacement plot. This plateau is reached once there is a steady state turnover of fibres behind the crack tip. The force (and energy) increases until the fibres fail, and the tractions are removed. Therefore, the final length of the TSL is determined following Equation 4.2 as:

$$\delta_{ext} = 2R_o\left(1 - cos\frac{\Delta a_{ss}}{R}\right) \qquad 4.16$$

These three parameters are sufficient to generate a TSL which can capture the broad experimental trends. A tri-linear TSL is commonly used (as seen in chapter 3 and in literature [14–16]); however other forms such as an exponential decay during the extrinsic region are possible. The two fracture energies G_{int} and G_{ext} correspond to the area of the first and second

triangular regions of the TSL and for a tri-linear approach, the constraint mentioned above regarding a small crack opening for intrinsic toughness will also dictate the maximum traction. For a trilinear TSL, G_{ext} and δ_{ext} are both known, therefore σ_b is readily determined.

4.3.2 Arbitrarily shaped traction-separation law

In the previous approach, only the key fracture properties were determined, and assumptions were made about the form of the TSL. This approach is quick; however, it does not allow for detailed interrogation of extrinsic toughening mechanisms. Here, a method of defining an arbitrary piecewise linear TSL is presented. In this method, an incremental crack propagation details a section of the TSL which had not been described prior to that propagation as the separation between the laminates reaches a new maximum value (from δ_i to δ_j in Figure 4-3D).

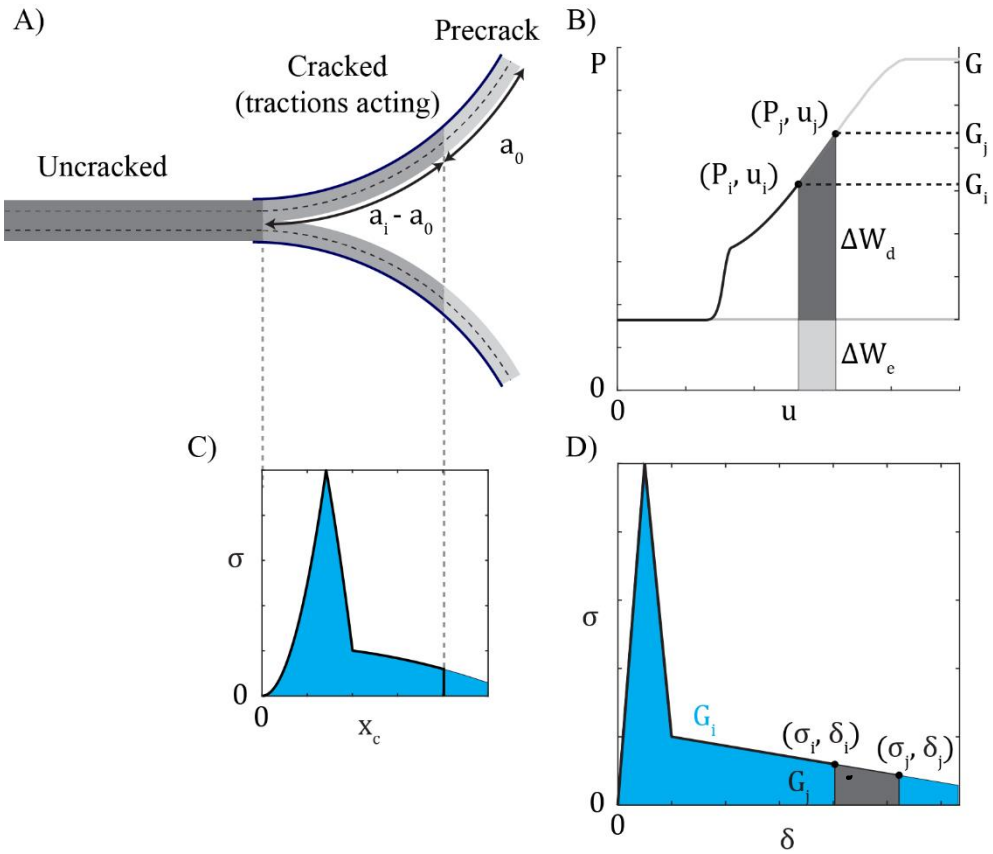

Figure 4-3 A) DRAFT specimen which has been loaded such that the current crack length is $a_i - a_0$. B) Resulting load displacement plot for DRAFT specimen at time i and at time j. The region ΔW_e is the change in strain energy from i to j and ΔW_d is the change in dissipated energy from i to j. C) Tractions σ as a function of distance from the crack tip x_c. Note that the TSL has not fully developed at this point (time i). D) Traction separation law at point i

and j, the region in grey has been developed from the crack propagating from a_i to a_j resulting in an energy dissipation of ΔW_d.

As discussed above, the number of bridging fibres accumulates behind the crack until fibre failure starts to occur, at which point a steady turnover of fibres continues. Consider a state i prior to reaching this steady state. The point Q at the end of the pre-crack will undergone a displacement following Equation 4.1 and the traction exerted will have followed the traction-separation law as the separation increased. The traction and separation at this point are σ_i and δ_i respectively, and the distribution of tractions behind the crack tip are shown in Figure 4-3C beneath the schematic diagram. For this explanation, a trilinear TSL is assumed (Figure 4-3D); the separation reached in this state i is also shown on the TSL. The reaction force P_i at u_i and the previous history are shown in Figure 4-3B.

Similar to the approach taken above for Equation 4.13, the fracture energy observed here (for the present amount of crack growth) is:

$$G_i = \frac{P_i - P_e}{b} \qquad 4.17$$

Note that once $P_i > P_1$, then G_i includes a constant intrinsic contribution G_{int}.

The current fracture energy is also apparent from the traction separation law:

$$G_i = \int_0^{\delta_i} \sigma \, d\delta \qquad 4.18$$

This is the shaded area in Figure 4-3D. Taking the derivative of both sides of Equation 4.18, we can obtain an expression for the current traction:

$$\sigma_i = \left(\frac{dG}{d\delta}\right)_{\delta_i} \qquad 4.19$$

Considering the current value of G_i and δ_i in addition to the previous data point G_j and δ_j (which have associated data P_j, u_j, and a_j) an approximation

of the derivative can be taken, and the traction is then obtained directly from the data.

$$\sigma_i = \frac{(G_j - G_i)}{(\delta_j - \delta_i)} \qquad 4.20$$

It is important to note that the tri-linear TSL was assumed here for illustration purposes and this approach is compatible with an arbitrarily shaped TSL.

Note that equation 4.20 can be rearranged to express the traction as a function of the derivative of the measured data, $\frac{dG}{du}$.

$$\sigma = \frac{dG}{d\delta} = \frac{1}{2}\frac{R}{R_0}\frac{1}{Sin\left(\frac{u}{R}\right)}\frac{dG}{du} \qquad 4.21$$

4.4 Results

4.4.1 Simulated response of an idealised material

In line with previous experimental and computational investigations [11,13,17], a representative tri-linear TSL (with fracture properties similar to those seen in CF composites [9,10]) is used to explore the behaviour of a material tested with the DRAFT apparatus. Figure 4-4 shows a typical deformed specimen shape obtained from a finite element analysis. The tractions acting at the interfacial cohesive layer are also shown. The reaction force measured at the roller reference points is shown in Figure 4-4D; the reaction force per unit width holds a steady value of P_0=0.2 N/mm (5 N for a 25 mm specimen) before the pre-crack is reached. This corresponds to the work needed to elastically deform the lever arms of the specimen. Once the pre-crack is reached, the measured reaction force begins to increase as energy required to advance the crack. The reaction force reaches a plateau once the intrinsic and extrinsic toughening mechanisms have been fully realised, i.e., the maximum allowable separation of δ_f has been reached ($\delta_f = 1.51$ mm in this case for $\Delta u = \Delta a = 12.3$ mm). The corresponding crack growth release rate is plotted on the secondary axis, as calculated based on the theory discussed above for Equation 4.17.

Finally, in order to demonstrate the reconstruction of an arbitrarily shaped TSL (as described in Section 4.3.2), the TSL of the idealised material is then calculated from the output only (i.e., Figure 4-4D) and presented in Figure 4-4E. The key features of the input behaviour are captured including the maximum traction, the separation for the intrinsic and extrinsic components, and the bridging tractions. Some fidelity with the original TSL is lost due to the numerical process and the sharp changes in traction with the input tri-linear law.

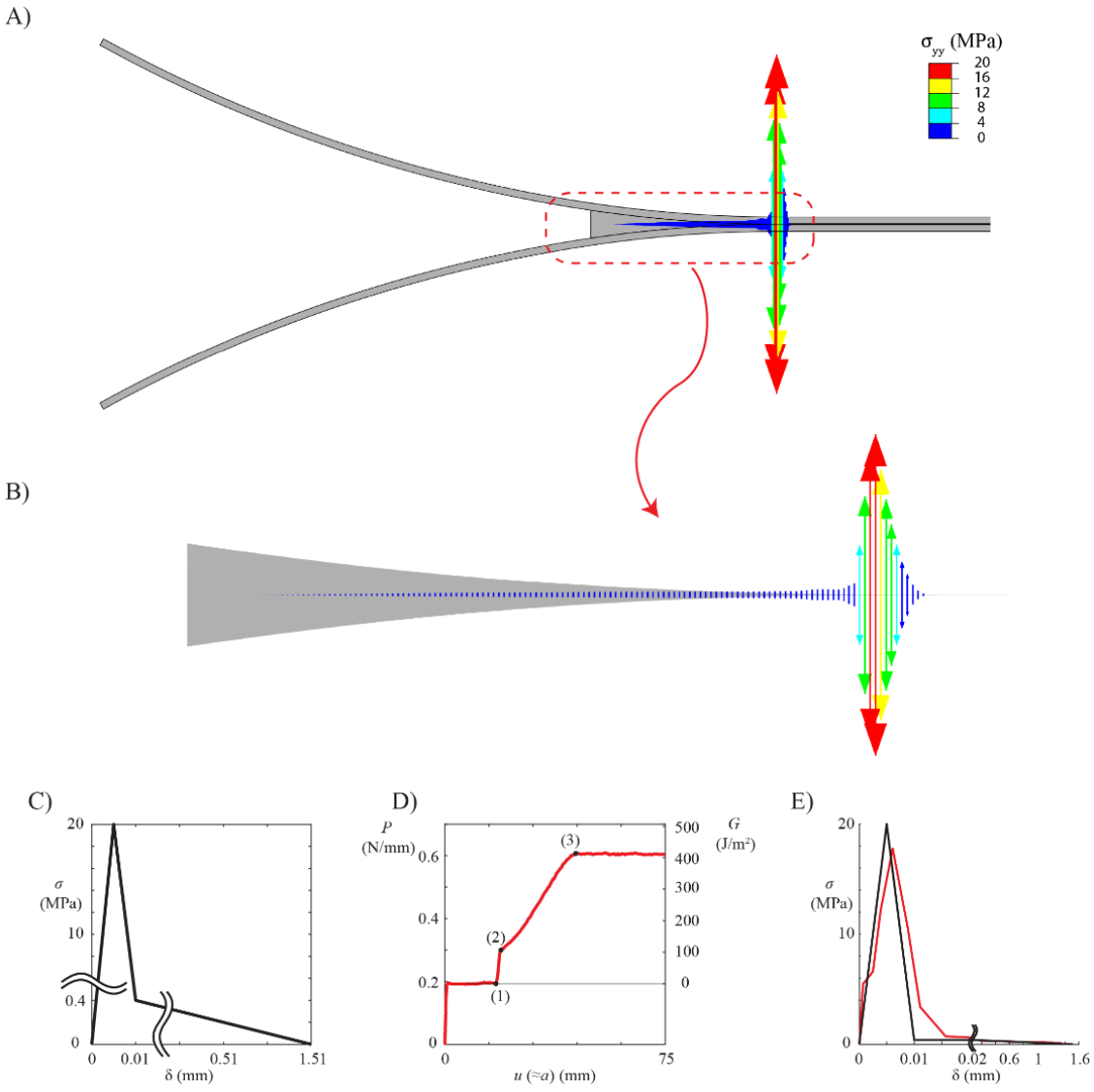

Figure 4-4 A) Deformed shape of specimen from a finite element analysis with overlaid tractions. B) Close up of overlaid tractions in the cohesive zone of the finite element model. C) Applied traction-separation law used to generate finite element response. D) Load-displacement response (and corresponding fracture toughness plotted in secondary vertical axis). The end of the pre-crack is reached at point (1), where crack propagation begins. The load increase at point (2) corresponds to the intrinsic toughness (e.g., resin) of the material

and point (3) is the steady state response when a constant turnover of bridging fibres is achieved. E) The input (black) and obtained (red) traction-separation laws (TSLs).

4.4.1.1 Parameter exploration.

To demonstrate the applicability of the methods for a range of fracture behaviours, TSLs with different combinations of extrinsic and intrinsic toughness (including various values of δ_{ext}) are considered. The TSLs are all constructed with the parameters listed in Table 4-1 and Table 4-2 and the other variables (σ_{int}, k_c and δ_{ext}) depend on the choice of G_{int} and G_{ext}. The simulated response for these different tri-linear TSLs is shown in Figure 4-5. The responses all show the instantaneous jump in load once the crack propagation begins (i.e., when $u = a_0$) followed by an increase up to the plateau value of load which correspond to G_{int} and G_{ext}, respectively. The output variables are then measured from the graphed data and compared to the input data (Table 4-2); expected values of G are observed for all scenarios.

Table 4-1 Default simulation parameters

a_0	L	b	$2h$	r	E	δ_{int}	δ_e	σ_{ext}
30	200	3	1	100	170	0.01	0.005	0.4
mm	mm	mm	mm	mm	GPa	mm	mm	MPa

Table 4-2 Default simulation parameters

Input					**Measured**		
G_{int} J/m^2	G_{ext} J/m^2	Δa_{ss} mm	σ_{int} MPa	δ_{ext} mm	G_{int} J/m^2	G_{ext} J/m^2	Δa_{ss} mm
100	100	7.152	20	0.5	100	105	7
100	200	7.152	20	0.5	100	205	7.5
100	200	10.066	20	1	100	205	10.5
200	100	7.152	40	0.5	200	110	7
200	200	7.152	40	0.5	200	210	8
200	200	10.066	40	1	200	215	10.5

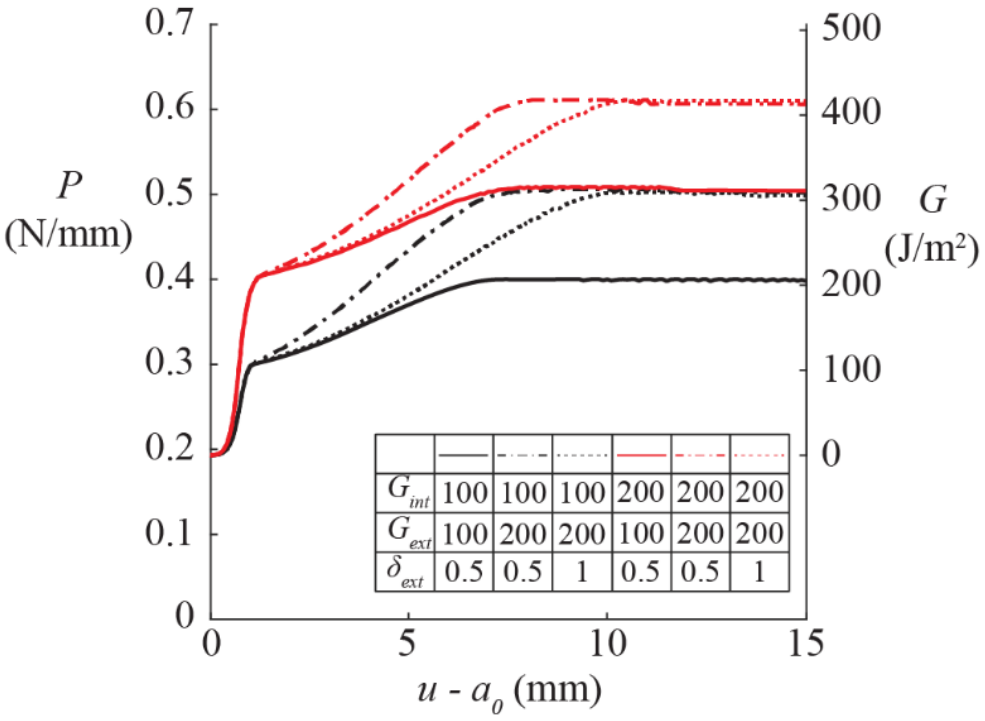

Figure 4-5 DRAFT responses for simulations with varying intrinsic and extrinsic toughness values. The default parameters used in these simulations are shown in Table 4-1. The other parameters (σ_{int}, k_c and δ_{ext}) depend on the choice of G_{int} and G_{ext} which are shown in the legend and in Table 4-2.

4.4.1.2 Effect of test geometry

Previously, all simulations used the same arc radius as in the prototype experimental set up; here, the effect of roller radius is demonstrated. The expected values of Δa_{ss} are shown for a range of maximum separations as a function of roller radius (Figure 4-6A). Depending on the expected behaviour, an appropriate rolling arc radius may be designed in order give adequate resolution in the calculation of the TSL from the observed data. For a representative TSL (Table 4-3), the effect of varying the rolling arc radius (from 75 to 200 mm) is explored.

Table 4-3 Parameters used to examine the effect of rolling arc radii

a_0	L	b	$2h$	E	δ_{int}	δ_e	δ_{ext}	σ_{int}	σ_{ext}
25	200	3	1	100	0.01	0.005	1.5	40	0.4
mm	mm	mm	mm	GPa	mm	mm	mm	MPa	MPa

Figure 4-6B shows an unexpected result; while all four simulations should show an almost instantaneous increase from 0 to the input intrinsic toughness value of $200\ \mathrm{J/m^2}$, the fracture energy increases gradually for radii greater than $75\ \mathrm{mm}$. This is due to the beam not remaining in contact with the rolling arc and thus not maintaining constant curvature. A similar effect occurs when the height of the specimen is varied (Figure 4-6C). As the specimen height increases, so too does the strain energy due to bending in the system (equations 4.6 and 4.9). Increasing the strain energy makes it more difficult for the specimen to conform to the rolling arc curvature as it is energetically favourable for the specimen to move away from the rolling arc surface.

Looking at the separation between the rolling arc and specimen in closer detail, Figure 4-6D shows the location of the crack surface on one of the lever arm (solid lines) and the expected location at $r + h$ from the centre of the rolling arc (relative to the current expected location of the crack tip directly underneath the centre of the rolling arc, x_c), when the centre of the rolling arc is at $u = 30$ mm. In the case of the $75\ \mathrm{mm}$ arc, there is a small offset between the expected and observed values; however, in the case of $125\ \mathrm{mm}$, the crack remains almost completely closed for $\approx 3\ \mathrm{mm}$ behind the crack tip. The values of δ_e and δ_{int} are shown for comparison. Figure 4-6E compares the expected (theory) and observed (FEA) surfaces, with the *y* coordinate normalised by the expected value (i.e., 1 corresponds to the beam perfectly conforming to the shape of the rolling arc and 0 is a completely closed crack) for the instant when the centre of the rolling arc is at $u = 30$ mm. In the case of the larger roller, the separation remains less than δ_e for approximately 4 mm behind the crack tip and the fracture process has not started at all; for the smaller rolling arc, the maximum traction (i.e., start of fracture process) is reached approximately 0.5 mm further behind the crack tip than expected. Thus, for the larger arc radii, the fracture energy is not correctly captured and the error in the results is substantial.

This error is a result of a combination of factors including: (i) axial deformation during bending leads to Poisson effect and a reduction in the specimen height, (ii) the cohesive tractions can substantially alter the shape of the beam if the flexural stiffness is sufficiently low and (iii) axial stretching in the straight section of beam ahead of the crack tip. A clear relationship between the flexural stiffness of the beam and the onset of this phenomena is not evident due to the non-linear relationship between tractions and separations.

The error can be reduced substantially by introducing an axial pre-strain in the specimen. In the simulation, this was achieved with a displacement applied to the fixed end of the specimen corresponding to 5% strain; however this introduces a second error, whereby the Poisson effect creates additional clearance between the beam and the rolling arc causing the load, and therefore the observed fracture energy, to increase before the end of the pre-crack is reached (Figure 4-6F). This may be compensated for by introducing a corresponding inwards movement of the rolling arcs in the simulation, or a preloaded spring to keep the arc in contact; however, the contact between the specimen and surface should be recorded. A similar result can be observed by considering a material with zero Poisson's ratio with the axial stretch applied; in this case, inwards movement of the rolling arc is not necessary and expected results are achieved. In both approaches, the final plateau value is approximately 5% lower; this is due to the axial stretch which alters the previous relationship between crack growth and displacement. The energy release rate is relative to the unstretched surface area; the 5% pre-strain causes an error of similar magnitude in the calculation of the area.

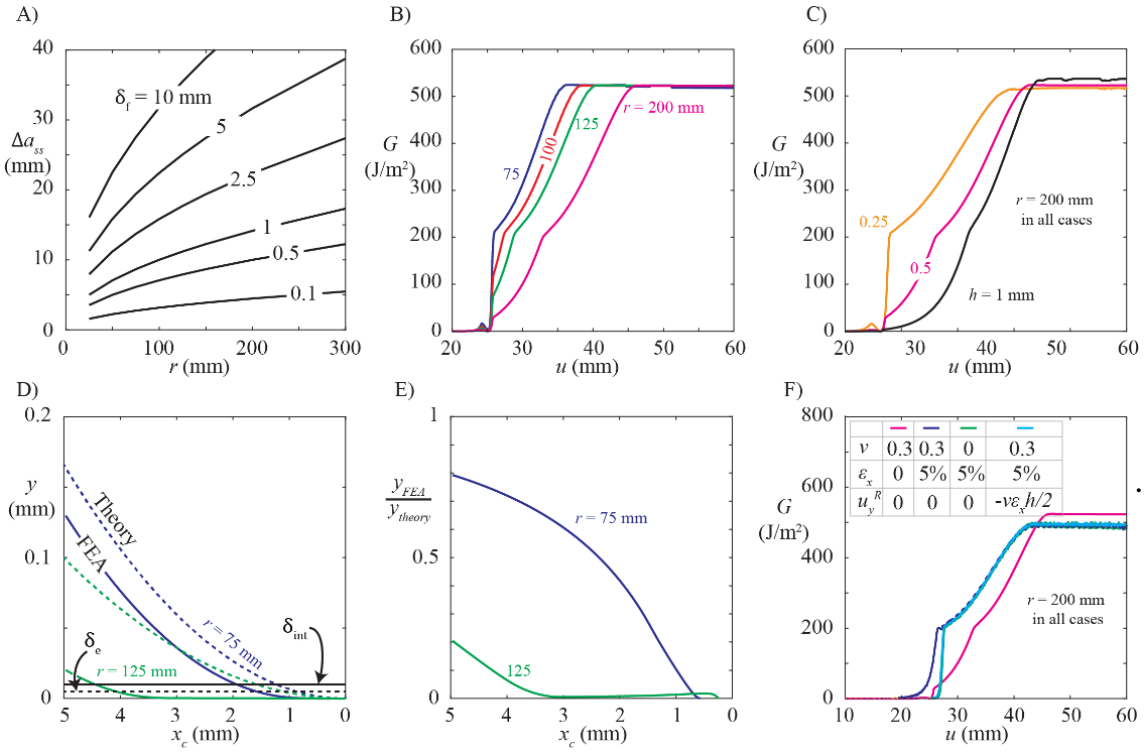

Figure 4-6 A) Δa_{ss} as a function of rolling arc radius for different values of δ_f as calculated by equation 4.16. B) Crack growth resistance curves with different rolling arc radii. All other model parameters are identical $a_0 =$ 25mm, $L = 200\ mm$, $2h = 1\ mm$, $b = 3\ mm$, $E = 100\ GPa$, $G_{int} = 200\ J/m^2$, $G_{ext} = 300\ J/m^2$, $\delta_{int} = 0.01\ mm$, $\delta_{ext} = 1.5\ mm$, $\sigma_{int} = 40\ MPa$ & $\sigma_{ext} = 0.4\ MPa$. C) Crack growth resistance curves with different specimen half height h, all other parameters are the same as the $r = 200\ mm$ case as shown in (B). D) Position of the specimen outer surface theoretically (equivalent to the rolling arc surface) and in FEA for $r = 75mm$ and $r = 125mm$ cases from (B). E) ratio of difference between theoretical and FEA y values as distance from the crack tip increases. F) Crack growth resistance curves for the $r = 200\ mm$ case. Various corrections for lag in response are applied: no correction (pink), 10 mm stretch in axial direction prior to crack propagation (purple), 10 mm stretch applied and $\nu = 0$ to supress Poisson effect (green), 10 mm stretch applied, $\nu = 0.3$ to allow Poisson effect to occur and an inward displacement of 9.69 μm applied to the rollers to counteract the Poisson effect (blue).

4.4.2 Estimation of fracture properties (validation)

Figure 4-7 shows the fracture energy for two different composite materials, one with a higher extrinsic toughness (fibre bridging) and one with a lower extrinsic toughness, hereafter referred to as HET and LET, respectively. Under testing with the DRAFT method, both materials increase in toughness at similar rates with respect to crack growth; however, the LET material reaches a plateau at a lower value. Although the performance of the materials is not the scope of this study, this suggests that the extrinsic toughening mechanisms, fibre bridging, proceeds in the same manner by peeling of fibres adhered to both laminates but that the failure of the fibres

is what determines the extrinsic toughness. Using the methods described above, an arbitrarily shaped TSL is determined for both materials and implemented in Abaqus. Examining the HET TSL in detail, the damage value D required to capture the TSL at $\delta = 4\ mm$ is greater than the value at $\delta = 8\ \mathrm{mm}$. Therefore, when implemented in the FEA package, the TSL is not correctly captured as D increases strictly monotonically. The increase in traction is then linear resulting in the dotted line shown in Figure 4-7B which excludes the shaded region of the TSL and substantially undervalues the fracture energy. This is seen in Figure 4-7C, where the TSL is used to reproduce the experimental data.

This limitation can be overcome by (i) using a non-linear behaviour for the undamaged elastic response that would allow the increase in traction to be captured, (ii) using a parallel network of elements where the elasticity of the intrinsic toughness and extrinsic toughness elements are represented separately or (iii), modifying the TSL so that the correct area/energy is captured. The first two approaches require the use of custom subroutines and the introduction of additional material parameters, increasing the burden for validation of TSL for use in applications. Here, the third method is used and the corrected TSL is generated as shown in Figure 4-7B. The FEA simulation with this response captures the plateau value in toughness correctly and the deviation introduced leads only to a small difference between the experimental and simulated data at $a - a_0 \approx 20\ \mathrm{mm}$. As a check on the modification, the area under the TSL is calculated via numerical integration and, using the relationship between separation and crack length established above, is plotted against crack length in Figure 4-7C.

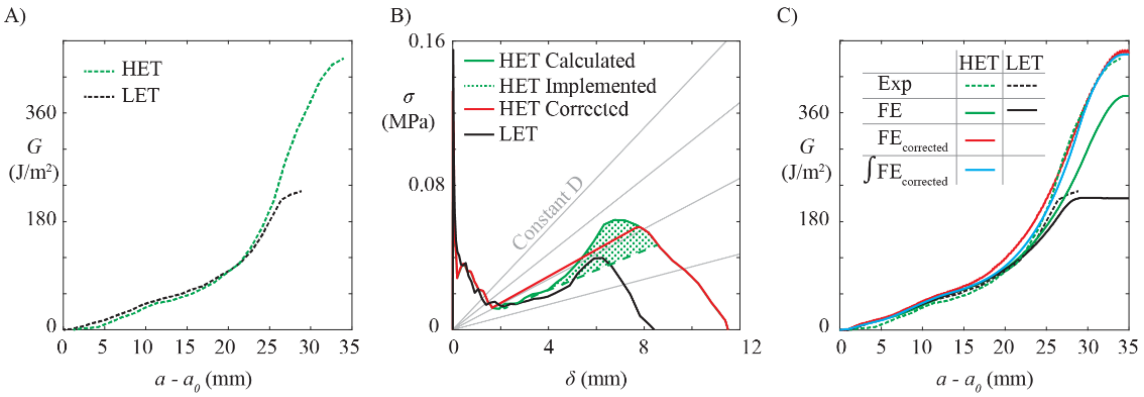

Figure 4-7 A) Experimental crack growth resistance data for both materials considered in this study. B) Traction separation laws generated using equations 4.2 and 4.20 based on the experimental data shown on the left. C) Measured finite element response using the traction-separation laws (B) overlaid with original experimental data (A).

4.4.3 Comparison between DCB and DRAFT measurements of fracture properties.

To highlight the strengths and weaknesses of both methods, a DCB and a DRAFT test are shown in Figure 4-8 including the experimental data and simulations using properties derived from both test methods. In both cases, an average of 4 experimental tests is shown. Considering the experimental data first, there is considerable difference in the shape of the response and the final value achieved. In the case of the DRAFT data, there is no sudden increase in G typically associated with the intrinsic toughness of the material which is clearly present in the DCB test. This is likely related to the phenomena discussed above in Figure 4-6 and a different test geometry may more clearly capture the true intrinsic toughness. The final steady state value of G is estimated to be up to 30% lower for the DRAFT measurement. In the case of the DCB test data, the compliance was used to determine the crack length, however, optical measurements were also periodically taken. Comparing the measured and calculated values (Figure 4-8D), the compliance is seen to overestimate a by ≈15% at the end of the test; this would lead to an overestimation of G for the DCB measurement shown in Figure 4-8B. The remaining difference can be attributed to the same error that caused the inaccuracy at the beginning of the test and frictional losses in the apparatus.

The TSL generated from the DCB test is tri-linear, following the methods outline in Chapter 3 and it is not possible to readily create a more accurately defined TSL from the standard DCB test. The simulations on both geometries are broadly similar with different crack propagations required to reach the plateau as this parameter is set by the test geometries. The TSL generated by the DRAFT rig has a substantially lower maximum stress, far below the transverse strength of this material, suggesting that it has not captured the correct value. Of more note is the second later peak in the tractions (discussed in detail above) which cannot be observed in the DCB test. Further refinement of the test parameters for the DRAFT rig is clearly necessary to more correctly capture the tractions associated with the intrinsic toughness.

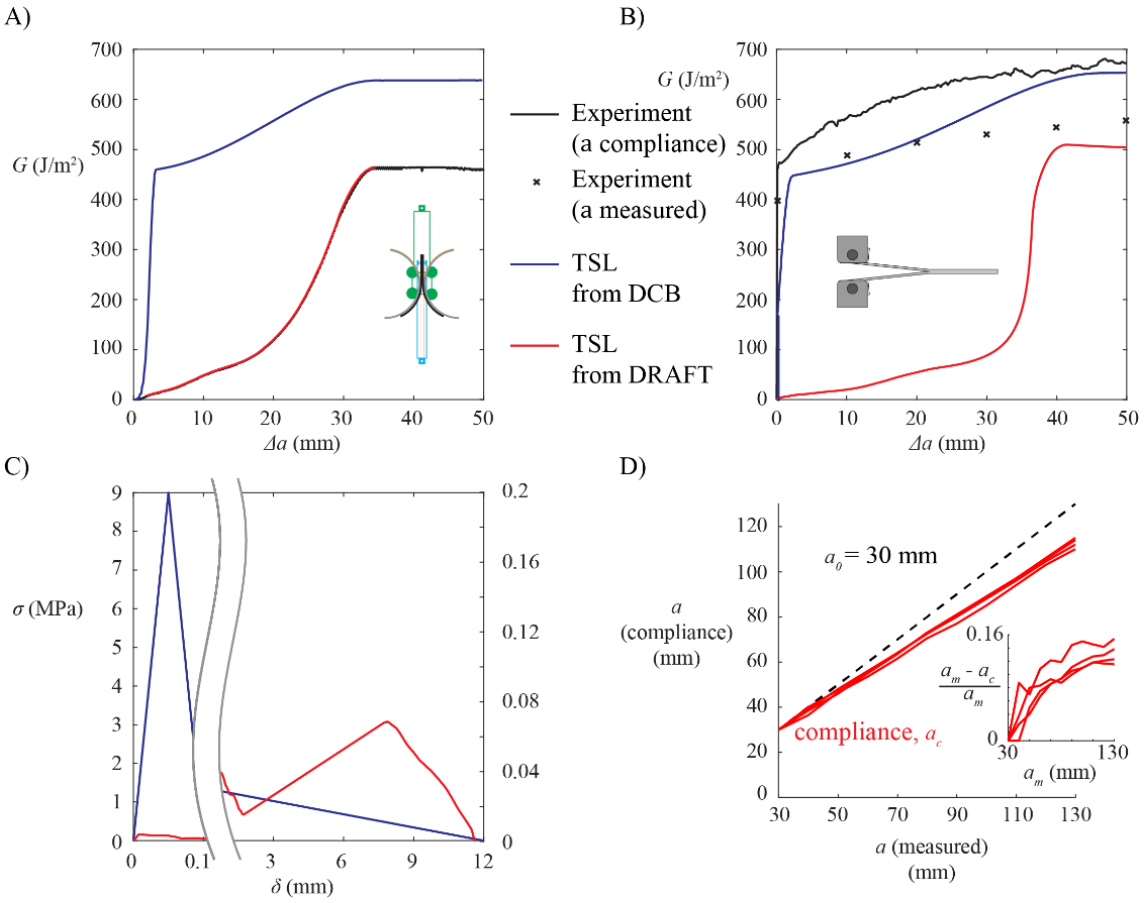

Figure 4-8 A) Comparison of average experimental data using HET material in DRAFT method (black), finite element response in a DRAFT simulation using a TSL generated from the experimental DRAFT data (red) and using a TSL generated from experimental DCB data (Blue). B) Comparison of average experimental data using HET material in DCB method (black), finite element response in a DCB simulation using a TSL generated from the experimental DRAFT data (red) and using a TSL generated from experimental DCB data (Blue). C) TSL generated from experimental DRAFT data (red) and from experimental DCB data (blue). D) Comparison of crack lengths by physical measurement using a ruler (black) and approximated using the specimen compliance (red) in experimental DCB tests with the HET material

4.5 Concluding remarks

In the present study, we have described a new test method and shown how it can be used to investigate extrinsic toughening mechanisms in fibrous materials. The test method offers advantages over the standard DCB test; however further refinement is needed to improve the accuracy of the test method.

The DRAFT apparatus aims to simplify the measurement of fracture energies by keeping the strain energy contribution well defined through imposition of a constant curvature similar to the applied moment test used by Sørensen

and Jacobsen [3]. In the present work, the external work can be compared to the strain energy stored during the applied deformation to determine the energy released during fracture. This method has the potential to determine the detailed shape of the traction separation law once the constant curvature is imposed on the test specimen. Comparing the two materials tested, which were known to have different extrinsic toughness values, reveals that the tractions generated are broadly similar but in the tougher material, the maximum separation is much higher. This understanding of the extrinsic toughening can help guide future material development.

The DRAFT method was not able to accurately capture the intrinsic toughness and was more than an order of magnitude in difference to that noted by the DCB method. It is important to note that in the TSL determined from the DCB test, the maximum traction was a choice of the user, typically chosen to be the transverse toughness of the material [13,18,19]. As the intrinsic toughness will dictate the onset of initial crack propagation, the TSL determined from the DRAFT method should not be used in simulations of applications using the materials. The origins of the error are discussed above and the parameters of the test, such as the roller radius, should be changed to improve the measurement until closer agreement is observed. Due to the complexity of manufacture, it was not possible to manufacture a different test apparatus within the scope of the current study. In the following chapter, an alternative method to determine the TSL from a DCB test is presented to investigate if the second peak in the TSL is a true phenomenon of the material or a test artifact. Previous studies have looked at a second peak [20], but not in the context of an arbitrarily shaped TSL. A TSL with more than one peak poses implementation challenges which may limit their applicability in simulations of load cases and larger simulations in automotive and aerospace applications.

In conclusion, we have presented a method to interrogate the crack growth release rate of materials while keeping the strain energy known. While the method was shown to work for idealised materials, in experimental testing

of two materials, the test geometry was found to introduce errors which made the absolute values of fracture energy not comparable to other measurements. The test method did reveal detailed information about the tractions exerted on the crack surface due to extrinsic mechanisms and provide insight into the differences in behaviour between materials. Further work is necessary to overcome the issues raised and the verify the results observed.

4.6 References

[1] ASTM. Standard Test Method for Mode I Interlaminar Fracture Toughness of Unidirectional Fiber-Reinforced Polymer Matrix Composites 1 2013. https://doi.org/10.1520/D5528-13.

[2] Sørensen BF, Horsewell A, Jørgensen O, Kumar AN, Engbaek P. Fracture Resistance Measurement Method for in situ Observation of Crack Mechanisms. J Am Ceram Soc 1998;81:661–9. https://doi.org/10.1111/j.1151-2916.1998.tb02387.x.

[3] Sørensen BF, Jacobsen TK. Determination of cohesive laws by the J integral approach. Eng Fract Mech 2003;70:1841–58. https://doi.org/10.1016/S0013-7944(03)00127-9.

[4] Breslauer E, Troczynski T. Determination of the energy dissipated during peel testing. Mater Sci Eng A 2001;302:168–80. https://doi.org/10.1016/S0921-5093(00)01370-8.

[5] ASTM D1781 - 98. Standard Test Method for Climbing Drum Peel for Adhesives. Astm 2012;98:9–12. https://doi.org/10.1520/D1781-98R12.2.

[6] Škec L, Alfano G, Jelenic G. Complete analytical solutions for double cantilever beam specimens with bi-linear quasi-brittle and brittle interfaces List of symbols. Int J Fract 2019;215:1–37. https://doi.org/10.1007/s10704-018-0324-5.

[7] Škec L, Alfano G, Jelenić G. On Gc, Jc and the characterisation of the mode-I fracture resistance in delamination or adhesive debonding. Int J Solids Struct 2018;144–145:100–22. https://doi.org/10.1016/j.ijsolstr.2018.04.020.

[8] Broughton W. Testing the mechanical, thermal and chemical properties of adhesives for marine environments. Adhes Mar Eng 2012:99–154. https://doi.org/https://doi.org/10.1533/9780857096159.2.99.

[9] De Morais AB, Pereira AB. Application of the effective crack method to mode I and mode II interlaminar fracture of carbon/epoxy unidirectional laminates. Compos Part A 2007;38:785–94. https://doi.org/10.1016/j.compositesa.2006.09.001.

[10] Yang Q, Cox B. Cohesive models for damage evolution in laminated composites. Int J Fract 2005;133:107–37. https://doi.org/10.1007/s10704-005-4729-6.

[11] Shokrieh MM, Daneshjoo Z, Fakoor M. A modified model for simulation of mode I delamination growth in laminated composite materials. Theor Appl Fract Mech 2016;82:107–16. https://doi.org/10.1016/j.tafmec.2015.12.012.

[12] Thomason JL. The influence of fibre length, diameter and concentration on the strength and strain to failure of glass fibre-reinforced

polyamide 6,6. Compos Part A Appl Sci Manuf 2008;39:1618–24. https://doi.org/10.1016/j.compositesa.2008.07.002.

[13] De Morais AB. A new fibre bridging based analysis of the Double Cantilever Beam (DCB) test. Compos Part A Appl Sci Manuf 2011;42:1361–8. https://doi.org/10.1016/j.compositesa.2011.05.019.

[14] Gutkin R, Laffan ML, Pinho ST, Robinson P, Curtis PT. Modelling the R-curve effect and its specimen-dependence. Int J Solids Struct 2011;48:1767–77. https://doi.org/10.1016/j.ijsolstr.2011.02.025.

[15] De Morais AB. Double cantilever beam testing of multidirectional laminates. Compos Part A Appl Sci Manuf 2003;34:1135–42. https://doi.org/10.1016/j.compositesa.2003.08.008.

[16] Heidari-Rarani M, Shokrieh MM, Camanho PP. Finite element modeling of mode I delamination growth in laminated DCB specimens with R-curve effects. Compos Part B Eng 2013;45:897–903. https://doi.org/10.1016/j.compositesb.2012.09.051.

[17] Sørensen BF, Jacobsen TK. Large-scale bridging in composites: R-curves and bridging laws. Compos Part A Appl Sci Manuf 1998;29:1443–51. https://doi.org/10.1016/S1359-835X(98)00025-6.

[18] Hodgkinson JM. Mechanical Testing of Advanced Fibre Composites. 2000.

[19] De Morais AB, De Moura MFSF. Assessment of initiation criteria used in interlaminar fracture tests of composites. Eng Fract Mech 2005;72:2615–27. https://doi.org/10.1016/j.engfracmech.2005.05.003.

[20] Sills RB, Thouless MD. Cohesive-length scales for damage and toughening mechanisms. Int J Solids Struct 2015. https://doi.org/10.1016/j.ijsolstr.2014.06.010.

Chapter 5. Experimental fracture behaviour of composite specimens experiencing fibre bridging

Abstract

In literature, a bilinear damage model is commonly used to describe extrinsic toughening mechanisms in a traction-separation law. This type of damage model does not capture non-linear traction-separation behaviour. In the previous chapter the DRAFT method of capturing non-linear behaviour is described. However, the DRAFT method is not directly comparable with existing data. Here, a standardised fracture test method is modified to measure local specimen rotation. Pins are inserted into the specimen to increase the length of the surface normal, while images are taken throughout the experimental procedure. The local rotation data is related to interfacial traction through Euler-Bernoulli beam bending theory. The method presented here shows non-linear material behaviour in the traction-separation law as seen in experimental results of the same material from the previous chapter. However, the resolution of the traction-separation law produced can be improved. Recommended improvements to the experimental procedure are provided.

Nomenclature

a	Crack length
a_0	Pre-crack tab length
b	Specimen breadth
C	Compliance
E	Young's modulus
G	Fracture energy
G_{ext}	Extrinsic fracture energy
G_{int}	Intrinsic fracture energy
G_0	Total fracture energy
G_I	Mode I fracture energy
h	Thickness of one DCB specimen arm (or a single cantilever)
I	Second moment of area
L	Beam length
M	Moment
n	Order of polynomial fit to θ
n_{cc}	Fitting parameter used in compliance calibration calculation
P	Applied load
t	Time
u	Applied displacement
V	Shear force
x	x coordinate in cartesian coordinate system
x_a	First x coordinate of cantilever beam between which the traction ω acts
x_b	Second x coordinate of cantilever beam between which the traction ω acts
y	y coordinate in cartesian coordinate system
Δa_{ss}	Crack length required to achieve a steady state distribution of fibre bridging
δ	Separation
δ_e	Separation at the maximum traction of the intrinsic region

δ_f	Maximum allowable separation
δ_{int}	Separation at the transition from intrinsic to extrinsic regimes
θ	Rotation/slope
$\bar{\theta}$	Slope averaged over five frames
θ_i	Slope of pin i
$\theta_{i,t=0}$	Slope of pin i at time $t = 0$
$\bar{\theta}_{Mono}$	Slope averaged over five frames and monotonically increasing
θ_{orig}	Original slope before processing
θ_{RBM}	Slope of free end of DCB used to account for rigid body motion
κ	Beam curvature
σ	Traction
σ_{ext}	Extrinsic traction, associated with fibre bridging behaviour
σ_{int}	Maximum intrinsic traction
ω	Traction per unit breadth

5.1 Introduction

This chapter further examines the traction-separation law (TSL) following the suggestion in chapter 4 that there is a second peak in the TSL (see Figure 5-1A). Here, a modification is made to the DCB method to analyse the shape of the TSL using simpler methods than in Chapter 4. In chapter 3, the DCB method is examined in detail, showing a clear relationship between test parameters and interface properties. However, in chapter 3 it was assumed that a trilinear traction-separation law (TSL) represented the R-curve response. In actuality, the trilinear TSL captured the key features of the R-curve but not the detailed shape of the curve. The DRAFT method (described in chapter 4) can determine a piecewise linear TSL based on the load-displacement response which is akin to the crack length-fracture toughness response. The DRAFT method captures nonlinear traction separation behaviour but is not practical to apply in an industry setting as the test apparatus is difficult to use and the results can be queried as the specimen

may not conform to the exact radius of the rolling arcs. The resulting data is not readily comparable with existing DCB tests.

Detailed investigations of the TSL have been performed before using peel tests [1] and end moments applied to DCB specimens [2]. Peel tests are less suitable for laminate composites due to the small radius of the mandrels used and similar issues as with the DRAFT method can occur. Using end moments instead of the typical point loads on a DCB allows the use of the J-integral method to determine tractions as a function of crack opening; Sørensen and Jacobsen [3] derived cohesive laws with either a plateau followed by a monotonic decrease in traction or a simple monotonic decrease in traction without a plateau. Previous studies have used digital image correlation (DIC) to track the motion of a timber DCB specimen and determine an interface law from DIC [4]. The strain energy release rate is determined for the images and an empirical TSL is fit to this data.

While these test rigs can be used to derive a cohesive law, the data gathered is not directly comparable with existing DCB data. Therefore, a method of deriving a nonlinear traction-separation law (TSL) from DCB fracture tests would be advantageous. While most of the literature assumes a trilinear TSL to model extrinsic toughening, Sills and Thouless consider a traction-separation law with a second peak in traction response suggesting a larger traction is present at higher separation between the surfaces [5]. This law is not arbitrarily shaped, however, and is a composite of typical idealised curves.

Figure 5-1 shows TSL data derived from experimental results using the DRAFT method in chapter 4. A second peak is evident in the TSL shown (Figure 5-1A). Betterman et al. propose that the length of fibres affects the peak stress achieved and the behaviour after the peak (Figure 5-1C) [7]. It is feasible that a combination of these effects could produce the behaviour seen in chapter 4.

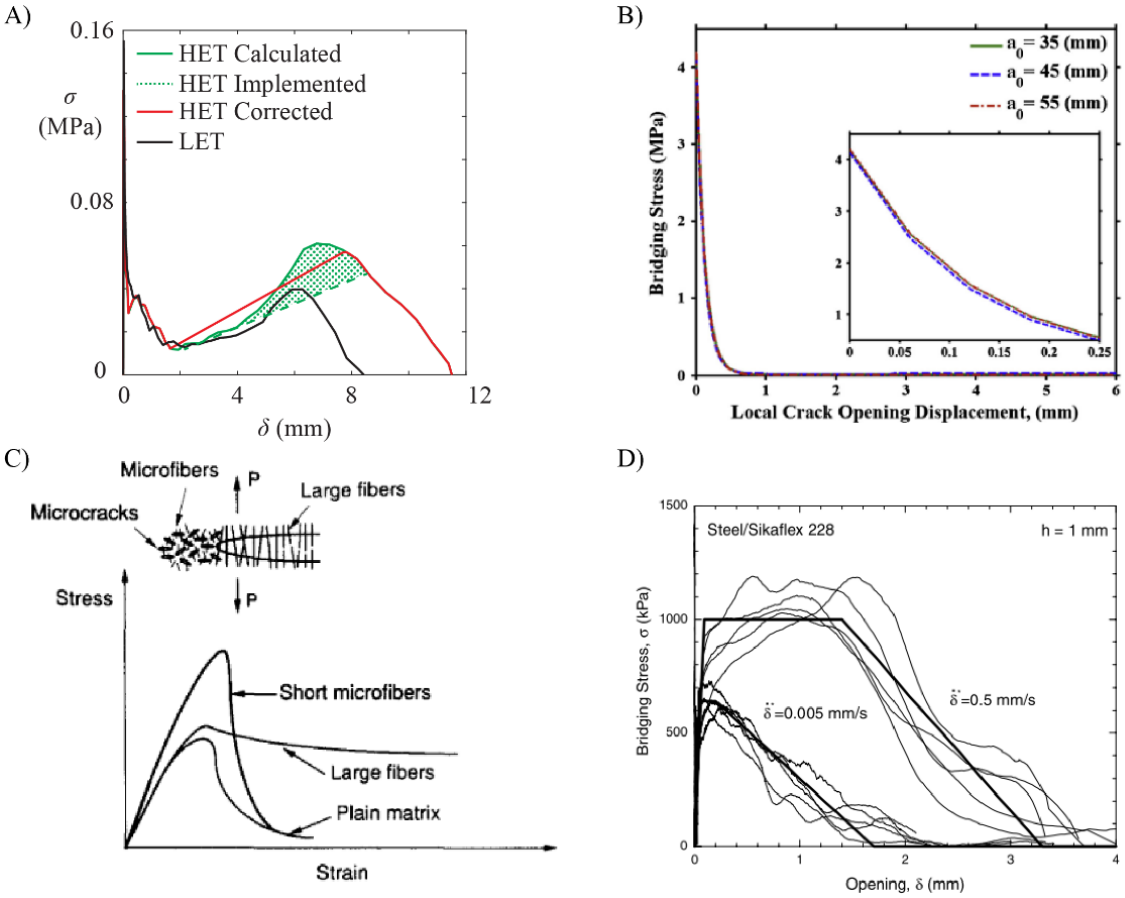

Figure 5-1 A) Traction separation laws derived from experimental DRAFT data presented in chapter 4. For both High Extrinsic Toughness (HET) and Low Extrinsic Toughness (LET) materials, a second peak in the traction response is seen at a separation of approximately 6 mm. B) Shokrieh calculates the TSL for three different pre-crack lengths using experimental measurement of the crack tip opening displacement and the J-integral [6]. C) Differing shapes of stress strain response proposed by Betterman et al. based on representative length of fibres in the material [7]. D) TSL shape measured for a DCB sandwich material by differentiation of the $J-\delta$ curve and overlaid multilinear cohesive law fit (bold) [8].

In computational work the TSL is commonly computed using the J-integral. In experimental work the TSL is typically found using approximate methods, such as the compliance calibration method, but a number of papers have experimentally determined interface laws. Shokrieh [6] tested DCB specimens with bridging lengths of ≈10 mm and found an exponential decay in the traction separation response using the simple beam theory to approximate the fracture toughness. Zhu measured rate dependent TSLs in polyurea/steel sandwich materials using tensile and shear tests [9]. In this study, Zhu reported that the TSL had a parabolic shape and the fracture toughness and peak of the TSL depend on the loading rate. Betterman et al. [7] show that the peak in a stress-strain response changes based on the fibre

properties (fibre diameter and volume fraction), with short or long fibres having different peaks (see Figure 5-1C). Jacobsen and Sørensen measured a nonlinear softening TSL and compared it to a micromechanical model of fibre crossover bridging. They computed a power law TSL. They compared experimental and computational R-curves to find good agreement between both [10,11]. Sørensen et al. have more recently developed a micromechanical model for fibre crossover bridging for mixed mode loading of DCB specimens [12]. They found that the toughening due to crossover bridging is much higher in mode II or mixed mode loading than in pure mode I loading. Sills and Thouless also model a discrete fibre debonding from both surfaces at the crack interface to investigate crack jumping [5].

Here, a standardised double cantilever beam (DCB) test is modified to allow additional data to be gathered based on measurement of the rotation at several points on the specimen. This experiment uses pins to increase the length of the surface normal, which allows simple discrete measurement of the rotation. A digital camera is used to capture images as the test progresses. These images are used to infer the interfacial traction separation law of the material by means of relating the discrete slope measurement to the applied distributed load through Euler-Bernoulli beam bending equations. The goal of this modification is to capture the detailed interface response in a similar manner to the DRAFT rig (chapter 4); while using a standardised test that can be readily implemented in industry (chapter 3). Using a modified DCB test is beneficial in an industry setting as (i) the machining and tooling costs associated with the production of a DRAFT fixture do not exist. The modifications to the DCB experiment do not require excessive tooling. (ii) machine operators do not require training on how to complete a new fracture test method. (iii) gathered data is directly comparable with existing DCB test data.

5.2 Methodology

5.2.1 Material description & specimens

Carbon fibre laminates were created consisting primarily of 0° plies with the plies either side of the central ply offset at 5° (24:$[0_9/-5/+5/0]_s$). The offset plies prevent the occurrence of nesting in a purely unidirectional 0° laminate. Two material systems are considered which are known to experience either a high or low amount of fibre bridging/extrinsic toughening; hereafter referred to as *HET* (High Extrinsic Toughening) and *LET* (Low Extrinsic Toughening) respectively.

Pre-cracked specimens were created by inserting a shim in between the plies during the manufacturing process as shown in Figure 5-2A. Specimens manufactured for the DCB tests were 250 mm long with a 30 mm pre-crack and had a height of 3 mm and breadth of 25 mm. The number of specimens used for each load condition is given in Table 5-1. Figure 5-2B shows the specimen geometry for the DCB.

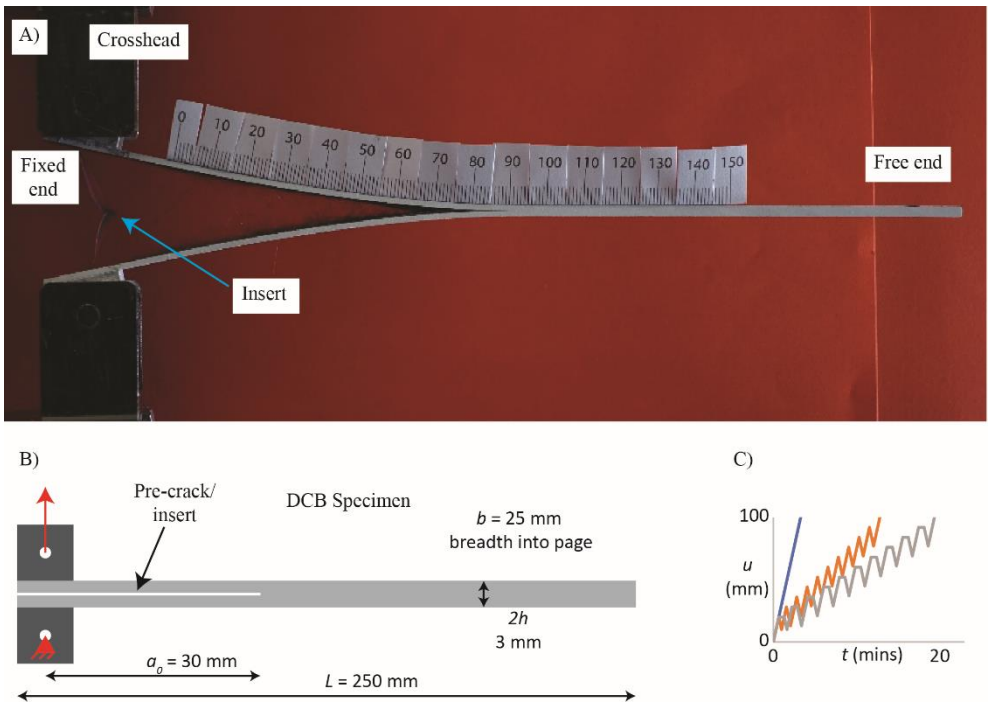

Figure 5-2 A) Experiment configuration including DCB specimen with load applied via a uniaxial tensile tester. The current delamination length is approximately 80 mm. Fibres can be seen bridging the interface between the laminates. A tab insert used in the manufacturing process to create the pre-crack at the fixed end of the specimen is also visible. B) Schematic diagram of the DCB specimen and loading blocks. C) Loading patterns used are *load throu*gh (blue), *load/unload* (orange), and *pause* (grey) shown on the right of the image.

Table 5-1 List of DCB experiments conducted.

Load pattern	Material	Number of samples	Rationale
Load through	*LET*	1	Compare results to examine if unloading affects macroscopic behaviour
	HET	1	
Load/Unload	*LET*	5	Standard DCB analysis
	HET	5	
Pause	*LET*	1	Investigate if creep behaviour is present in the materials
	HET	1	
Load/Unload	*HET*	1	Use pins to enhance the surface normal, increasing the accuracy of the measured curvature

5.2.2 DCB methodology

The DCB test was performed following the ASTM standard [13]. The peak in the load displacement plot was used to identify the onset of fracture. The fracture energy was determined using the Compliance Calibration method (Equation 5.1) (the alternative methods are discussed further in Chapter 2):

$$G_I = \frac{n_{cc} P u}{2ba} \tag{5.1}$$

Where G_I is the mode I fracture energy, P is the applied load, u is the load-line displacement, b is the specimen breadth, a is the crack length, Δ is the crack tip rotation factor, n_{cc} is the exponent relating compliance $C = u/P$ to crack length

The crack length was measured using two methods (i) visually using a flexible, calibrated linear scale adhered to the specimen and an approximation based on the compliance, which provided a higher number of data points than the first method. The approximation gives the crack length as:

$$a = \left(\frac{3}{2}EIC\right)^{\frac{1}{3}} \qquad 5.2$$

where E is Young's modulus, I is the second moment of area of the beam and C is the beam compliance $C = u/P$.

Three loading patterns are used in the DCB experiments to examine the material behaviour. These loading patterns are shown in Figure 5-2C. and described below. In all cases the loading/unloading is performed at a crosshead speed of 0.1666 mm/s**.**

1. *Load through* – a linearly increasing crosshead displacement is applied until the crack has propagated approximately 100 mm
2. *Load/unload* –a linearly increasing crosshead displacement is applied until the crack has propagated 10 mm after which the crosshead is reversed for 10 mm of crosshead displacement (however, the reaction force is not permitted to fall below 20 N to prevent compression of fibres in the process zone). After the unloading, the crosshead is reversed to the original direction and proceeds until a further 10 mm of propagation occurs and this procedure repeats for 10 cycles (giving a total of ≈100 mm of crack propagation).
3. *Load/Pause* – a linearly increasing crosshead displacement is applied as in case 2; however, before reversing the crosshead direction of travel, the crosshead is held stationary for 30 seconds. The unloading and reloading of the sample proceed as in case 2 for 10 cycles.

5.2.3 Modified DCB methodology

In an experiment using a *HET* material specimen, the curvature is measured as described below and used to calculate the interface tractions. A series of holes are drilled at 5 mm centre-to-centre spacing into the top of the specimen to a depth of one quarter of the total thickness. The first pin is 27.5 mm from the end of the pre-crack. Cylindrical aluminium pins are inserted and fixed using a cyanoacrylate adhesive. It is difficult to ensure the pins are perfectly normal to the specimen as the depth which they are inserted is shallow (0.75 mm). The initial position of the pins should aim to be normal to the surface. Some deviation is allowed as the change in angle of the pins is of interest, not the current angle.

During the DCB experiment, a camera (Sony RX100 mark IV) was used to capture sequential images of the test at 1 second intervals. The camera was set up on a tripod and placed orthogonal to the test specimen at 635 mm as shown in Figure 5-3. This experiment is conducted based on DCB methodology described above using a *Load/unload* pattern, with load reversals at intervals of approximately 10 mm of crack propagation.

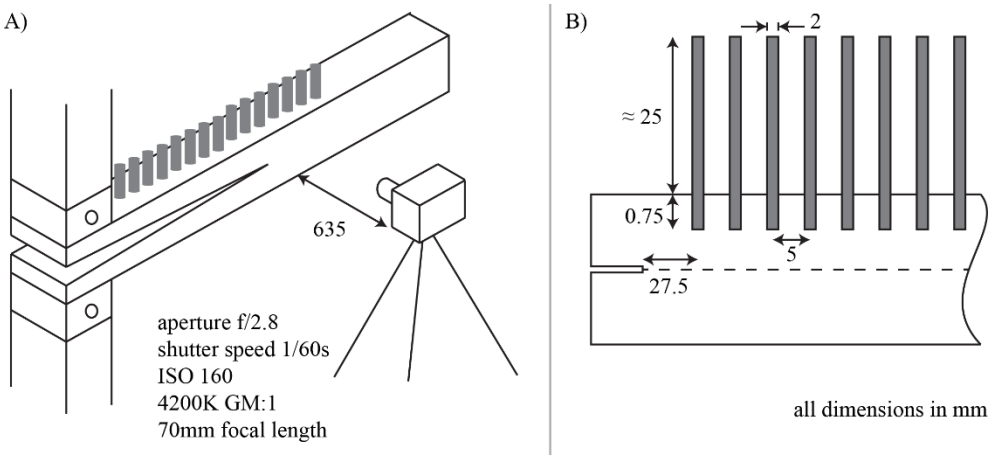

Figure 5-3 A) Schematic representation of image capture set up for DCB curvature analysis. B) Detailed view of the pins which are inserted one quarter of the total thickness into the specimen (0.75 mm). Note, the first pin is 27.5 mm from the start of the pre-crack and the diagram is not to scale.

5.2.4 Image processing

The rotation of each pin in the images is tracked and the angle of each pin determined which provides the slope at each point. The image processing is completed in stages as outlined below and shown in Figure 5-4. Matlab (version 2020a, Mathworks UK) is used for all image processing and the functions used are listed with each step where applicable.

i. The image is cropped to only include the pins using the same cropping limits for all images.
ii. Thresholds were applied to each of the red, green, and blue channels to create a binarized image of the beam and pins with the background removed.
iii. As the binarized image contained noise, a hole fill function is run to fill in any pixels which are surrounded by pixels of the opposite value (using `bwcompconn`).
iv. A quadrilateral mask is created above the beam (for each image) and used to identify the pins.
v. Each pin is identified as a separate region (using `bwlabel`).

vi. In each labelled region/pin, the orientation of the region is recorded (using `regionprops`). The orientation is shown as a red line in Figure 5-4(vi) and defined as the angle between the major axis of an ellipse that has the same second moment of inertia as the region in question and a horizontal line.

vii. To account for Rigid Body Motion (RBM) of the beam relative to the camera, the orientation of the uncracked end of the specimen is determined. A mask is used on the uncracked region shown in red in Figure 5-4(vi) and the orientation is determined using the same method as for the pins

Further analysis of the data is discussed below in Section 5.3.2.

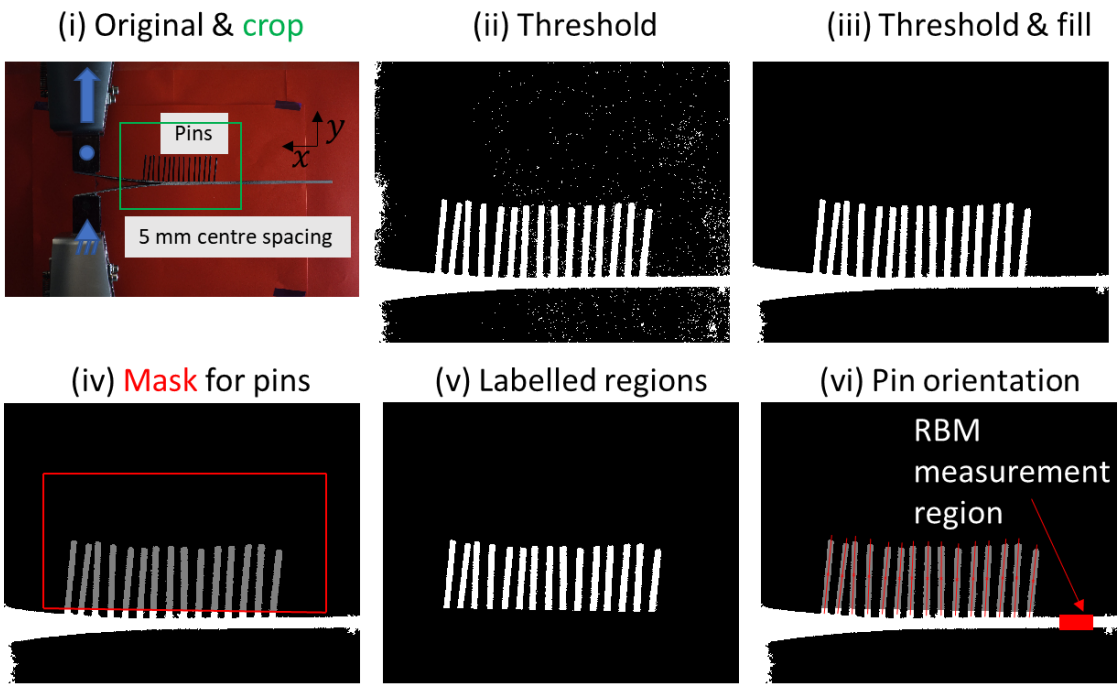

Figure 5-4 Stages of image processing (shown for frame 500 of 907). (i) The original image with the cropped region. (ii) the cropped image binarized based on RGB thresholds and (iii) the binarized image after a hole fill is completed. (iv) the mask used to separate the beams and pins for this frame, (v) the isolated pins, and (vi) the pins with the measured orientation overlaid. The region in red on the right of the image is used to account for rigid body motion by measuring the slope of the bottom and top edge (identified as a column of at least 5 pixels) of the beam.

5.2.5 Simulations

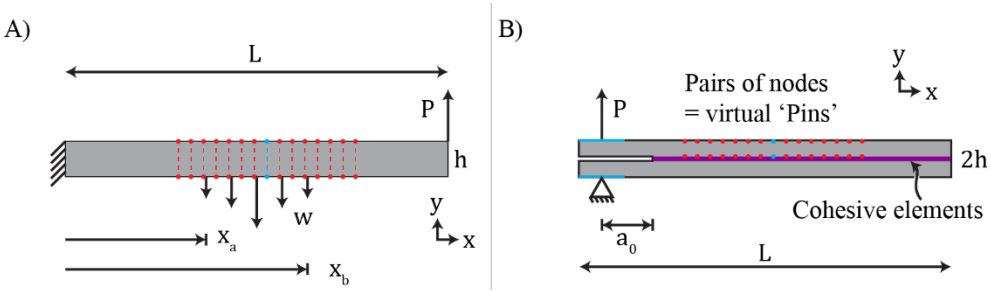

Figure 5-5 A) Finite element model of a cantilever beam subject to a distributed load ω between x_a and x_b and a point load P at the tip. Fifteen pairs of nodes on the beam are identified and used to track discrete rotation similar to the pins in the modified DCB methodology. B) Finite element model of a DCB specimen. Pairs of nodes are used to track discrete rotation. Cohesive elements, governed by a traction-separation law, are used to model the interfacial behaviour as the crack propagates.

Two finite element models are created and analysed using Abaqus 2019 (Dassault Systemes, RI, USA). A DCB model (Figure 5-5B) is created similar to those used in Chapter 3 with cohesive elements used to capture the delamination. In the DCB model, 15 virtual pins are created by tracking the deformed coordinates of 15 pairs of nodes as shown. The slope of the beam at each virtual pin can be determined from the slope of line connecting each pair.

In the second model, a cantilever beam is subjected to an end load a distributed load which varies between x_a and x_b as follows (and as shown in Figure 5-5A):

$$\omega(x) = \begin{cases} -\frac{P}{4} = -2.5N/mm, & 50 \geq x < 51 \; and \; 59 \geq x < 60 \\ -\frac{P}{2} = -5\,N/mm, & 51 \geq x < 52 \; and \; 58 \geq x < 59 \\ -\frac{3P}{4} = -7.5N/mm, & 52 \geq x < 53 \; and \; 57 \geq x < 58 \\ -P = -10N/mm, & 53 \geq x < 57 \\ 0, & otherwise \end{cases} \quad 5.3$$

5.3 Results

5.3.1 DCB results

Here, the results of the experiments outlined in Table 5-1 are presented. For the DCB experiments, the results (shown in Figure 5-6) consist of load versus

load-line displacement and fracture resistance curves (R-curves). Only the loading sections of the curve are used to calculate the R-curve (i.e., the load-line displacement is monotonically increasing). For the LET material, the toughness immediately reaches a steady state value at $300\ \mathrm{J/m^2}$. For the HET material, the initial toughness is $\approx 450\ \mathrm{J/m^2}$ and increases to a plateau value of $\approx 650\ \mathrm{J/m^2}$ over a crack growth of $\Delta a_{ss} = 50\ \mathrm{mm}$. Using the methods described in Chapter 3, a tri-linear TSL is created for each material and the parameters are given in Table 5-2. Examining the cases where a load reversal or a load reversal and pause were introduced, no difference is seen outside of the unloading/reloading loop (Figure 5-6). In all cases, the behaviour is similar to the monotonically loaded specimen. Hysteresis is seen when the crosshead is reversed and then returned to the original direction of travel (see inset in Figure 5-6C). Investigation of each loop shows no clear trend to suggest that the hysteresis is due to a material effect; instead, the energy loss is attributed to losses in the testing set up (e.g., friction at the loading blocks). Note that the crack length used is determined from the compliance of the specimen as described above; comparisons with optical measurements are included in Figure 5-7. The compliance method underestimates the crack length by approximately 10%. The optical measurements could be used to calibrate the compliance-based value – however, this step has not been taken here as the crack length is not critical to the majority of the analysis performed here.

Table 5-2 Traction separation law parameters for *LET* and *HET* materials using the method outlined in chapter 3 on the R-curves presented in Figure 5-6B

	$\boldsymbol{\sigma_{int}}$ (MPa)	$\boldsymbol{\sigma_{ext}}$ (MPa)	$\boldsymbol{\delta_e}$ (mm)	$\boldsymbol{\delta_{int}}$ (mm)	$\boldsymbol{\delta_f}$ (mm)	$\boldsymbol{G_{int}}$ (J/m^2)	$\boldsymbol{G_{ext}}$ (J/m^2)	$\boldsymbol{G_0}$ (J/m^2)
LET	6	0	0.05	0.1	0.1	300	0	300
HET	9	0.0333	0.05	0.1	11.9	450	200	650

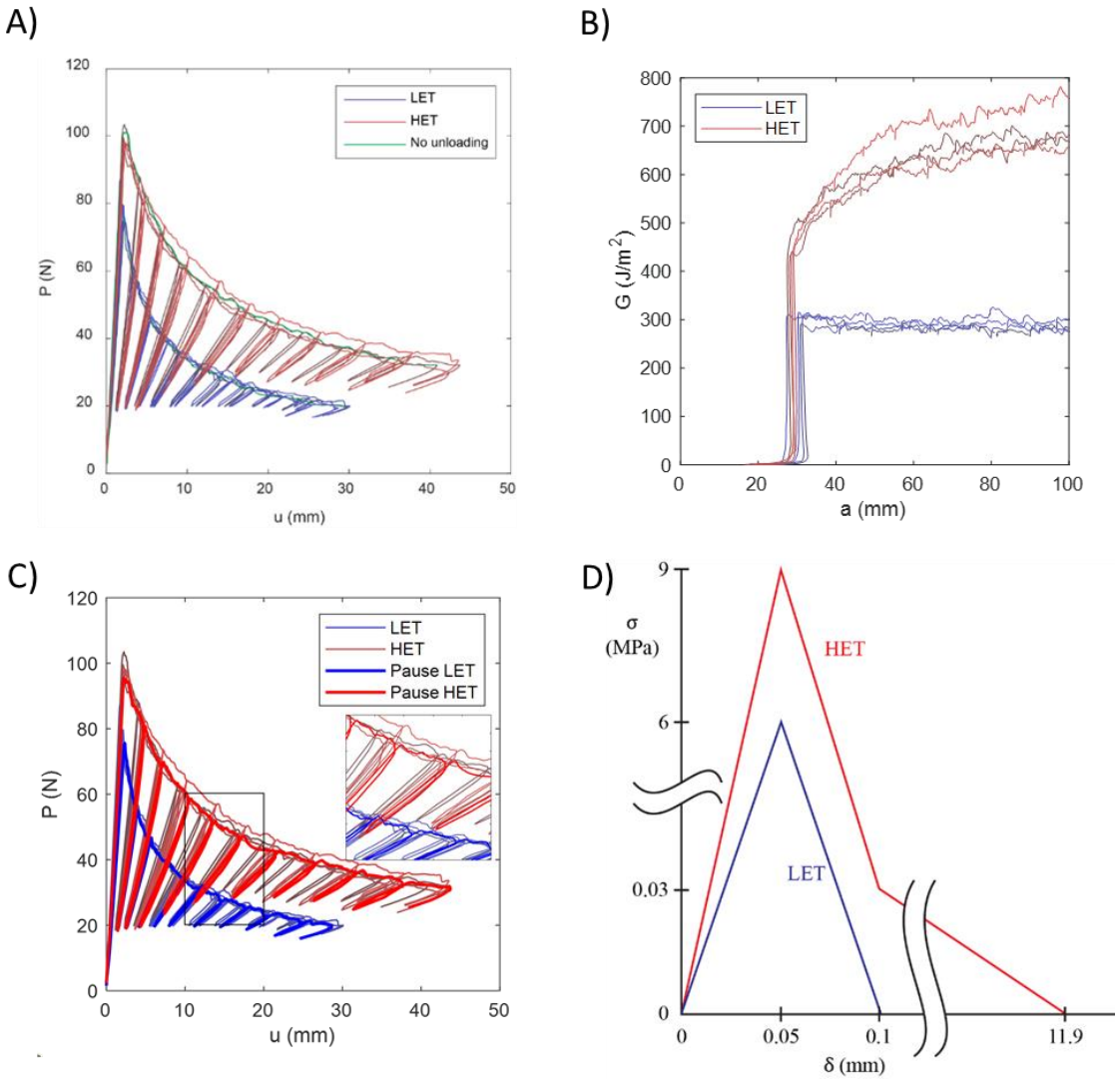

Figure 5-6 A) A comparison of the load versus load-line displacement for DCB experiments using the *LET* and *HET* materials using the *Load/unload* pattern and the *Load through* pattern showing that unloading does not affect macroscopic response and B) resulting R-curves using the compliance calibration method. C) load versus load-line displacement with the response of the *LET* and *HET* materials using the *Pause* pattern overlaid with heavier line weights. D) Tri-linear traction-separation laws based on the average response of the *LET* and *HET* materials.

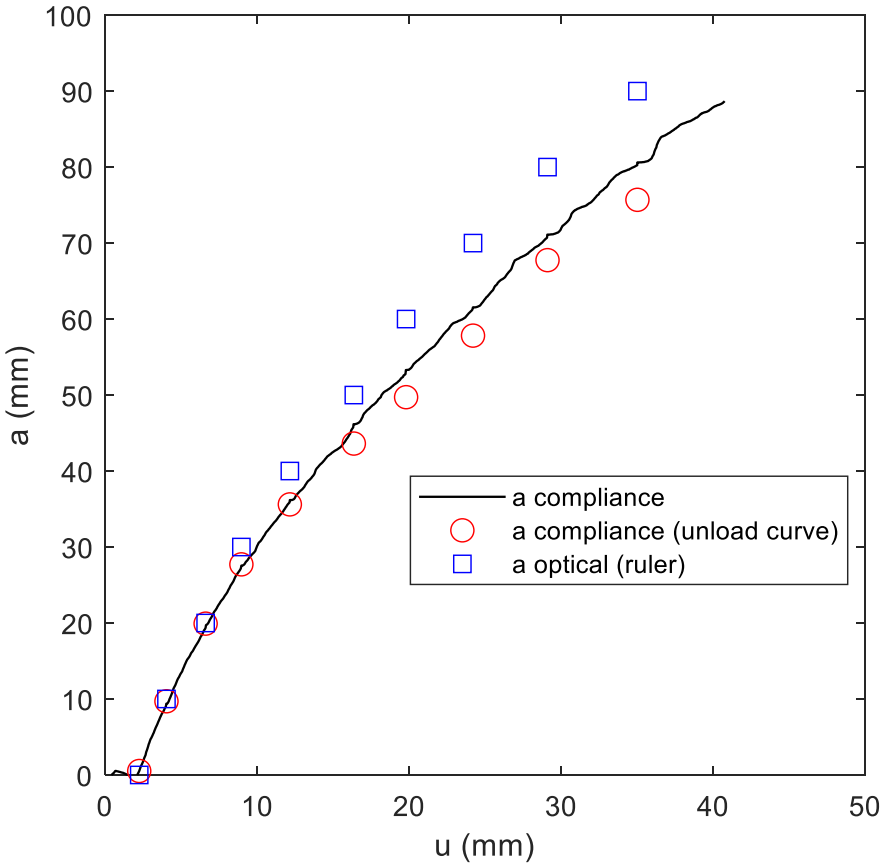

Figure 5-7 Comparision between the optically measured crack length (blue squares) and the computed values using the compliance method. The compliance was also directly measured from the unloading portion of the test (red circles).

5.3.2 Modified DCB results: measuring discrete rotation using evenly spaced pins

5.3.2.1 Imaged based beam slope

Using the methods described in Section 5.2.3, the change in slope of the beam at each pin location θ_{orig} is plotted for each image (i.e., as a function of time) in Figure 5-8A. The initial rotation of each pin is taken as a reference value and taken into account ($\theta_i = \theta_i - \theta_{i,t=0}$) as the change in angle (from the initial position) is the desired quantity (not the current value). The slope after rigid body motion is accounted for ($\theta = \theta_{orig} - \theta_{RBM}$) is shown in Figure 5-8B. The noise in the data is reduced by taking a five-frame moving average (Figure 5-8C). As the test included the unloading regimes discussed in Section 5.2.2, a subset of the frames is taken to correspond to

monotonically increasing crosshead displacement (Figure 5-8D). The propagation of the crack tip can be seen whereby each pin remains at $\theta = 0$ until the crack is reached and θ increases.

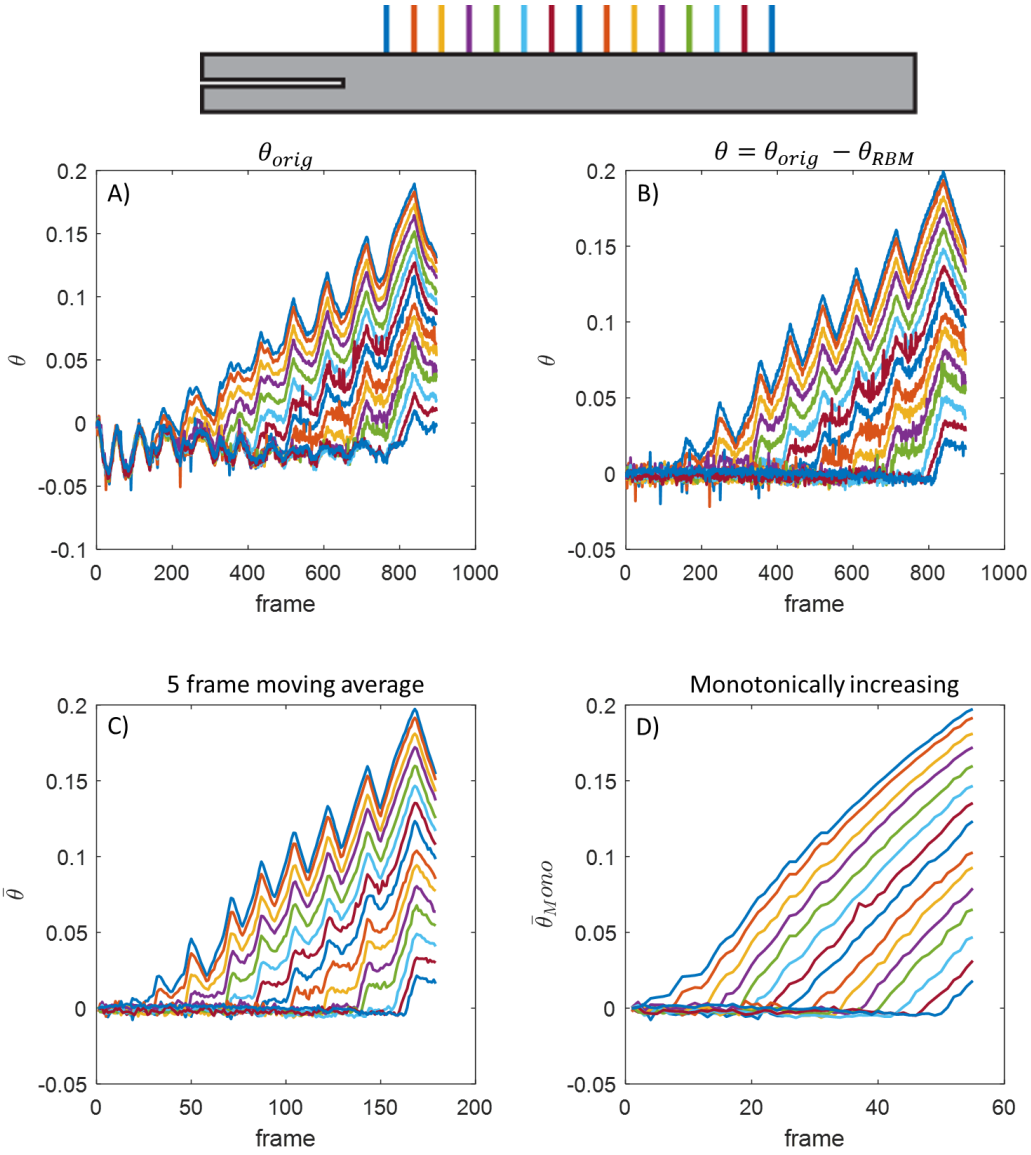

Figure 5-8 Processing θ from measured values to monotonically increasing values. A) the measured change in rotation from the initial position for each frame θ. B) the measured change in rotation for each frame minus the rotation of the free end of the DCB specimen (shown in Figure 5-4(vi)), accounting for rigid body motion. C) $\bar{\theta}$ is the average value of $\theta - \theta_{RBM}$ over five frames and D) $\bar{\theta}$ using only values such that $\bar{\theta}_i > \bar{\theta}_{i-1}$ where i denotes the frame number.

5.3.2.2 Bridging tractions

The beam displacement y, beam curvature κ, bending moment M, shear load V and interfacial traction ω are determined from the array of beam slopes (a slope value θ is available for each pin and frame (which

corresponds to time)). Euler-Bernoulli beam bending is assumed and the integrals and derivatives of θ with respect to x are used to determine each quantity using the following equations (E and I are the Young's modulus and second moment of area, respectively):

$$\theta = \frac{dy}{dx} \tag{5.4}$$

$$\kappa = \frac{d\theta}{dx} = \frac{d^2y}{dx^2} = \frac{M}{EI} \tag{5.5}$$

$$V = \frac{dM}{dx} = EI\frac{d^3y}{dx^3} \tag{5.6}$$

$$-\omega = \frac{dV}{dx} = EI\frac{d^4y}{dx^4} \tag{5.7}$$

$$y = \int \theta \, dx \tag{5.8}$$

Two methods are used to perform these operations: (i) using the discrete values and (ii) using a polynomial fit to the 15 values of θ. For the first method, a central difference is used to calculate the derivatives and the trapezoidal method is used calculate the integrals. To plot traction ω against separation, an average of the displacement at two points is used to calculate the displacement at the midpoint. Note that there is one fewer value after each operation and only twelve values are shown for ω. The integration constant is found by noting that $y = 0$ at the crack tip. Figure 5-9 shows these discrete values for two sample frames. As each derivative is taken, the variation from pin-to-pin increases substantially and the plot of σ ($\sigma = \omega/b$) vs δ shows no clear trend and, in some cases, unphysical negative tractions are computed.

In the second method, an 8th order polynomial is fit to the values for θ using the `polyfit` function in Matlab which calculates the coefficients of a polynomial that provides the best least-squares fit to θ. The order of the polynomial was chosen such that after taking the derivative $d^4y/dx^4 = d^3\theta/dx^3$, the function would still be capable of fitting the arbitrary form of the TSL observed in Chapter 4. A higher order was not chosen as even though

there were 15 pins, each pin was not always in a region where tractions were evident and fitting to a higher order polynomial may give unsound results. The order of the polynomial is discussed further below. The derivatives and integrals were evaluated by using the fit polynomial coefficients.

Figure 5-9 shows these polynomials overlaid over the discrete values and the polynomials are evaluated every 1 mm along the *x*-axis. The polynomial is also plotted within pins 3-13 (heavy magenta lines) to show the regions where there is a higher confidence in the polynomial fit. In the earlier frame shown, the traction vs separation plot shows tractions from 0 to 0.5 mm separation whereas for the later frame, tractions are computed over a different range. For the final frames, tractions are not computed for small separations; therefore, to understand the traction separation behaviour, it is necessary to consider all of the frames together.

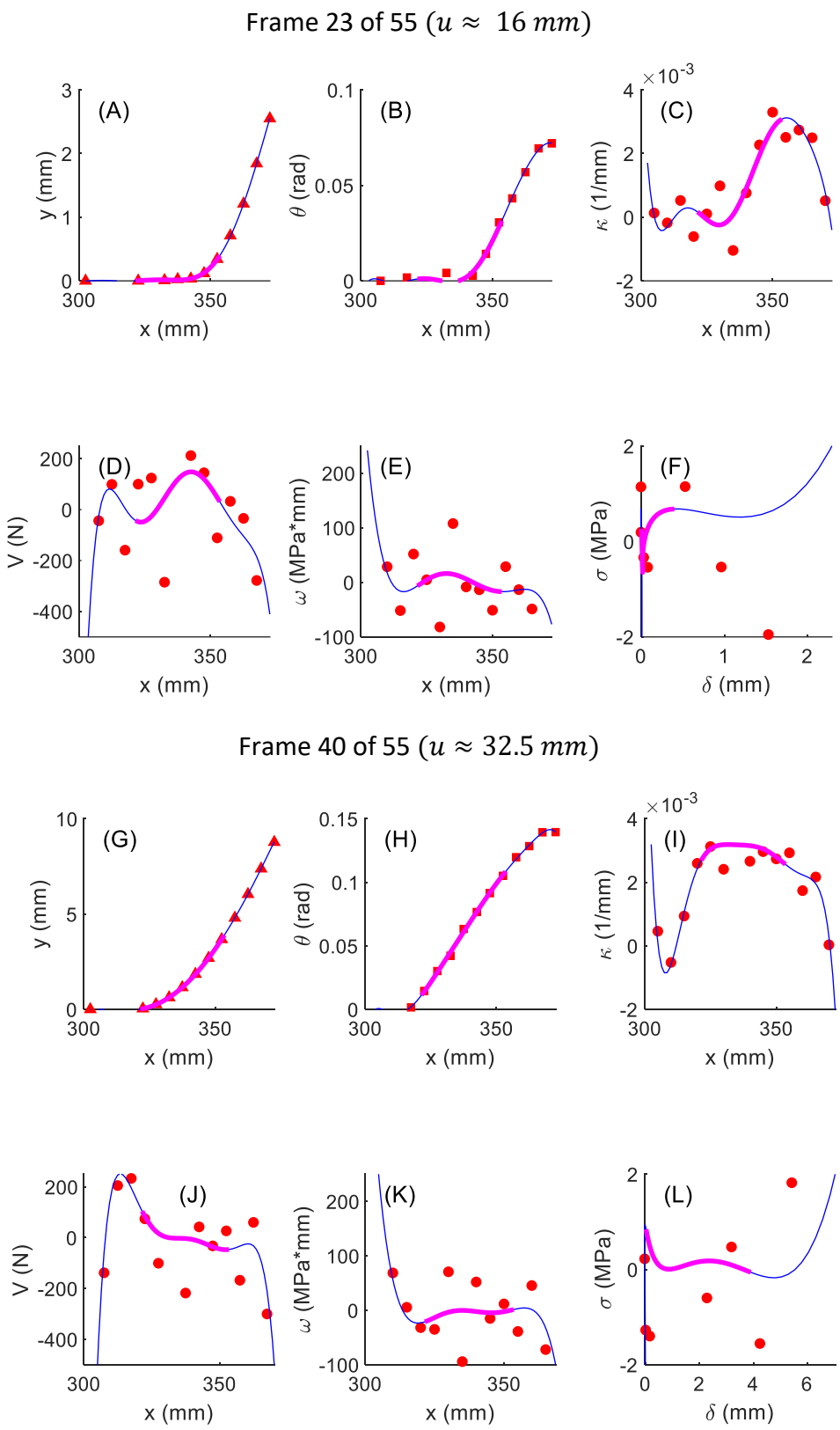

Figure 5-9 Comparison of frames showing $y, \theta, \kappa\ (\propto M), V, \omega$ along the beam (A-E, G-K) and the derived TSL (F, L) for two different frames. The top frame and bottom frame correspond to displacements $u = 16\ mm$ and $u = 32.5\ mm$, respectively. The red crosses denote measured values and discrete differentiation/integration of that data. The blue line denotes the polynomial fitted to θ and differentiation/integration of that function. The magenta data is also polynomial data plotted inside the two outermost pins.

Figure 5-10 shows the TSL using the polynomial method from each frame plotted on the same axis. Note that the plot only includes the region highlighted in magenta in Figure 5-9 for each frame. While there is not clear agreement between all the frames, clear trends are visible. To further explore these trends, a heatmap is created whereby the pixel intensity is related to the number of frames predicting that value of traction for each separation. Each pixel corresponds to $d\sigma = 0.12\ MPa$ and $d\delta = 0.12\ mm$. The same trends are evident in this heatmap; it is clear there is an initial peak at (i) followed by a trough at (ii) and a secondary peak at (iii). The value of stress in the intrinsic region is substantially below that suggested by the traditional methods which suggested a maximum traction of $\approx 9\ \mathrm{MPa}$ for the intrinsic region. The maximum separation is comparable with $11\ \mathrm{mm}$ for the tri-linear approximation and $10\ \mathrm{mm}$ for this method. For comparison, the tractions computed using the discrete method are also shown; however, the issues seen in the frames above are evident in the other frames also (Figure 5-9C).

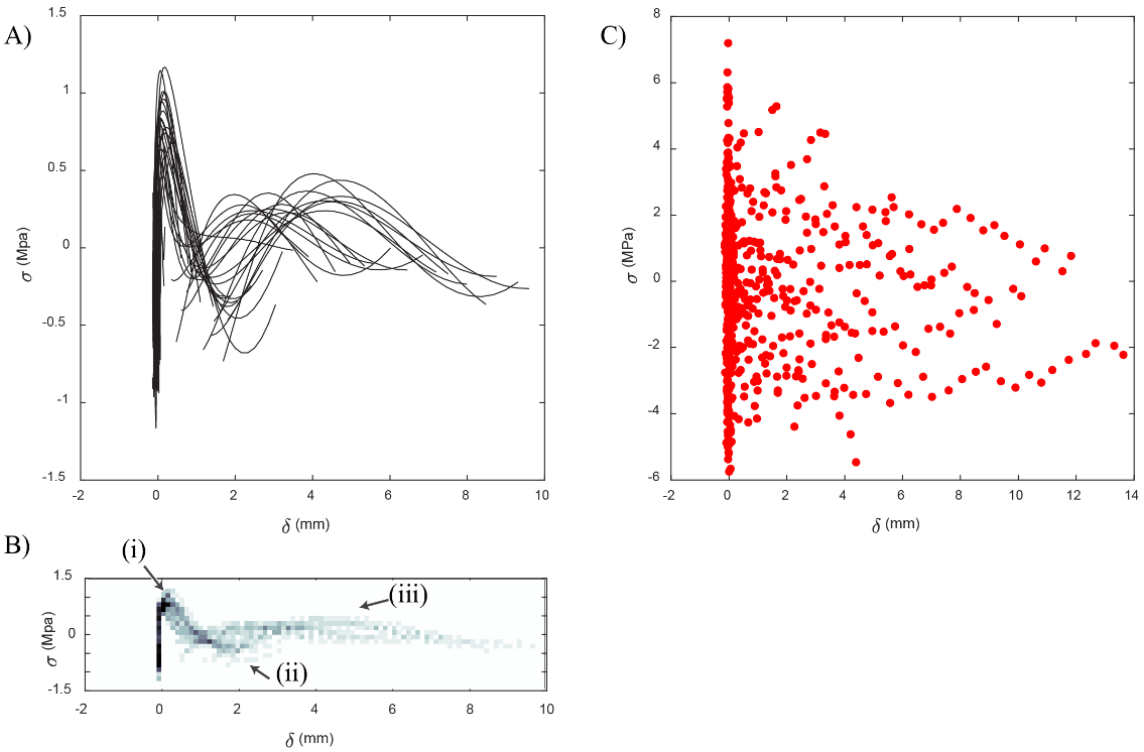

Figure 5-10 A) Traction separation laws obtained from each frame of the experiment overlaid. The data is taken from inside the outermost pins to decrease the noise in the image. B) A heatmap is also provided in which the pixels are shaded in accordance with how many traction-separation curves pass through a given pixel. C) the traction – separation values derived from the discrete pin values.

5.4 Verification & Validation of the differentiation and integration techniques using finite element

To establish credibility in the method used above, two activities are performed. First, a test case is created using a known set of tractions applied to a cantilever beam (as described in section 5.2.5). In the second, a virtual test of a DCB is created using a known traction separation law. In both cases, the "pins" are replicated by tracking pairs of nodes as shown in Figure 5-5.

5.4.1 Known tractions on a cantilever beam

Using the finite element model of a cantilever beam from section 5.2.5, virtual 'pins' measure the rotation of the cantilever beam. A polynomial expression is fit to these discrete rotations in the same manner as above and the same methods are used to compute y, κ, V and ω. A theoretical solution based on Euler-Bernoulli beam bending is used for comparison. For both the

discrete and polynomial approaches, good agreement is seen with the known solution (Figure 5-11).

In the case of the polynomial, the applied traction is not fully recovered, although this improves as the order of the polynomial is increased (Figure 5-11). Although in this case the tractions are constant with respect to separation, the order of the polynomial must be at least 3 times greater than the approximate order for the shape of the traction separation law. As discussed above, the order of the TSL seen in Chapter 4 was 4^{th} order and therefore an 8^{th} order polynomial was used here. Figure 5-11 shows polynomials up to 15^{th} order, however these higher order fits require more data points to be credible. Although the peak is captured more closely with higher orders, the response is more oscillatory in nature and this increases near the outer pins (highlighted with light grey shading). This oscillation, known as Runge's phenomenon, is described by Fornberg and Zuev [14] as a problem of oscillation at the edges of an interval that occurs when using polynomial interpolation with polynomials of high degree over a set of equidistant interpolation points. The choice of 8^{th} order is a compromise between higher fidelity to a TSL and fitting to the 15 data points.

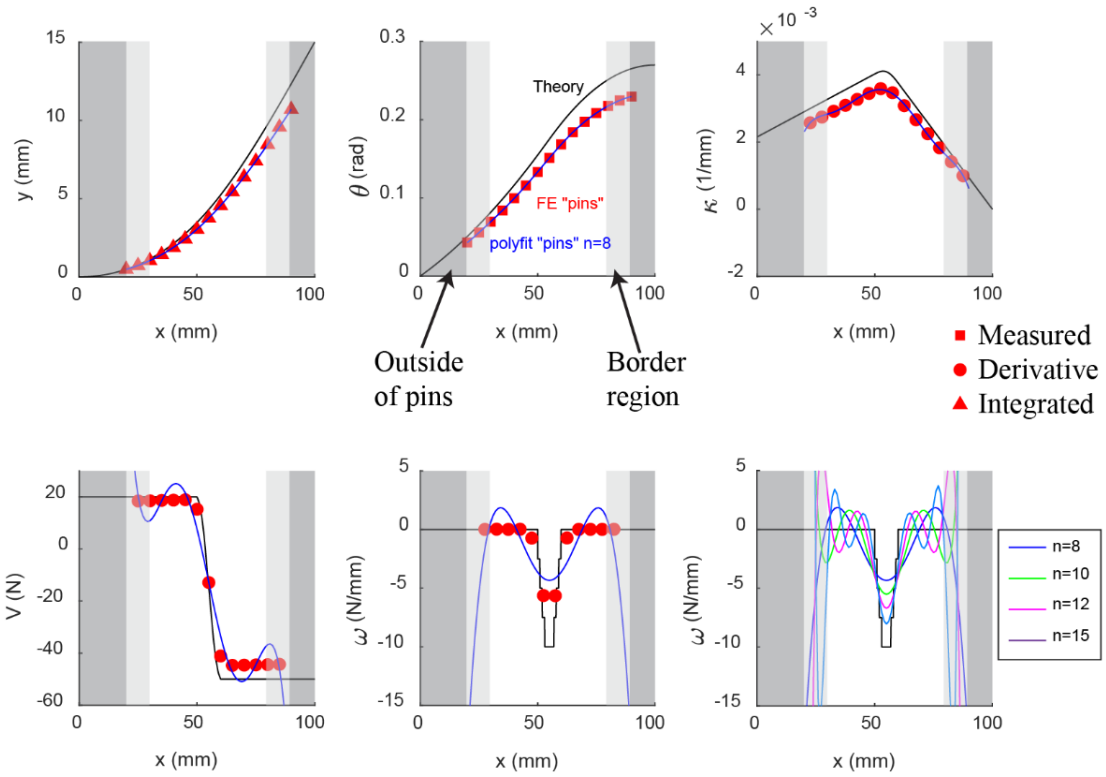

Figure 5-11 Comparison of y, θ, κ, V and ω using a theoretical Matlab model and a finite element cantilever beam simulation (length 100 mm) subject to a distributed load with a maximum value of -10 N/mm, loaded between x = 50 mm to x = 60 mm and subject to an end load of 50 N. Pairs of nodes are used in the FE model to replicate pins as used in a subsequent DCB experiment, the red crosses denote measured values of θ, while squares represent the integrated values of θ and circles represent the derivatives. The blue line represents a polynomial function fit to the measured values of θ and the integrals/derivatives of this polynomial function. The dark shaded region indicates that no pins are present in this section of the beam, while the light shaded region indicates the outer two pins on the beam where the polynomial tends to approach a large value compared to the rest of the pins.

5.4.2 Virtual experiment with known TSL

In the second validation, a known traction-separation law (TSL) is applied in a FE model of a DCB fracture test and the method above is applied without knowledge of the TSL. Two applied interface laws are considered, a trilinear TSL and a piecewise-linear exponential TSL (shown in Figure 5-12). Similar to the experimental method data, each frame results in a traction separation curve which shows a variation from frame to frame. The combined plots of the TSLs for each frame are plotted and in the case of the exponential law, good agreement is seen in terms of the peak and the tractions associated with the intrinsic toughness ($\approx \delta < 0.05$ mm). A heat map using the same approach is also created which makes the comparison clearer. In the case of

the trilinear law, the sharp transition from the intrinsic region to the extrinsic region (at $\delta = 0.01$ mm) is much more difficult to capture. In a real material, such a sharp transition is unlikely, and this virtual experiment is captured well for the case of the exponential methods.

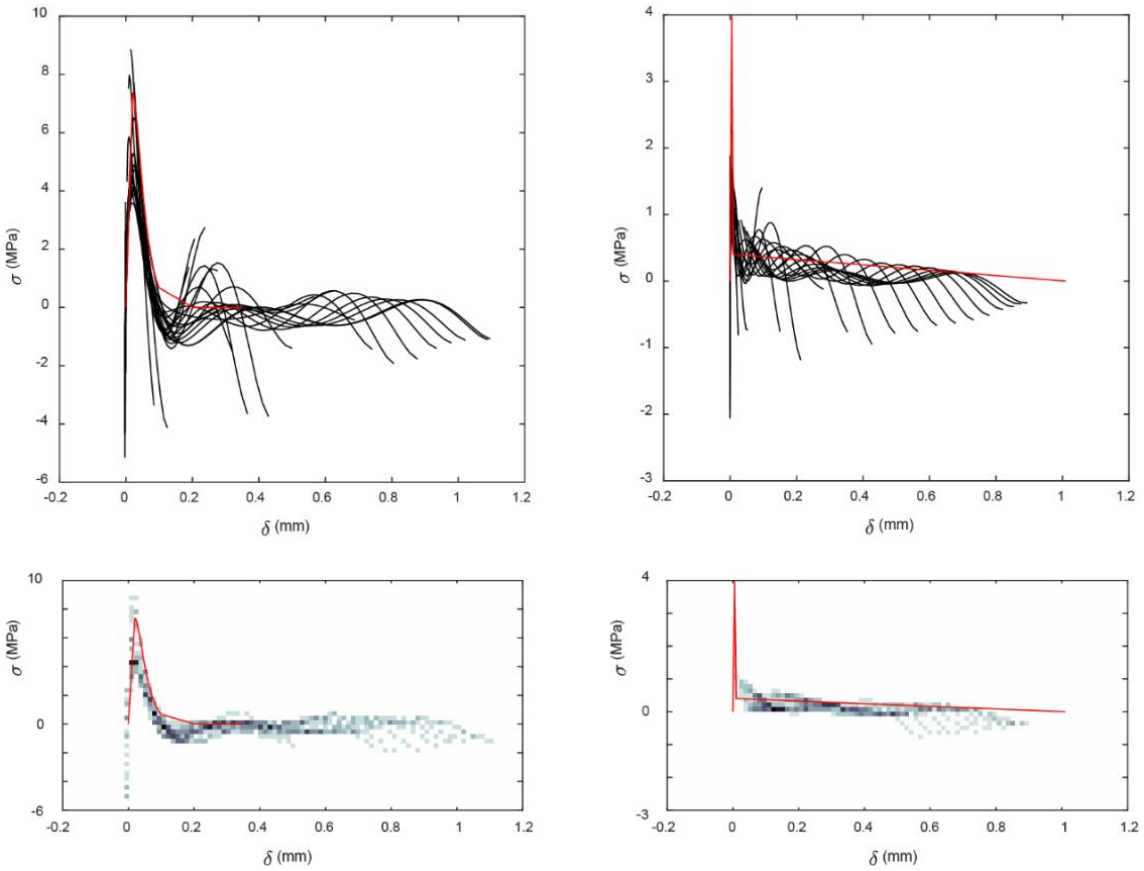

Figure 5-12 Predicted TSL using nodal pairs as pins (black) and applied TSL in the FE model (red). The TSL is treated as an unknown to generate the black lines, and only included for comparison. On the left is an exponential TSL with a final separation value of 0.33 mm and $G = 385\, J/m^2$. On the right is a trilinear TSL with $\sigma_{int} = 4\, MPa$, $\delta_f = 1\, mm$, and $G = 220\, J/m^2$. A heatmap is also provided in which the pixels are shaded according to how many traction-separation curves pass through a given pixel.

5.5 Future perspectives

Although the method described here is an improvement on that seen in Chapter 4 – the experimental set up is much simpler and the issue of the beam not remaining in contact with the roller does not arise, there is room for further improvement. During the experimental work, affixing the pins is difficult and requires complex machining of the specimen. The predicted TSLs show a high degree for variability and while there is substantial support for the second peak observed in Chapter 4, the confidence in this conclusion

is undermined by the variability. Two future approaches are considered, and some initial analysis is performed. First, the displacement of the centre line of one of the beams is exported from the FE simulation to assess whether optical tracking of a beam edge would provide sufficient data. Second, an alternative to the pins is considered.

5.5.1 Image based displacement measurement on a cantilever

The fit of the polynomials above was undermined by the number of data points (15); therefore, here we consider tracking the displacement at every point along one of the beams of the DCB. As it is not possible to track the rotation of these points, the algorithm above is modified to start with y instead of $\theta = dy/dx$, which requires an extra derivative to be taken. The same approach was taken as above in the cantilever beam validation; however, displacement is tracked instead of rotation. Additionally, the displacement of 15 discrete points is recorded and processed similar to the discrete θ values above. Both sets of data are plotted for each quantity in Figure 5-13. Displacement, rotation, and curvature based on the midplane displacement show good agreement with both the known solution and the discrete pins method, however for higher derivatives (i.e., shear and tractions), the agreement is poorer than for the discrete pins. Although the displacement data is exported from the finite element method with six significant figures, the computed values are incorrect due to the small value of dx associated with the element size.

The effect of the data precision on the accuracy of the discrete pins is investigated by changing the number of significant digits in the exported data. By rounding to fewer digits, the computed values are seen to disagree with the known solution for less than three significant digits. As the displacements are in the order of tens of mm and the region of interest is at least $50\ \mathrm{mm}$ wide, then three significant digits corresponds to $0.1\ \mathrm{mm}$ (note that each beam in the DCB is $1.5\ \mathrm{mm}$ in height). Therefore, optical method would need at least to be able to resolve displacement in tens to hundreds

of microns. In the experiments above, the pixel size was approximately 60 microns, and a smaller field of view could be used to increase the resolution.

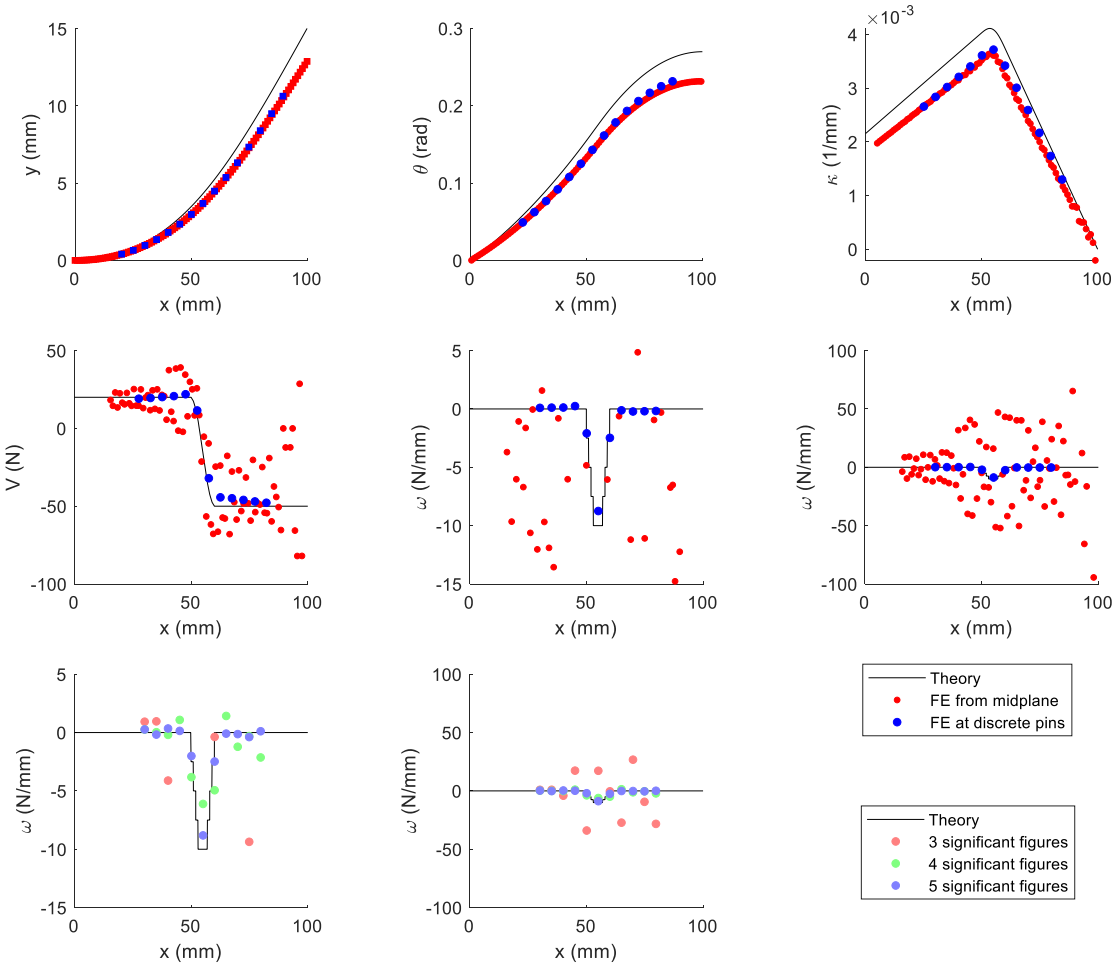

Figure 5-13 Comparison of y, θ, κ, V and ω from a theoretical Matlab model and a finite element cantilever beam simulation (length 100 mm) subject to a distributed load with a maximum value of -10 N/mm between x = 50 mm to x = 60 mm and an end load of 50 N. The beam has a Young's modulus of $E = 100\ GPa$. Solid squares represent the measured values of displacement, while solid circles represent differentiated values. The bottom row shows the effect of the level of precision included in the differentiation. Here y is rounded to 3-5 significant figures prior to differentiation to resemble the precision of experimental measurements.

5.5.2 Experimental approaches

Based on the previous observations, a modified experimental method is proposed. The displacement tracking of a continuous line (the centre line in the FE simulation) was not shown to be feasible; therefore, image-based tracking of the edge of the beam or of a feature painted or otherwise added to the beam is not pursued further. The tracking of discrete points showed the most promise, therefore a new method to continue tracking discrete

points, but without the issues related to the pins is presented. So called "Secchi" discs are commonly used in impact crash tests and water depth measurements [15] and can provide an easily identifiable feature to track in the image. These discs consist of a pattern based on using alternate colours (yellow and black) in alternating quadrants of the circle, as shown in Figure 5-14. The discs allow for tracking of both the rotation and the displacement (on a plane orthogonal to the camera view) of each point.

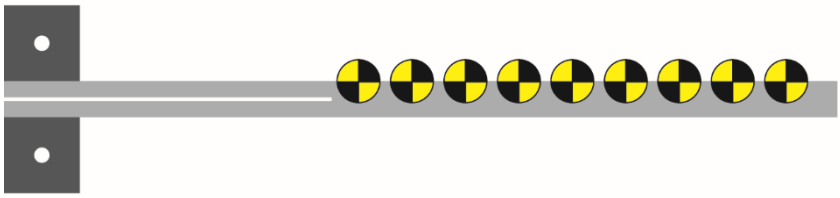

Figure 5-14 Concept for improved test specimen using Secchi disks to measure rotation in DCB curvature analysis. Dimensions of specimen and disks excluded as these may be dictated by machining parameters.

For a fracture test that has reached a steady state value, a point adjacent to the original crack tip must have undergone a separation equal to the steady state crack length Δa_{ss} to fully develop the fibre bridging. The spacing of the Secchi discs should be determined based on the number of desired discs over this length. Table 5-3 shows the crack growth required for different specimen geometries based on the TSL parameters identified for the HET material. Note that overall specimen length should be increased to accommodate the required crack propagation. These parameters (most importantly δ_{ext}) can be determined from a standard DCB test. The relationship between δ_{ext} and Δa_{ss} is further discussed in Chapter 3. As the minimum order of the polynomial required is 7th order, at minimum 7 discs would be required to fit the polynomial; however, as discussed above, a larger number of data points will improve the fit. For the material thickness used in the tests above, the discs may be prohibitively small, and a larger specimen would be required.

Table 5-3 Relationship between beam thickness h and the steady state crack length Δa_{ss} (required to achieve a steady state distribution of fibre bridging) and hence the Secchi disks spacing (assuming 7 or 14 disks are used in the experiment). The beam thickness used in the first iteration of this experiment ($2h = 3\ mm$) is shown in bold. The maximum allowable separation is fixed at 12 mm and Young's modulus of 100 GPa, making this table applicable to the *HET* material.

h	$\boldsymbol{\Delta a_{ss}}$	**Secchi disk spacing (mm)**	
		7 disks	14 disks
1	46.4159	7.7360	3.5705
1.5	**69.6238**	**11.6040**	**5.3557**
3	139.2477	23.2079	10.7114
6	278.4953	46.4159	21.4227

5.6 Concluding remarks

In the present chapter, a new method for investigating the traction separation law of a laminate fibre composite is introduced. This method is an adaptation of the ASTM standard method and does not require additional fixtures (as was the case in Chapter 4). By tracking the rotation of pins embedded in the specimen, the rotation and hence the curvature, shear, and surface tractions are determined along the beam of the DCB. By comparing the results at numerous different crack lengths, the traction separation relationship can be explored over the full range of separations. Although this method is an improvement on the work presented in Chapter 4, the variation from frame to frame in the TSL undermines credibility in the model. Through validation steps taken, future avenues are identified to improve the accuracy of the method, while following the same basic principles. As was seen in Chapter 4, analysing the difference in traction-separation behaviour over the full range of separations is important to understanding the effect of manufacturing changes on the toughness of the laminate composites. The work presented in this chapter develops a test platform to quickly complete these tests.

The validation and verification steps performed also provide interesting perspectives for future modifications to the test. Possible improvements are

suggested which would allow this method to provide deep insight into material behaviour while being possible to complete quickly with minimal changes to standard test methods. The processing techniques developed here can be quickly adapted to any future iterations.

5.7 References

[1] Breslauer E, Troczynski T. Determination of the energy dissipated during peel testing. Mater Sci Eng A 2001;302:168–80. https://doi.org/10.1016/S0921-5093(00)01370-8.

[2] Sørensen BF, Horsewell A, Jørgensen O, Kumar AN, Engbaek P. Fracture Resistance Measurement Method for in situ Observation of Crack Mechanisms. J Am Ceram Soc 1998;81:661–9. https://doi.org/10.1111/j.1151-2916.1998.tb02387.x.

[3] Sørensen BF, Jacobsen TK. Determination of cohesive laws by the J integral approach. Eng Fract Mech 2003;70:1841–58. https://doi.org/10.1016/S0013-7944(03)00127-9.

[4] Majano-Majano A, Lara-Bocanegra AJ, Xavier J, Morais J. Measuring the cohesive law in mode I loading of Eucalyptus globulus. Materials (Basel) 2018;12. https://doi.org/10.3390/ma12010023.

[5] Sills RB, Thouless MD. Cohesive-length scales for damage and toughening mechanisms. Int J Solids Struct 2015. https://doi.org/10.1016/j.ijsolstr.2014.06.010.

[6] Shokrieh MM, Salamat-Talab M, Heidari-Rarani M. Effect of initial crack length on the measured bridging law of unidirectional E-glass/epoxy double cantilever beam specimens. Mater Des 2014;55:605–11. https://doi.org/10.1016/j.matdes.2013.09.064.

[7] Betterman LR, Ouyang C, Shah SP. Fiber-matrix interaction in microfiber-reinforced mortar. Adv Cem Based Mater 1995;2:53–61. https://doi.org/10.1016/1065-7355(95)90025-X.

[8] Sørensen BF. Cohesive law and notch sensitivity of adhesive joints. Acta Mater 2002;50:1053–61. https://doi.org/10.1016/S1359-6454(01)00404-9.

[9] Zhu Y, Liechti KM, Ravi-Chandar K. Direct extraction of rate-dependent traction–separation laws for polyurea/steel interfaces. Int J Solids Struct 2009;46:31–51. https://doi.org/10.1016/j.ijsolstr.2008.08.019.

[10] Jacobsen TK, Sørensen BF. Mode I intra-laminar crack growth in composites - modelling of R-curves from measured bridging laws. Compos Part A Appl Sci Manuf 2001;32:1–11. https://doi.org/10.1016/S1359-835X(00)00139-1.

[11] Sørensen BF, Jacobsen TK. Large-scale bridging in composites: R-curves and bridging laws. Compos Part A Appl Sci Manuf 1998;29:1443–51. https://doi.org/10.1016/S1359-835X(98)00025-6.

[12] Sørensen BF, Gamstedt EK, Østergaard RC, Goutianos S. Micromechanical model of cross-over fibre bridging – Prediction of mixed mode bridging laws. Mech Mater 2008;40:220–34. https://doi.org/10.1016/j.mechmat.2007.07.007.

[13] ASTM. Standard Test Method for Mode I Interlaminar Fracture Toughness of Unidirectional Fiber-Reinforced Polymer Matrix Composites 1 2013. https://doi.org/10.1520/D5528-13.

[14] Fornberg B, Zuev J. The Runge phenomenon and spatially variable shape parameters in RBF interpolation. Comput Math with Appl 2007;54:379–98. https://doi.org/10.1016/j.camwa.2007.01.028.

[15] Hou W, Lee Z, Weidemann AD. Why does the Secchi disk disappear? An imaging perspective. Opt Express 2007;15:2791. https://doi.org/10.1364/oe.15.002791.

Chapter 6. Concluding remarks and future perspectives

Fibre bridging, an extrinsic toughening mechanism, is challenging to accurately capture in interface models; the tractions generated by fibre bridging are not fully understood. It is common for an experimental result to be replicated in-silico with a small set of parameters, but the sensitivity of the computational parameters is rarely examined. This leads to subjectivity in the choice of interface parameters. The methods described in this thesis allow for (i) non-subjective choice of interface parameters based on experimental response (which is valuable in an industry setting); (ii) comparison of material properties at large separations (this highlights how differences in manufacturing processes or material (fibre/resin) choices affect macroscopic properties; (iii) development of new methods or modification of a standardised test methods to generate traction-separation data.

Fracture toughness in fibre reinforced composites is typically characterised using a DCB (Double Cantilever Beam) test. In Chapter 3, a systematic parameter study was conducted on the traction separation law used in a finite element model of the DCB fracture test. This exploration yielded a robust method of defining a trilinear traction separation law for materials experiencing significant extrinsic toughening based on experimental observations of the standardised ASTM DCB fracture test [2]. The key features of an experimentally determined R-curve, along with specimen dependent properties such as thickness and modulus, are used to determine the interface law. It was found that the method outlined in this chapter accurately captures the key features of experimentally measured R-curves (initial toughness, final/plateau toughness, and crack length required to reach the plateau value). Where further details of the shape of the R-curve are not needed, this method balances ease of use with accuracy and robustness of the results.

In the cases where more detail of the TSL is required, other methods can be used. In the existing literature, the J-integral is typically used to determine the traction separation law [3]. The J-integral is typically restricted to cases where end moments are applied to the cantilever arms of the specimen and can require assumptions around the form of the TSL; for example, Jacobsen et al. [3] assume tractions are of the form $\sigma \propto (n+1)\delta^n$. Such test methods and analyses are not always practical to conduct in an industry setting. The methods outlined in this thesis are much simpler to implement in an industrial setting and can be applied to simple measurements (key R-curve features, specimen height, specimen modulus). Particularly, the interpretation of standard (end loaded) DCB results is readily implementable in industry.

In Chapter 4, a novel fracture test method capable of directly measuring fracture toughness is discussed. This method (known as the DRAFT method) uses rolling arcs to apply a constant curvature to the test specimen, i.e., the specimen conforms to the rolling arc curvature. The analysis of this fracture test presented in Chapter 4 establishes the direct relationships between fracture energy, delamination length, and applied load. In this method, the delamination length is equivalent to the applied displacement assuming the specimen completely conforms to the rolling arc surface. The theoretical treatment shows how the tractions can subsequently be determined. This method proved effective at capturing the extrinsic behaviour of the material while allowing a piecewise linear traction separation law to be generated from the measured response.

The material tested in Chapter 4 exhibits a second peak in the traction separation response of the material. It is difficult to definitively state what causes this secondary peak. As there are two peaks in the response, there are likely two mechanisms for toughening in the material – the first being responsible for the initial peak related to intrinsic toughening and the other mechanism being responsible for the secondary peak related to extrinsic mechanisms. As shown in Chapter 4, changes at the interface ply resulted in

a change only in the secondary peak. Possible explanations for this behaviour include: (i) Delayed onset of tension in fibres that were not fully extended when the layup was impregnated with resin; (ii) crack propagation causing bunching of fibres, which in turn increases the traction exerted by the bunch of fibres; (iii) an excessive peel of fibres from the debonding surfaces causing slack in the fibres, the slack is then removed as the crack propagates which increases the tensile load on the fibre and the traction exerted at the interface.

Comparing the DRAFT method to the more established DCB fracture test method, it was found that in most cases the DCB method is sufficient to capture the key features of the crack growth resistance curve. However, the shape of the R-curve (and resulting traction-separation law) can be explored using the DRAFT rig. Compared to the DCB method, the DRAFT method provides additional detail about the shape of the transitional response in an R-curve before a steady state turnover of bridging fibres has been achieved. An important point to consider with the DRAFT rig is that the theoretical framework assumes that the beam fully conforms to the rolling arc radius. This assumption becomes less valid as the strain energy of the specimen increases. A recommendation of this chapter is to simulate the test using values approximated from a DCB test to assess the validity of using the DRAFT method. Modifications to the test method may improve the results (e.g., changing the roller radius); however, whether these are performed is in the context of the effort and cost required.

Considering the data and simulations across the entire thesis, it is clear that the DCB method should be used to capture the intrinsic response of the material. Although the DRAFT method can readily capture the extrinsic behaviour; there is no clear sudden increase in fracture toughness that would be associated with the intrinsic behaviour of the material. The tractions predicted by this approach do not reach the maximum values expected; instead, a broader peak is observed in the TSL. The sharp change

in applied load at the beginning of crack propagation in the DCB method can be used to accurately determine the intrinsic toughness.

As the DRAFT method is not directly comparable with existing fracture test data and required a complicated testing procedure, there was a need to develop a method of determining non-linear interfacial laws capable of including a second (or more) peak in traction-separation behaviour (as suggested by the DRAFT method). In a novel experiment, the DCB method was altered to include pins along the specimen which increases the length of the surface normal for image processing (Chapter 5). These pins were used to provide discrete measurement of local rotation along the specimen as the test progresses. This information is used to infer the interface TSL which may be non-linear in nature. The local rotation data is used to infer the TSL based on the fourth order differential relationship between displacement, rotation, curvature, shear force and traction (Euler-Bernoulli theory). However, the accuracy of this method can be improved upon as discussed in Chapter 5.

This modified DCB experiment provided a useful proof of concept and much of the framework is in place for a second iteration of the experiment. A future, second iteration is recommended to improve the resolution of the achieved results by increasing the accuracy of the rotation measurement. Possible improvements to the experimental arrangement include: (i) Changing the pins to quarter shaded Secchi discs. These discs are typically used in impact simulations as their rotation can be easily tracked when completing the image processing. (ii) Increase the length of the test specimen. This would allow more pins or discs to be included along the length of the specimen, increasing the number of data points gathered per frame. The polynomials fit to the rotation were typically sixth order or higher. Ideally, the number of data points gathered should be much greater than the order of the polynomial used to minimise oscillatory behaviour [5].

This thesis has performed an investigation of extrinsic toughening and presented methods to assess material performance and capture the

essential behaviour in simulations (primarily the finite element method). A robust method to determine a minimum set of cohesive properties from the industry standard test methods was developed; this work was also packaged in a format readily usable by industry. Two new methods of more detailed investigation of the cohesive behaviour were analysed. In the first method (the so-called DRAFT method), the investigations revealed that the bridging tractions do not follow the usually assumed trilinear or exponentially decaying form. However, a number of issues undermined full confidence in this method and a second method was developed. In this second approach, a standard DCB approach was modified to measure tractions along the beam. Beam curvature was determined from a series of images and used to calculate the changes in moments and loads along the beam.

The work performed here provides several tools that allows extrinsic toughening mechanisms to be determined in a robust and objective way. The approaches are compatible with standard industry practices and allow computational techniques to be used more effectively in both the analysis and optimisation of materials and in larger scale simulations of applications involving these materials.

6.1 Future perspectives

While this thesis has furthered knowledge of fracture in fibrous materials, it can be improved upon. The methods developed in this thesis have limitations which are discussed in their relevant chapters. The following suggestions for future work could improve the methods in this thesis and possibly develop new methodologies based on the research presented here.

By comparing the DCB and DRAFT methods, it is clear that the DRAFT method can provide a more detail traction separation response at large separations but does not accurately capture the intrinsic behaviour of the material. The DCB method does capture the intrinsic behaviour but produces a simplified extrinsic region of the TSL. To capture the full material response,

both test methods are relevant. However, there is a question as to how to combine the results from each test to a single traction separation law.

The analysis of the DRAFT method highlighted that the specimen does not perfectly conform to the rolling arc surface. Future work could alter the test rig to apply a pretension to the specimen, or another method of ensuring the specimen conforms to the geometry.

The modified DCB experiment in chapter 5 produces non-linear trends in the TSL, but the resolution of the TSL is poor. Possible improvements to this method are discussed in chapter 5. It is suggested that improving the accuracy of the rotation measurement using Secchi disks will improve the resolution of the result. The resolution of the peak will still be difficult to detect with this improvement as there are four differentiation steps in this experiment. It may be the case that some of these differentiation steps can be removed by measuring the curvature, shear, or traction directly (instead of the rotation). The proposed alteration to this experiment (using Secchi disks) is one option to improve the accuracy of the rotation measurement. A laser profilometer is an alternative approach which should yield an accurate rotation measurement at a higher density than the Secchi disks.

Another alternative is to bypass the need for differentiation by measuring the tractions exerted by the fibres directly; here the concept is to insert a transducer into the specimen which measures the force exerted by the fibres. It would also be necessary to use image tracking here to relate the detected force to the separation. If possible, it would be preferable to adhere a sensor to the specimen rather than place it inside the sample as the sample would be more representative of the material. This may be limited by the specimen and transducer/sensor used.

6.2 References

[1] Sills RB, Thouless MD. Cohesive-length scales for damage and toughening mechanisms. Int J Solids Struct 2015. https://doi.org/10.1016/j.ijsolstr.2014.06.010.

[2] ASTM. Standard Test Method for Mode I Interlaminar Fracture Toughness of Unidirectional Fiber-Reinforced Polymer Matrix Composites 1 2013. https://doi.org/10.1520/D5528-13.

[3] Jacobsen TK, Sørensen BF. Mode I intra-laminar crack growth in composites - modelling of R-curves from measured bridging laws. Compos Part A Appl Sci Manuf 2001;32:1–11. https://doi.org/10.1016/S1359-835X(00)00139-1.

[4] Dávila CG, Rose CA, Camanho PP. A procedure for superposing linear cohesive laws to represent multiple damage mechanisms in the fracture of composites. Int J Fract 2009;158:211–23. https://doi.org/10.1007/s10704-009-9366-z.

[5] Fornberg B, Zuev J. The Runge phenomenon and spatially variable shape parameters in RBF interpolation. Comput Math with Appl 2007;54:379–98. https://doi.org/10.1016/j.camwa.2007.01.028.

Chapter 7. Appendices

7.1 Appendix 1 – Examining the intrinsic region of the traction-separation law

This appendix accompanies Chapter 3, it details an investigation into the relationship between macroscopic Double Cantilever Beam (DCB) behaviour and the traction-separation law (TSL) for a bilinear TSL – i.e., without extrinsic toughening.

In the simplest case, with no fibre bridging, the traction-separation curve is completely defined by the stiffness k_c, maximum traction σ_{int}, and a final separation δ_{int} at which the traction returns to zero. This shape of TSL is commonly used in mode II loading as fibre bridging is motivated by mode I opening [1]. Preliminary work in this study involves a systematic variation of the parameter space associated with the intrinsic region of the TSL, i.e., a law without fibre bridging present. The parameter space is explored in three phases: as shown below. Table 7-1 shows in detail the parameters used and the first column of Figure 7-1 presents the traction-separation laws input into the simulations in the preliminary work of this investigation.

I. The stiffness k_c varies but the traction σ_{int} and failure separation δ_{int} are fixed.

II. The maximum traction σ_{int} is varied. In this case the fracture energy G_{total} is allowed to change (the failure separation is fixed).

    i. The stiffness k_c is fixed, therefore the elastic separation δ_e is variable.

    ii. The elastic separation δ_e is held constant; hence k_c is variable.

III. The maximum traction σ_{int} is varied, for each of the three stiffness values listed above. In this case the fracture energy G_{total} is kept constant. Different shapes of traction-separation laws are examined

including isosceles triangles, scalene triangles, and trapezoids. These laws all have the same fracture energy G_{total} as calculated by the integral $G_{total} = \int \sigma \, \partial\delta$.

Table 7-1 Parameters used in the preliminary investigation into the intrinsic region of traction-separation law. *Analyses where an alternative shape to the bilinear model are used.

		$\boldsymbol{\sigma_{int}}$ $(\mathbf{MPa})$	$\boldsymbol{\delta_e}$ $(\mathbf{mm})$	$\boldsymbol{\delta_{int}}$ $(\mathbf{mm})$	$\boldsymbol{k_c}$ $(\mathbf{MPa/mm})$	$\boldsymbol{G_{total}}$ $(\mathbf{J/m^2})$
I		40	$9x10^{-3}$	$10x10^{-3}$	4444.4	200
		40	$5x10^{-3}$	$10x10^{-3}$	8000	200
		40	$1x10^{-3}$	$10x10^{-3}$	40000	200
II	**(i)**	40	$5x10^{-3}$	$10x10^{-3}$	8000	200
		10	$1.25x10^{-3}$	$10x10^{-3}$	8000	50
		4	$5x10^{-4}$	$10x10^{-3}$	8000	20
	(ii)	10	$5x10^{-3}$	$10x10^{-3}$	2000	50
		4	$5x10^{-3}$	$10x10^{-3}$	800	20
III		40	$5x10^{-3}$	0.01	8000	200
		10	$5x10^{-3}$	0.04	2000	200
		10	$1.25x10^{-3}$	0.04	8000	200
		4	$5x10^{-3}$	0.1	800	200
		4	$5x10^{-4}$	0.1	8000	200
		10	$5x10^{-3}$	-	8000	200
		(square)*	$5x10^{-3}$	-	8000	200
		4 (square)*				

The stiffness study (Figure 7-1(A-D)) shows that the macroscopic behaviour of a DCB (without bridging) is not affected by the value of k_c. Regardless of the value of k_c, the *P-u* plot shows the same behaviour; hence the measured toughness $\hat{G}$ does not vary as shown in the R-curves.

In the strength study (Figure 7-1(E-H)), the maximum traction influences the peak value in the *P-u* plot and the plateau in the R-curve, however once

normalised using the total area under the TSL (i.e., the total input fracture energy G_{total}), the maximum traction has little effect on the R-curve.

Finally, by varying the shape of the TSL (Figure 7-1(I-L), similar trends were observed; once normalised, the R-curve was the same. In contrast, the TSL with the very large δ_{int} was noticeably different with a gradually increasing toughness. However, this TSL is not representative of material with only intrinsic toughening as δ_{int} is unphysically large. Such behaviour is more appropriately examined with a TSL that incorporates bridging as explored in this study.

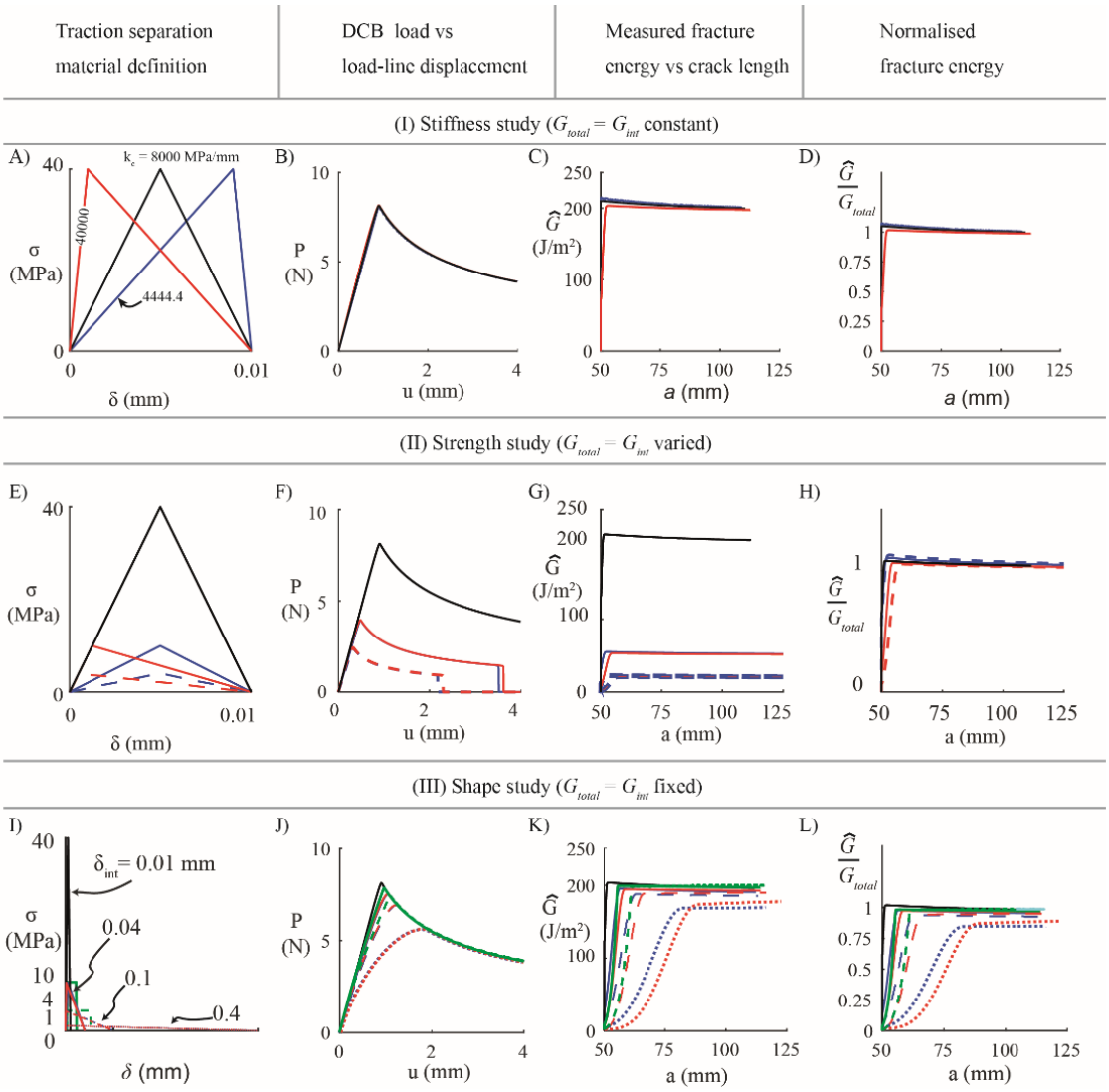

Figure 7-1 Summarised input parameters and results from the intrinsic study, i.e., no fibre bridging present.

7.2 Appendix 2 – development of a Graphical User Interface (GUI)

A graphical user interface (GUI) was developed for use by industry sponsors, Hexcel. This GUI is based on the findings presented in Chapter 3, the investigation into traction separation law parameters. The purpose of the GUI is to allow the operator to load experimental data, enter the test parameters and output the resultant traction separation law using the findings presented in Chapter 3. The GUI is also capable of creating a finite element analysis of an ASTM standard DCB test [2] specimen using the calculated traction separation law and test properties.

The GUI is split into two interfaces; the first interface is designed to read experimental data, adjust test properties, and calculate the resulting traction separation law. The second interface allows the user to run and postprocess finite element simulations. Figure 7-2 and Figure 7-3 show the first and second interface of the GUI respectively.

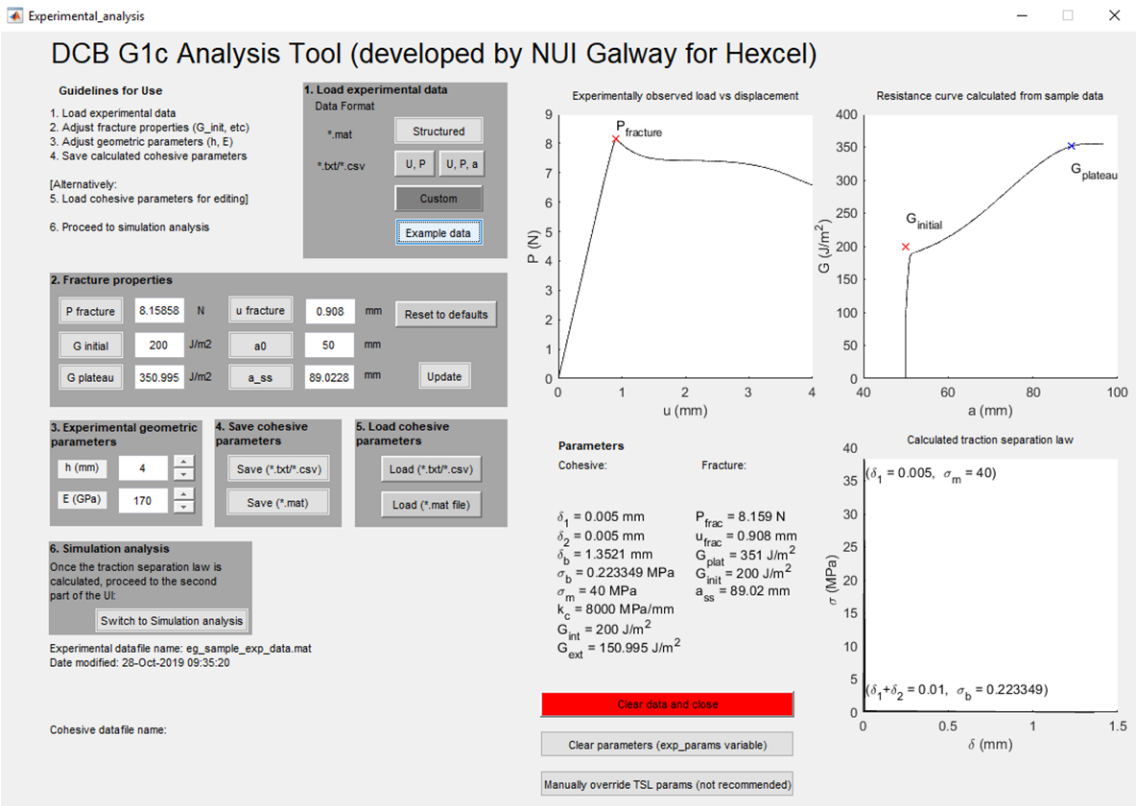

Figure 7-2 The first interface of the GUI which reads experimental data.

Experimental data can be loaded in different formats, namely as Matlab data structure, delimited text files or as a custom data set. The custom data set functionality is intended to read company text files as they may have unique headers or formatting. The data should contain applied load, load-line displacement and crack length. However, if crack length is not provided, the beam compliance is used to approximate the crack length by the equation below:

$$a = \sqrt[3]{\frac{3}{2}EIC} \qquad 7.1$$

The GUI also allows the user to edit fracture properties if they have been estimated incorrectly by the underlying code. Test parameters, such as modulus, are entered in edit boxes. Most properties can be manually overwritten, but it is not recommended as some R-curve relations outlined in Chapter 3 may be invalidated, depending on the property overwritten.

Resulting traction separation laws are plotted for inspection. These parameters can be output to text file or Matlab data structure. It is also possible to load an existing TSL and continue directly to the second interface.

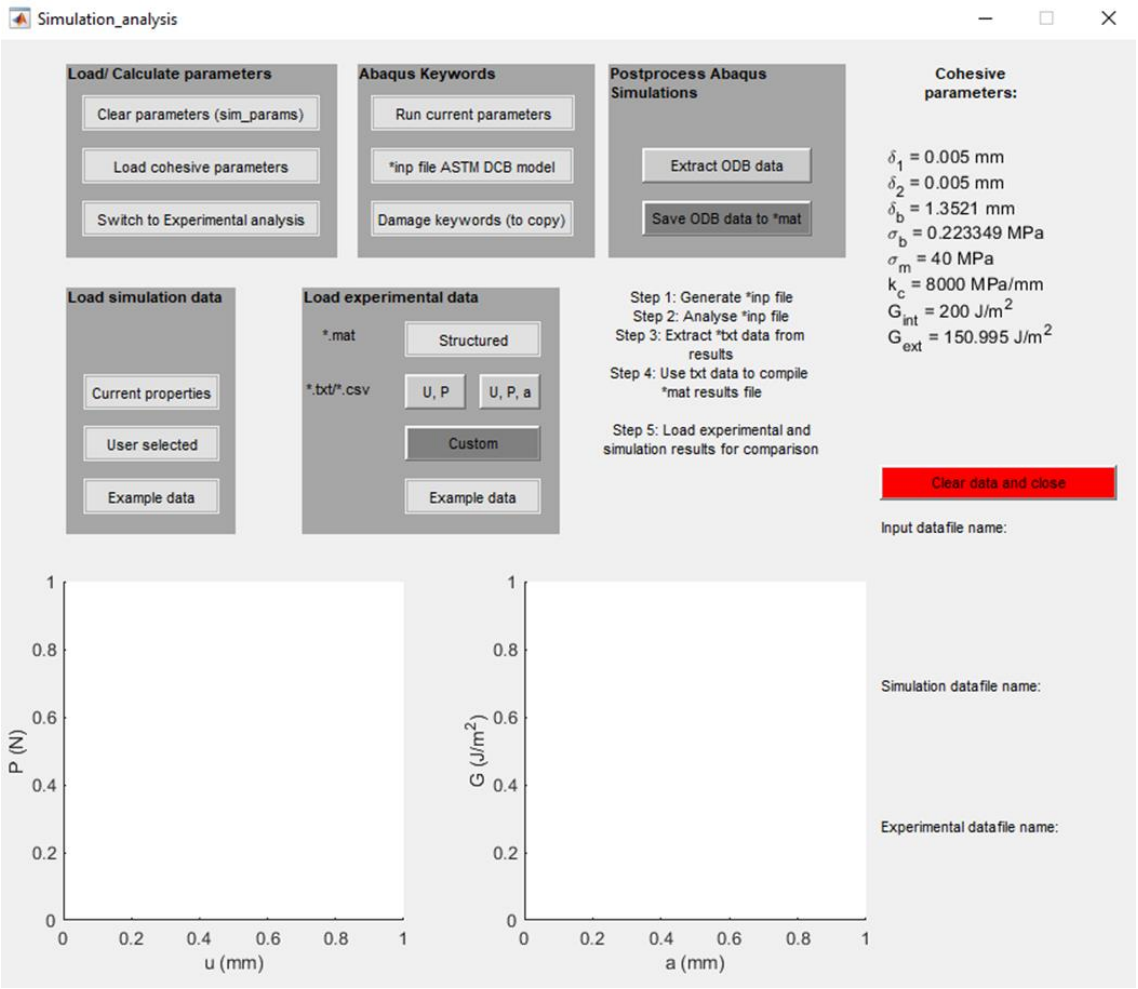

Figure 7-3 The second interface of the GUI which calculates simulation parameters and generates analysis files.

The second interface reads the experimental data and traction separation law properties calculated or loaded in the first interface. Abaqus input files for an ASTM DCB test can be produced based on the current parameters by executing a Python script. Alternatively, only damage related keywords can be written to an input file, intended to be copied into an existing analysis. The analysis is always completed in SI units (mm, N, MPa, s) but the parameters entered can be in any unit system, a conversion is completed in the code.

It is possible to run Abaqus analyses through this interface. It is also possible to run a Python postprocessing script and a Matlab data sorting script. Once data is compiled in a structured format; plotting tools allow simple comparison of computational and experimental results.

7.3 Appendix 3 - Compliance calibration method derivation

When modelling double cantilever beams (DCBs), traction separation law theory (previously discussed in Chapter 2) is relevant as the interface is modelled using cohesive elements. The behaviour of the interface elements is defined by a traction separation law. These models typically measure the applied load, P, load-line displacement, u, and crack length, a. The measured fracture energy, $\hat{G}$, in finite element models within this thesis is approximated using the compliance calibration (CC) method, in accordance the ASTM standard test method [2]. The derivation of this approximation is included for reference. The beam compliance, C, which is the ratio of load-line displacement to applied load is also needed in this approximation.

The CC equation in the ASTM standards is:

$$\hat{G} = \frac{nPu}{2ab} \tag{7.2}$$

Where b is the specimen width.

The strain energy release rate in 3D is given by the partial derivative of the internal energy Π:

$$G_I = -\frac{1}{b}\frac{\partial \Pi}{\partial a} \tag{7.3}$$

The strain energy is given by:

$$U = \frac{1}{2}Pu \tag{7.4}$$

The strain energy U is equal to the work done which is the force by displacement. In this case the load is linearly increasing so the load vs displacement plot is triangular. Meaning the work $W = \frac{1}{2}Pu$.

Rearranging and substituting compliance $C = \frac{u}{P}$ for u gives:

$$U = \frac{1}{2}CP^2 \tag{7.5}$$

The strain energy for a linear response:

$$\Pi = -U \tag{7.6}$$

$$G_I = -\frac{1}{b}\frac{\partial \Pi}{\partial a} = \frac{1}{b}\frac{\partial U}{\partial a} = \frac{P^2}{2b}\frac{\partial C}{\partial a} \tag{7.7}$$

As P does not depend on a.

The end deflection of a cantilever beam can be expressed as:

$$u_{beam} = \frac{PL^3}{3EI} \tag{7.8}$$

In the case of a DCB specimen, $u = 2u_{beam}$ and $L = a$

$$C = \frac{u}{P} = \left(\frac{1}{P}\right)\frac{2Pa^3}{3EI} \tag{7.9}$$

$$C = \frac{2}{3}\frac{a^3}{EI} \tag{7.10}$$

$$\frac{\partial C}{\partial a} = \frac{2a^2}{EI} \tag{7.11}$$

$$G_I = \frac{P^2}{2b}\frac{2a^2}{EI} = \frac{P^2a^2}{bEI} \tag{7.12}$$

$$G_I = \frac{P^2a^2}{bEI} = \frac{P^2a^2}{bEI} * \frac{2}{3} * \frac{3}{2} * \frac{a}{a} = \frac{3P^2C}{2ab} \tag{7.13}$$

Which leads to the following fracture energy equation:

$$\hat{G} = \frac{3Pu}{2ba} \tag{7.14}$$

The Berry method approximates the compliance with a power law:

$$\hat{G} = \frac{3Pu}{2ba} \tag{7.15}$$

$$C = ka^n$$

Where n and k are determined by experiments. n is the slope of $\log(C)$ vs $\log(a)$.

$$\frac{\partial C}{\partial a} = nka^{n-1} \tag{7.16}$$

$$G_I = \frac{P^2}{2b}\, nka^{n-1} * \frac{a}{a} \tag{7.17}$$

$$G_I = \frac{P^2}{2b}\frac{nC}{a} = \frac{P^2}{2b}\frac{nu}{aP} \tag{7.18}$$

This leads to the compliance calibration equation.

$$\hat{G} = \frac{nPu}{2ba} \tag{7.19}$$

$$\widehat{G(a)} = \frac{nP(a)\delta(a)}{2ba} \tag{7.20}$$

7.4 References

[1] Borotto M. Bridging effects on Mixed Mode delamination : experiments and numerical simulation. École Polytechnique Fédérale de Lausanne, 2016. https://doi.org/10.5075/epfl-thesis-7056.

[2] ASTM. Standard Test Method for Mode I Interlaminar Fracture Toughness of Unidirectional Fiber-Reinforced Polymer Matrix Composites 1 2013. https://doi.org/10.1520/D5528-13.